

POLITECNICO DI TORINO

MASTER OF SCIENCE THESIS

CFD analysis of combustion in
CNG/HCNG engines



Author: Pasquale Marco VISCIGLIO

Supervisors:

Daniela Anna MISUL

Mirko BARATTA

Rainer ROTHBAUER

25/07/2019

*Ai miei genitori e ai miei fratelli
che hanno sempre creduto in me*

Contents

Acknowledgements	i
Abstract	ii
1 CFD modelling	1
1.1 Introduction	1
1.2 What is CFD?	1
1.3 Basic concepts of Fluid Flow	2
1.4 Governing equations of Fluid Flow	3
1.4.1 Continuity equation	3
1.4.2 Momentum equation	5
1.4.3 Energy equation	7
1.4.4 Equation of State	8
1.5 Numerical solution methods	9
1.6 Grid control in CONVERGE [©] CFD Software	10
2 Fundamentals of HCNG properties	12
2.1 Why HCNG?	12
2.2 Relevant properties of HCNG for the engine	12
2.3 Advantages and challenges	13
3 CNG/HCNG Engine: Experimental data	15
3.1 Introduction	15
3.2 Engine main characteristics	15
3.2.1 Engine fuel	16
3.2.2 Intake system	17
3.2.3 Fuel supply system	18
3.2.4 Sensors	19
3.3 Experimental parameters for model validation	24
3.4 Data conditioning	27
3.5 Operating point considered	27
3.5.1 O.P. 2000 [rpm] x 3.6 [bar] x lambda=1: HCNG-15	28
3.5.2 O.P. 2000 [rpm] x 3.6 [bar] x lambda=1: HCNG-25	29
4 CNG/HCNG Engine: Case Setup	31
4.1 Geometry and regions	31
4.2 Regions Initialization and Boundary conditions	34
4.2.1 Regions Initialization	34
4.2.2 Boundary conditions	35
4.3 Fuel composition	37
4.4 Turbulence modeling	37
4.4.1 Introduction	37
4.4.2 The RANS equations and the k- ϵ model	38
4.5 Source/sink modeling	40
4.6 Mesh settings	41

5	Chemistry and Emissions modeling	44
5.1	Introduction	44
5.2	Combustion Models in CONVERGE	46
5.2.1	Models	46
5.2.2	SAGE Detailed Chemical Kinetics Solver	46
5.3	Mechanisms used	48
5.3.1	GRI Mech 3.0	48
5.3.2	USC mech II	48
5.3.3	USCD NO _x v2	49
5.4	Emissions Modeling	51
6	Results	53
6.1	Introduction	53
6.2	O.P. 2000[rpm] x 3.6[bar] x lambda=1; HCNG 15	53
6.2.1	Base simulation: GRI Mech 3.0	53
6.2.2	USC mech II	57
6.2.3	USC + USCD mechanisms merged	61
6.2.4	Schmidt Number sensitivity	66
6.2.5	Reduction of the temperature of the wall	76
6.2.6	LHV correction	84
6.2.7	Crevice volume	88
6.3	O.P. 2000[rpm] x 3.6[bar] x lambda=1; HCNG 25	102
6.3.1	Base simulation: <i>GRI Mech 3.0</i>	102
6.3.2	USC mech II	106
6.3.3	USC + USCD mechanisms merged	112
6.3.4	Boundary conditions manipulation	115
6.3.5	Crevice Volume	121
7	Conclusions and Future Developments	130
	List of Figures	136
	List of Tables	138
	References	139

Acknowledgements

I would like to express my gratitude to all the people who supported me in every situation, accompanying me towards the accomplishment of my targets and my dreams.

First of all, I would like to thank my supervisor at Convergent Science GmbH, Dr. Rainer Rothbauer for the great occasion to join the team, for his support and for the access to all the equipment and facilities, which allowed me to develop my thesis project. I would also express my deep gratitude to my supervisors at Politecnico di Torino: Prof. Daniela Misul and Prof. Mirko Baratta. I will always be grateful to you not only for your kindness, patience and constant support but also for giving me the opportunity to work on this project, which allowed me to grow up from the professional and personal point of view.

I would also like to thank the whole team of Convergent Science GmbH: Ivona, Riccardo, Matteo, Pietro, Bugra, Suresh, Jyothish, Vera, Veera, Edith and in particular Lorenzo and Luca who really helped me with the thesis development and in general throughout my stay in Austria.

I would like to say a huge “thank you” to all the people that I have met in these years.

To Flavia, Ginevra, Giulio and Sveva for having always sustained me during the studies in Turin and in general in every hard situation.

To the amazing group of *tanos*: Alessio, Daniele, Giacomo, Giulia, Gloria, Marco, Marta and of course Aldo which have made the months in South America one of the best experience of my life.

To my best friend Pierluigi and to my “*sisters*” Rossella and Tania which are always on my side, despite the distance.

To all my friends who have an important weight on my life.

To my family: Gino, Margherita, Lorenzo and Antonio, who, with their support both moral and economic, taught me to overcome any challenge met in my life.

Abstract

The aim of this thesis project is to study the combustion of ICE engines fuelled with natural gas, NG, and mixtures of natural gas with a percentage of hydrogen, HCNG. The work is carried out to support the European research project called *GasOn* whose target is to realize a sustainable and more efficient mobility in Europe, improving the energy efficiency of the powertrain. The use of low carbon alternative fuels like HCNG, will play in fact a fundamental role on the de-carbonisation process and it is beneficial for the reduction of pollutant emissions.

A powerful tool able to study the combustion process in engines is the *Computational Fluid Dynamics*, CFD, analysis: this approach is based on the theory of the fluid mechanics and it allows to solve problems related to fluid flows. Nowadays, there are several software in the market able to run CFD simulations; the commercial code used in this work is **CONVERGE**, provided by **Convergent Science GmbH** (Austria) company where this thesis has been carried out. Furthermore, thanks to the collaboration with **Politecnico di Torino** and in particular with the DENERG laboratory, the real performances of the *FIAT FIRE 1.4 16V Turbo* engine have been compared with the numerical results obtained from the simulations.

The study is focused on two different fuels, each containing distinct percentages of hydrogen: 15% and 25% of H₂. The validation of the model is based on the main characteristic parameters of the combustion, such as pressure, dissipation of energy inside the cylinder and finally pollutant emissions. The combustion process has been simulated through the *SAGE detailed chemistry* model; furthermore, different reaction mechanisms have been used in order to find the numerical model which simulates the real behavior of the engine as well as possible.

The thesis can be split into three main parts. The first part introduces the numerical modelling, with a brief description of the fluid governing equations useful for the CFD analysis, the discretization approaches and the base concepts of the CONVERGE software. The second part is focused on the main characteristics of the engine and lists the experimental data obtained in laboratory. In addition, it describes the case setup of the engine itself on the CONVERGE interface, showing for example the CAD geometry, the boundary conditions and the combustion and turbulence models used. Finally, the third part compares the numerical results with the experimental data, showing all the changes made to the case setup in order to reach the best possible results.

1 CFD modelling

1.1 Introduction

In engineering, modeling a process means developing and using the appropriate combination and equations in order to analyze critical features of a particular case-study. The modeling of engine process continues to evolve in parallel with the technology and the capability of the computers, understanding even more in detail the physics and chemistry of the phenomena of interest. The major contributions to engine engineering are:

- developing a complete and detailed of the process, involving numerical models.
- identifying key controlling variables and then that provide guidelines, thus less experimental development costs;
- predicting engine behavior and, if the model is sufficiently accurate, optimizing design and control
- providing a rational basis for design innovation.

A very useful tool which is increasingly used for this purpose is the Computational Fluid Dynamics, CFD, model.

[1]

1.2 What is CFD?

Computational Fluid dynamics (CFD) is the analysis of systems involving fluid flow, heat transfer and associated phenomena such as chemical reactions by means of computer-based simulations. The technique is very powerful and is used in different areas, industrial and non-industrial (e.g. aerodynamics of aircraft and vehicles, hydrodynamics of ships, turbomachinery, chemical process engineering). As availability of high-performance computing hardware have been increased and even more user-friendly interfaces have been introduced, the CFD techniques have become more popular, leading to a complete description of fluid flow in less time cost. Nowadays, CFD is becoming a vital component for the industrial product design.

All the commercial CFD codes contain three main elements:

- **Pre-processor:** consists of the input of flow problem to a CFD program by means of an operator-friendly interface. Hence, this input is transformed into a form suitable for use by the solver. The user activities at the pre-processing stage are definition of the geometry and of the computational domain, grid control, definition of fluid properties, selection of the chemical phenomena and specification of the boundary conditions;
- **Solver:** it solves the equations of fluid motion as a steady-state or transient through iterative methods, by means of numerical techniques like *Finite elements method*, *Finite differences method*, or *Finite volume method*;

- **Post-processor:** CFD packages are equipped with versatile data visualization tools e.g. domain geometry and grid display, 2D and 3D surface plots, particle tracking and view manipulation. It allows the user to analyze and visualize the results of the simulation.

In the next section, the fundamental basis of the CFD problems will be described: the governing equations of fluid flow, the numerical solution methods and turbulence. Finally, the CONVERGE[®] CFD Software adopted in this thesis project will be introduced.

1.3 Basic concepts of Fluid Flow

The substances whose molecular structure offers no resistance to external shear forces are called fluids: even the smallest force causes *deformation* of a fluid particle. It is possible to do a significant distinction between liquids and gases, but both types of fluids obey the same laws of motion.

The fluid flow is generated by external forces; they can be *surface forces* (e.g. the shear force) and *body forces* (e.g. gravity) and can include pressure differences, gravity, shear, rotation, and surface tension.

To study the fluid motion the *macroscopic properties* of the fluids must be known; the most important properties are *density* and *viscosity*. These properties are strictly dependent on thermodynamic variables (e.g. temperature and pressure).

Another variable which can affect these properties is the speed: depending on the regime the fluid can be *creeping* (at low enough speeds), *laminar* and *turbulent* (as the speed increases and the inertia of the fluid becomes important). In addition, the *transition* process of laminar-turbulent is very important for the study of the fluid motion and it is defined by the Reynolds number, Re . This number represent the ratio between the inertia factor and the viscosity factor: as the inertia factor increases, the Reynolds number is high, then the flow is turbulent and the particles have a random motion. Hence, the effects of the viscosity, which affect the Reynolds number, are very important but only near walls. For this reason, the flow in the largest part of the domain can be considered as *inviscid*. There are several viscosity laws; in this thesis work the Newton's law of viscosity will be the only one considered.

It is also possible to describe the fluid through the Mach number, Ma , which is the ratio of the flow speed to the speed of the sound in the fluid: for small Mach numbers, $Ma < 0.3$, the flow may be considered *incompressible*; otherwise, it is *compressible*. Furthermore, the flow is called *subsonic* ($Ma < 1$) and *supersonic* ($Ma > 1$). Finally, when the fluid reaches high enough temperatures because of the compression its nature can change; this happens with $Ma > 5$ and the flows are called *hypersonic*. Obviously, the mathematical nature of the problem and therefore the solution method depend on these distinctions.

Many other phenomena which affect the fluid flow are: temperature differences (which lead to heat transfer and density differences), differences in concentration of solutes, phase changes, surface tension etc.

[2]

1.4 Governing equations of Fluid Flow

The computational fluid dynamics makes use of three fundamental governing equations of fluid dynamics: the *continuity equation*, the *momentum equation* and the *energy equation*. These equations are based on three fundamental physical concepts, which are:

- mass conservation;
- second Newton's law: $\mathbf{F} = m\mathbf{a}$;
- energy conservation.

In addition to the equations developed from the universal laws, it is really important to describe the relationships between fluid properties in order to close the system of equations: the equation of state, which relates variables like pressure, density and temperature is an example.

There are two main approaches to study the fluid flow:

- “**Lagrangian model**” or *Infinitesimal fluid element model*: focus on an **individual fluid parcel** which is moving through the domain (space) and time. From this method, partial differential equations are given directly by applying the physical principles on a control volume;
- “**Eulerian model**” or *Finite control volume model*: focus on the **fluid motion** on specific locations (finite control volume) through which the fluid flow as time passes. From this method, equations in integral form are obtained by applying the physical principles on a control volume. Thus, they can be manipulated to obtain partial differential equations.

1.4.1 Continuity equation

The *Lagrangian model* is considered first. The mass variation of the fluid particle δm in a volume δV is described as:

$$\delta m = \rho \delta V$$

According to the Lagrangian approach, the mass conservation principle states that as the element moves along with the flow the time-rate-of-change of the mass is equal to zero, thus:

$$\frac{D(\delta m)}{Dt} = 0$$

where $\frac{D(\delta m)}{Dt}$ is the variation of the mass of the given fluid through the space and the time; the so-called *substantial derivative*.

Combining these two equations:

$$\frac{D(\rho \delta V)}{Dt} = \delta V \frac{D\rho}{Dt} + \rho \frac{D(\delta V)}{Dt} \quad (1.1)$$

Finally, dividing by δV and applying the physical meaning of $\nabla \cdot \mathbf{v}$, which means the volume time rate of change of a moving fluid, the continuity equation is obtained according to the following eq. 1.2:

$$\frac{D\rho}{Dt} + \rho \nabla \cdot \mathbf{v} = 0 \quad (1.2)$$

Considering the *Eulerian model*, the mass conservation principle of the flow applied to the control volume is expressed by:

$$\frac{\partial \rho}{\partial t} + \nabla \cdot (\rho \mathbf{v}) = 0 \quad (1.3)$$

where \mathbf{v} is the velocity of the flow. According with eq. 1.3, the continuity equation in the Eulerian approach states that the rate of change of the mass inside the control volume is equal to the net rate of mass flowing through the surface that bounds the volume.

For Cartesian coordinate system, the equation 1.3 can be expressed as:

$$\frac{\partial \rho}{\partial t} + \frac{\partial(\rho v_x)}{\partial t} + \frac{\partial(\rho v_y)}{\partial t} + \frac{\partial(\rho v_z)}{\partial t} = 0 \quad (1.4)$$

where v_x, v_y, v_z are the x, y, z components of the velocity vector.

Finally, considering the vector elemental surface area $d\mathbf{S}$ and an elemental volume dV inside the control volume, the continuity equation can be expressed in integral form by integrating over the entire volume V the eq. 1.3:

$$\frac{\partial}{\partial t} \iiint_V \rho dV + \iint_S \rho \mathbf{v} d\mathbf{S} = 0 \quad (1.5)$$

For steady air flows with speed < 100 m/s we can assume that the fluid is *incompressible*, then:

$$\frac{D\rho}{Dt} = 0$$

so the equation for the *Lagrangian approach* (eq. 1.2) becomes:

$$\nabla \cdot \mathbf{v} = 0 \quad (1.6)$$

and for the *Eulerian approach* (eq. 1.4):

$$\frac{\partial(\rho v_x)}{\partial t} + \frac{\partial(\rho v_y)}{\partial t} + \frac{\partial(\rho v_z)}{\partial t} = 0 \quad (1.7)$$

[3]

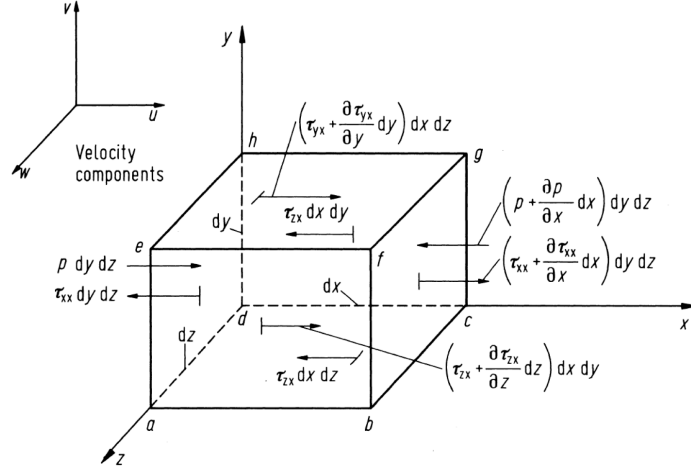


Figure 1.1: Surface forces in the x -direction exerted on the fluid element

1.4.2 Momentum equation

A mathematical expression of the Newton's second law applied to fluids is the *momentum equation*. The vector relation between the net force and mass multiplied by the acceleration of the fluid element can be split into three scalar expressions: along x , y and z -axes.

There are two main forces acting on the particle:

- Surface forces: applied directly on the surface of the fluid (e.g. pressure forces)
- Body forces: applied on the control volume by distance (e.g. magnetic, gravitational, electric forces)

For the derivation of the momentum equation, the *Lagrangian approach* will be considered in this demonstration. Let us consider the x -axis; then the mathematical expression of the Newton's second law is:

$$F_x = ma_x \quad (1.8)$$

where F_x is the sum of the *surface forces*, $F_{surface,x}$ and *body forces*, $F_{body,x}$:

$$F_x = F_{surface,x} + F_{body,x} \quad (1.9)$$

The *surface forces* exerted on the fluid element are shown in Fig.1.1 : The net surface force on the moving fluid element in the x -direction is:

$$\begin{aligned}
 F_{surface,x} = & \left[p - \left(p + \frac{\partial p}{\partial x} dx \right) \right] dydz + \\
 & + \left[\left(\tau_{xx} + \frac{\partial \tau_{xx}}{\partial x} dx \right) - \tau_{xx} \right] dydz + \left[\left(\tau_{xy} + \frac{\partial \tau_{xy}}{\partial y} dy \right) - \tau_{xy} \right] dx dz + \\
 & + \left[\left(\tau_{xz} + \frac{\partial \tau_{xz}}{\partial z} dz \right) - \tau_{xz} \right] dx dy
 \end{aligned} \quad (1.10)$$

where τ_{xx} is the normal stress in the x -direction and τ_{xy} and τ_{xz} are the shear stresses in the other directions. Therefore, the $F_{surface,x}$ of the equation 1.10 is:

$$F_{surface,x} = \left(-\frac{\partial p}{\partial x} + \frac{\partial \tau_{xx}}{\partial x} + \frac{\partial \tau_{xy}}{\partial y} + \frac{\partial \tau_{xz}}{\partial z} \right) dx dy dz \quad (1.11)$$

Focusing now on the *body forces* and denoting the body force per unit mass acting on the fluid element by \mathbf{f} , it is possible to express $F_{body,x}$ as:

$$F_{body,x} = \rho f_x dx dy dz \quad (1.12)$$

where f_x is the x -component of \mathbf{f} and $dx dy dz$ is the volume of the fluid element. By combining eq. 1.11, 1.12 and 1.9, F_x becomes:

$$F_x = \left(-\frac{\partial p}{\partial x} + \frac{\partial \tau_{xx}}{\partial x} + \frac{\partial \tau_{xy}}{\partial y} + \frac{\partial \tau_{xz}}{\partial z} \right) dx dy dz + \rho f_x dx dy dz \quad (1.13)$$

Furthermore, the mass of the fluid element is fixed and is $m = \rho \cdot dx dy dz$. Adopting the substantial derivative, the second term of the equation 1.8 can be written as:

$$ma_x = \rho \cdot dx dy dz \cdot \frac{Dv_x}{Dt} \quad (1.14)$$

By combining equations 1.13, 1.14 and 1.8 the x -component of the momentum equation for a viscous flow is expressed as:

$$\rho \frac{Dv_x}{Dt} = -\frac{\partial p}{\partial x} + \frac{\partial \tau_{xx}}{\partial x} + \frac{\partial \tau_{xy}}{\partial y} + \frac{\partial \tau_{xz}}{\partial z} + \rho f_x \quad (1.15)$$

Similarly, the y and z -components will be respectively:

$$\rho \frac{Dv_y}{Dt} = -\frac{\partial p}{\partial y} + \frac{\partial \tau_{yy}}{\partial y} + \frac{\partial \tau_{yx}}{\partial x} + \frac{\partial \tau_{yz}}{\partial z} + \rho f_y \quad (1.16)$$

$$\rho \frac{Dv_z}{Dt} = -\frac{\partial p}{\partial z} + \frac{\partial \tau_{zz}}{\partial z} + \frac{\partial \tau_{zx}}{\partial x} + \frac{\partial \tau_{zy}}{\partial y} + \rho f_z \quad (1.17)$$

which can be written in compact form:

$$\rho \frac{D\mathbf{v}}{Dt} = \rho \mathbf{f} + \nabla \cdot \mathbf{P}_{ij} \quad (1.18)$$

where \mathbf{P}_{ij} is the stress tensor which represents the surface forces per unit volume (its components are normal and shearing stresses τ_{ii} and τ_{ij}).

1.4.3 Energy equation

Since heat energy cannot be created or destroyed, it can only be transferred from one location to another, so a conservation of energy occurs. This concept, is described by the energy equation, which is the mathematical expression of the first law of thermodynamics.

In particular, for a fluid passing through an infinitesimal and fixed control volume, the energy equation is:

$$\frac{\partial E_t}{\partial t} + \nabla \cdot E_t \mathbf{v} = \frac{\partial Q}{\partial t} - \nabla \cdot \mathbf{q} + \rho \mathbf{f} + \nabla \cdot (\mathbf{P}_{ij} \cdot \mathbf{v}) \quad (1.19)$$

where E_t is the total energy per unit volume given by:

$$E_t = \rho \left(e + \frac{v^2}{2} + \text{potential energy} + \dots \right) \quad (1.20)$$

and e is the internal energy per unit mass.

According to the Fourier's law for heat transfer, the term $\nabla \cdot \mathbf{q}$ can be written by means of the coefficient of thermal conductivity, k , and the temperature T :

$$\mathbf{q} = -k \nabla T \quad (1.21)$$

Furthermore, considering a Cartesian coordinate system, the eq. 1.19 becomes:

$$\begin{aligned} \frac{\partial E_t}{\partial t} - \frac{\partial Q}{\partial t} - \rho(f_x v_x + f_y v_y + f_z v_z) + \frac{\partial}{\partial x}(E_t v_x + p v_x - v_x \tau_{xx} - v_y \tau_{xy} - v_z \tau_{xz} + q_x) + \\ + \frac{\partial}{\partial y}(E_t v_y + p v_y - v_x \tau_{xy} - v_y \tau_{yy} - v_z \tau_{yz} + q_y) + \\ + \frac{\partial}{\partial z}(E_t v_z + p v_z - v_x \tau_{xz} - v_y \tau_{yz} - v_z \tau_{zz} + q_z) = 0 \end{aligned} \quad (1.22)$$

considering the continuity equation and assuming that only kinetic and internal energy are significant in eq.1.20, the left hand side of the eq.1.19 can be written as:

$$\frac{\partial E_t}{\partial t} + \nabla \cdot E_t \mathbf{v} = \rho \frac{D}{Dt} \left(\frac{E_t}{\rho} \right) = \rho \frac{De}{Dt} + \rho \frac{D}{Dt} \frac{v^2}{2} \quad (1.23)$$

Then, by making the scalar product and considering eq.1.18:

$$\rho \frac{D\mathbf{v}}{Dt} \cdot \mathbf{v} = \rho \mathbf{f} \cdot \mathbf{v} + \nabla p \cdot \mathbf{v} + (\tau_{ij}) \cdot \mathbf{v} \quad (1.24)$$

Combining eqs.1.23 and 1.24 and substituting into 1.19, it holds:

$$\rho \frac{De}{Dt} + p(\nabla \cdot \mathbf{v}) = \frac{\partial Q}{\partial t} - \nabla \cdot \mathbf{q} + \nabla \cdot (\tau_{ij} \cdot \mathbf{v}) - (\nabla \cdot \tau_{ij}) \cdot \mathbf{v} \quad (1.25)$$

the last two terms of the right hand side can be combined into a single term:

$$\Phi = \nabla \cdot (\tau_{ij} \cdot \mathbf{v}) - (\nabla \cdot \tau_{ij}) \cdot \mathbf{v}$$

Φ represents the rate at which the mechanical energy is expended in the process of deformation of the fluid due to viscosity. The eq.1.25 becomes:

$$\rho \frac{De}{Dt} + p(\nabla \cdot \mathbf{v}) = \frac{\partial Q}{\partial t} - \nabla \cdot \mathbf{q} + \Phi \quad (1.26)$$

Finally, considering the enthalpy definition, e.g. $h = e + \frac{p}{\rho}$, the last equation can be written as:

$$\rho \frac{Dh}{Dt} = \frac{Dp}{Dt} + \frac{\partial Q}{\partial t} - \nabla \cdot \mathbf{q} + \Phi \quad (1.27)$$

1.4.4 Equation of State

The motion of fluid in three dimensions is described by a system of partial differential equations shown above (the Energy Equation, the Mass Equation and Mass Conservation Equation). Unfortunately, this system is very difficult to solve analytically and there is no general closed-form solution; for that reason a further equation is needed: the Equation of State.

The Equation of State describes the fluid under a given sets of physical conditions. Basically, it establishes relations between the thermodynamic variables (p, ρ, T, e, h) and closes the system of fluid dynamic equations.

Considering the intermolecular forces as negligible, it is possible to assume the fluid as a *perfect gas*, subjected to the perfect gas equation of state:

$$p = \rho RT \quad (1.28)$$

where R is the gas constant.

However, under particular conditions of high pressure and temperature the intermolecular forces are not negligible. In these cases, the perfect gas equation of state can not be used and alternative equations must be considered, e.g. the *Waals equation of state*.

On the other hand, for gas with relatively low temperature it is possible to assume constant specific heats: c_v, c_p and their ratio γ .

If the fluid considered is a liquid, it is possible to assume that the variation of the density with pressure and temperature is almost zero and in these cases it is called *incompressible fluid*. Obviously, without density variation the Energy Equation, Momentum Equation and the Mass Equation are not linked so it is impossible to find a correlation between the thermodynamic variables. For that reason, the study of the flow field for liquids is carried out just considering the Mass Conservation Equation and the Momentum Equation while the Energy Equation is used to study the heat transfer process.

1.5 Numerical solution methods

As introduced above, the phenomena related with flows are described by partial differential equations that cannot be solved analytically. A strategy which allows to obtain a solution from these equations is the discretization method. Through these method in fact it is possible to approximate the differential equations to a system of algebraic equations. The approximation is applied to small domains in space and/or in time; thus, the accuracy of the numerical solutions is dependent on the quality of discretization used. For that reason, the results will not represent exactly the reality but they can be close enough to be considered acceptable.

The numerical solution method is composed by:

- *Mathematical Model*: the set of partial differential or integro-differential equations and boundary conditions. As described before, an approximation is needed to solve these equations.
- *Discretization Method*: it approximates the partial differential equations to an algebraic equations system. The main important methods are the *Finite Element Method*, the *Finite Difference Method* and the *Finite Volume Method*.
- *Coordinates*: a coordinates system is essential to describe the conservation equations. Some examples are the Cartesian, cylindrical, spherical, curvilinear orthogonal or non-orthogonal coordinate systems.
- *Numerical grid*: called also *mesh*, it defines the discrete locations where the variables are calculated. It is a representation of the geometric domain, divided into a finite number of sub-domains (elements, control volumes, etc.). There are different types of grid: the *structured grid*, with a regular connectivity, the *block structured grid* (with more level of subdivision) and *unstructured grid* (the most flexible which allows to define an arbitrary solution domain boundary). However, although a high number of grid cells in the domain provides more accurate results, it increases the simulation run time; thus, a compromise should be found.
- *Solution Method*: this method solves the non-linear equations by iterative techniques.
- *Converge Criteria*: it states when to stop the iterative process.

[2] [4] [5]

1.6 Grid control in CONVERGE[®] CFD Software

The different tools for the grid generation control used by CONVERGE are:

- Grid Scaling
- Fixed embedding
- Adaptive mesh refinement

Grid scaling

In order to reduce the runtime of the simulation, the Grid scaling might be useful: it allows to change the base grid size at specified times. To do that, CONVERGE uses the *grid_scale* parameter and determines the base grid size via *dx_base* and *dz_base* according to the following relation:

$$scaled\ grid = \frac{dx_base}{2^{grid_scale}} \quad (1.29)$$

where *grid_scale* is the scaling parameter and *scaled grid* is the new value of base grid size. While negative and positive values make the base grid coarsen or refined respectively, a *grid_scale* of 0 leaves the base cells unchanged.

Fixed embedding

This tool is useful to refine mesh just in specific locations of the domain (e.g. spray, valves). The user has to specify an embedding scale in order to indicate to CONVERGE how to refine the grid in the chosen location. The *embed_scale* scales the base sizes according to:

$$dx_embed = \frac{dx_base}{2^{embed_scale}} \quad (1.30)$$

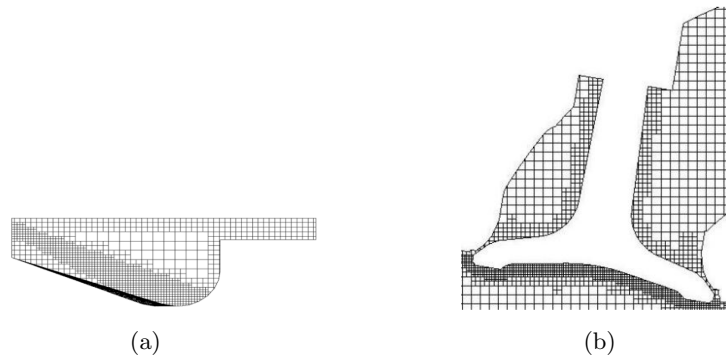


Figure 1.2: (a) nozzle embedding; (b) fixed embedding around a valve

Adaptive Mesh Refinement (AMR)

“The Adaptive Mesh Refinement (AMR) automatically refine the grid basing on fluctuating and moving conditions such as temperature and/or velocity. This option permits to have a very high refined grid to accurately simulate complex phenomena such as high-velocity flow and flame propagation without slowing the simulation using a globally refined mesh. Ideally, a good AMR algorithm will add higher grid resolution where the flow field is most under-resolved or where the sub-grid field is the largest. Generally speaking, the AMR algorithm will add a grid refinement when the gradient of velocity or temperature between two cells is higher that the value specified, in this way it is possible to capture some complex phenomena behaviour that would be impossible to catch without a global grid refinement”. [6]

With CONVERGE it is possible to use the AMR for many fields (e.g. velocity, number of parcels per cell, temperature and so on). In addition, the user can specify the time when the AMR will start and when it will end for each field. However, sometimes the sub-grid quantities near the solid walls trigger the AMR. CONVERGE avoid the refinement near the walls with the y^+ restriction; in this way CONVERGE automatically will remove refinement from AMR to maintain the desired target value. Further informations about the AMR are described in [6]

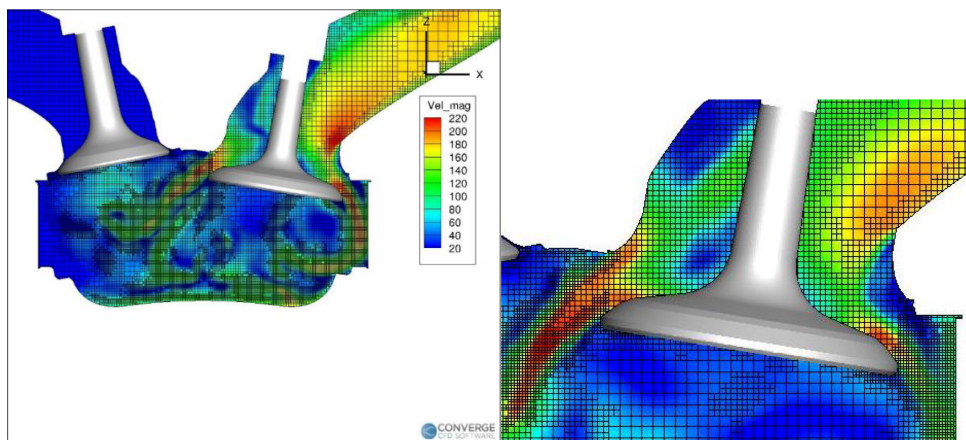


Figure 1.3: AMR through the valves

2 Fundamentals of HCNG properties

2.1 Why HCNG?

Nowadays, 97% of energy is used by transportation vehicles in land, sea and sky. Various products of unrefined petroleum mainly gasoline, diesel and aviation fuel are used by these vehicles. However, it is not permanent and unlimited and one day it will be exhausted.

The combustion of the unrefined petroleum presents another important problem: it produces unhealthy air pollutant's exhaust. After combustion, several substances are released including three main pollutants such as CO, NO_x and HC. For this reason, the consequences of the emissions of the internal-combustion engines can be figured out by using alternative fuels: biodiesel, bio alcohol, biomass, biogas, natural gas (fossil fuels), hydrogen (H₂) are many examples.

Hydrogen and natural gas are known as source of clean energy and are abundant and easy to collect. Hence, conventional natural gas as CH₄ is compressed at very high pressure to produce CNG (Compressed Natural Gas). Furthermore, in the recent years a mixture of hydrogen and CNG has been developed: the HCNG (Hydrogen Compressed Natural Gas) fuel.

The addition of H₂ in CNG provides a lot of advantages, such as rapid flame speed, large flammability limits, renewability of H₂, high-volume calorific value, less emission of CH₄, etc.

[7]

2.2 Relevant properties of HCNG for the engine

Generally, the HCNG fuels contain a small amount of hydrogen (5-30% by volume). Obviously, the properties of the HCNG fuel depend on the amount of the hydrogen; Figure 2.1 [8] and Figure 2.2 [9] show an overall comparison of properties of an example fuel (with 90.2% of CH₄) with 5%, 10%, 20% and 30% of H₂ (HCNG 5, 10, 20, 30 respectively).

The HCNG is well suited for engine applications thanks to different features:

- Addition of hydrogen increases the H/C ratio of the fuel which leads to a reduction of CO₂, thereby less greenhouse gas emissions.
- Hydrogen has the flame speed about eight times higher than natural gas. For this reason, H₂ can extend the amount of charge dilution reaching values of excess air ratio much higher than the stoichiometric condition, maintaining a very stable combustion.
- HCNG has an extended lean operating limit which reduces HC and CO emissions.

Properties	H ₂	HCNG 5	CH ₄	Gasoline
Limits of Flammability in air, vol %	4-75	5-35	5-15	1.0 -7.6
Stoichiometric composition in air, vol %	29.53	22.8	9.48	1.76
Minimum energy for ignition in air, mJ	0.02	0.21	0.29	0.24
Auto ignition Temp, K	858	825	813	501-744
Flame Temperature in air, K	2318	2210	2148	2470
Burning Velocity in NTP ^a air, cms ⁻¹	325	110	45	37-43
Quenching gap in NTP air, cm	0.064	0.152	0.203	0.2
Normalized Flame Emissivity	1.0	1.5	1.7	1.7
Equivalence ratio flammability limit in NTP air	0.1-7.1	0.5-5.4	0.7-4	0.7-3.8
Methane Number	0	76	80	-
Composition of CNG: CH ₄ – 90.2%, C ₂ H ₆ – 8.5%, C ₃ H ₈ -0.6%, N ₂ -0.6%, Butane- 0.1%				
^a NTP denotes normal temperature(293.15K) and pressure(1atm)				

Figure 2.1: Comparison of properties of Hydrogen, CNG and HCNG5 with Gasoline

Properties	CNG	HCNG 10	HCNG 20	HCNG 30
H ₂ [% vol]	0	10	20	30
H ₂ [% mass]	0	1.21	2.69	4.52
H ₂ [% energy]	0	3.09	6.68	10.94
LHV[MJkg ⁻¹]	46.28	47.17	48.26	49.61
LHV[MJ Nm ⁻³]	37.16	34.50	31.85	29.20
LHV stoich. mixture [MJNm ⁻³]	3.376	3.368	3.359	3.349

Figure 2.2: Properties of CNG and HCNG blends with different hydrogen content

Concerning this thesis project, the main fuel compositions studied are HCNG composed by 15% and 25% of H₂.

[10]

2.3 Advantages and challenges

Thanks to its properties described above, the HCNG usage as fuel presents some advantages [10]:

- HCNG is usable with the existing CNG infrastructure; only small hydrogen storage and a column for the mixing with natural gas is required.

- HCNG is safer to handle than hydrogen because of the lower amount of energy from H₂ (%vol of H₂ in HCNG only up to 30%).
- It extends the lean misfire limit of CNG.
- Hydrogen addition to natural gas can speed up the combustion process, which means less engine's unburned hydrocarbons (high lean burn capacity).
- Higher brake thermal efficiency and decrease of fuel consumption.

However, there are still some aspects and challenges to consider for the complete diffusion of the HCNG usage in the automotive industry [7]:

- Increasing the hydrogen fractions into CNG above a specific level gives abnormal combustion and phenomena such as knocking, pre-ignition and backfire. Thus, higher levels of exhaust emissions are obtained which cannot fulfill the emission standards.
- There is a strong relationship between hydrogen addition, excess air ratio (λ) and spark timing; the challenge is to find the optimal combinations of these three parameters.
- NO_x emissions are extremely low for CNG compared with traditional fuels; however, adding hydrogen to natural gas could lead to a higher value of oxides of nitrogen which are not tolerable.
- The hydrogen production cost is higher than the production cost of natural gas; consequently, HCNG blends are more expensive compared to CNG. The production of H₂ from renewable-energy sources (e.g. solar energy) could be a good solution.

The main features of the engine and the different fuel compositions used for this thesis project will be described in the next chapter.

3 CNG/HCNG Engine: Experimental data

3.1 Introduction

The aim of this thesis project is to develop a CFD model for a SI-Engine which fits as much as possible with the real performance of the engine. In particular, the *Politecnico di Torino* has carried out measures of the *Fiat FIRE 1.4 16V Turbo CNG* engine at different operating points (changing *load* and *rpm*).

The focus of this project is the combustion process: as first approach, main parameters such as *pressure*, *heat release*, *integrated heat release* and *trapped mass* will be compared with the experimental data through the CFD models. Secondly, pollutant emissions such as CO, CO₂, NO_x and HC will be analyzed. The experimental data have been taken directly from the Energy Laboratory of the university, where the engine is installed. The measurements, subdivided per engine operating point, have been provided as a TDMS (Technical Data Management Streaming) file extension. However, this file extension is not readable directly by *Excel* so a conversion has been carried out with *Add-In Excel Tool*. Each file represents a specific engine working condition; for example the document called `2000_360_04.tdms` indicates the operating point at 2000 rpm and 3.6 bar : “2000 [rpm] x 3.6 [bar]”.

In this chapter we are going to describe the main characteristic of the engine, the experimental data as well as the parameters for the model validation.

3.2 Engine main characteristics

The engine described above, shown in Figure 3.1, has been made by *Centro Ricerche Fiat* in Orbassano with the aim of developing a new generation engine following the “downsizing” logic: reduced size and higher, or at least equal, power. Furthermore, it is optimized for the methane and CNG/HCNG combustion.

The engine technical data are reported in Table 1 .

[11]



Figure 3.1: Engine and test bench under construction

Table 1: Engine technical data

Cycle	Otto (4 strokes)
Fuel supply	Matatron METAFUEL 6AO.PNT injector
Valves	16V, two camshaft in head
Intake valve opening (IVO)	TDC -3°
Intake valve closing (IVC)	BDC $+37^\circ$
Exhaust valve opening (EVO)	BDC $+37^\circ$
Exhaust valve closing (EVC)	TDC -30
Cylinders	4 (inline)
Bore	72 mm
Stroke	84 mm
Displacement	1368 cm ³
Connecting rod length	129 mm
Compression ratio (CR)	9.8

3.2.1 Engine fuel

The fuel compositions used by *Politecnico di Torino* are three: firstly, CNG fuel composition which mainly consists in CH_4 and less important species such as C_2H_6 , C_4H_{10} and CO_2 . Secondly, 15% and 25% of volume of hydrogen have been added in order to try to reduce the pollutant emissions.

In the previous works of Lorenzo Testa [4] and Luca Ferretti [5], the CNG and HCNG-15 fuel compositions have been treated. This thesis project will continue

the study of the HCNG-15 (in a different operating point) and will introduce the model for HCNG-25 fuel. The Table 2 shows the three fuel compositions:

	CNG	HCNG-15	HCNG-25
CH₄	98%	83.3%	73.5%
C₂H₆	1%	0.85%	0.75%
CO₂	1%	0.85%	0.75%
H₂	0%	15%	25%

Table 2: Fuel compositions

3.2.2 Intake system

The engine intake system of the Fiat FIRE is composed by:

- **Indirect air mass flow rate meter (*Speed Density-Lambda type*):** it measures the absolute pressure p_a and the temperature T_a in the intake manifold. Thus, the air mass flow rate is computed indirectly from these two parameters.
- **Wired controlled butterfly valve:** its role is to control the engine load, thus a valve position sensor (TPS) and a Idle load actuator (IAC) are mounted on the valve. The Figure 3.2 shows the throttle body layout.
- **IAC actuator:** the main function is to ensure sufficient air so that the engine can win the friction work, while continuing to work when the throttle is closed. It is installed next to the butterfly valve and is made by a stepping motor with high accuracy, resolution and velocity.
- **Centifugal radial compressor:** manufactured by IHI Corporation, it allows to force extra air into the combustion chamber in order to increase the engine's efficiency. The Figure 3(a) shows this component.
- **Intercooler air-water:** since during the compression the gas temperature increases, an intercooler is needed in order to increment the density and also the volumetric efficiency, with the benefit of more air in the chamber. This device is shown in Figure 3(b) .

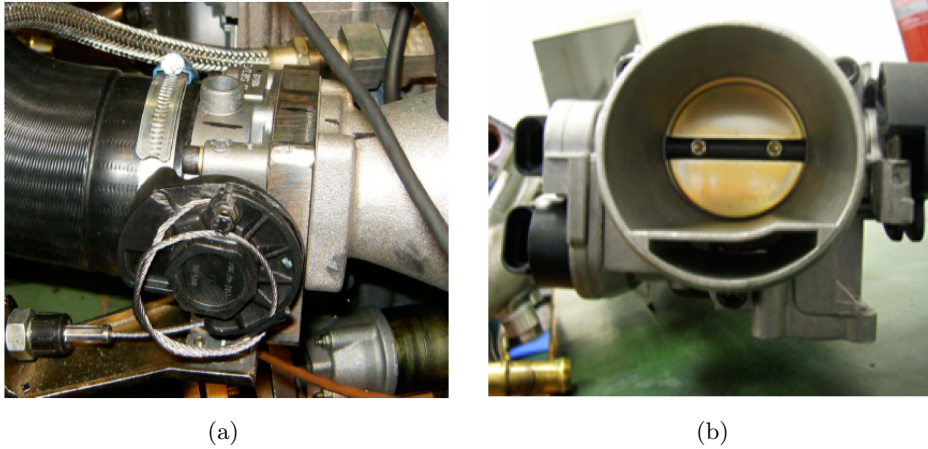


Figure 3.2: Throttle body: (a) wire control of throttle opening ; (b) frontal view of butterfly valve

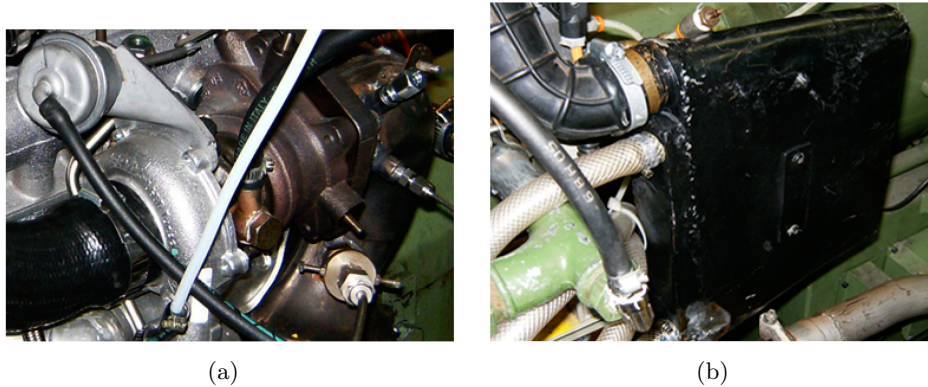


Figure 3.3: (a) Turbocharger ; (b) Intercooler air-water

3.2.3 Fuel supply system

The fuel supply system mounted on the engine consists in three main components:

- **Tartarini Meta M pressure regulator:** it is a self regulated valve, made in brass (Figure 4(a)). Calibrated to give an outlet pressure about 8.9 bar and inlet pressure between 15 and 200 bar. In the test bench we supply the fuel at constant pressure of 20 bar. It is equipped with *Piezoresistive high pressure sensor Keller Pa 22M* (Figure 4(b)), *Piezoresistive low pressure sensor Kavlico P4000* (Figure 4(c)) and *Type K thermocouple*.
- **Injectors rail:** it connects the injectors dedicated for each cylinder; the main difference respect the gasoline injection system is the bigger nozzle diameter and the higher pressure (8÷10 bar). It is shown in Figure 3.5 .

- Gas electro-injectors per cylinder.

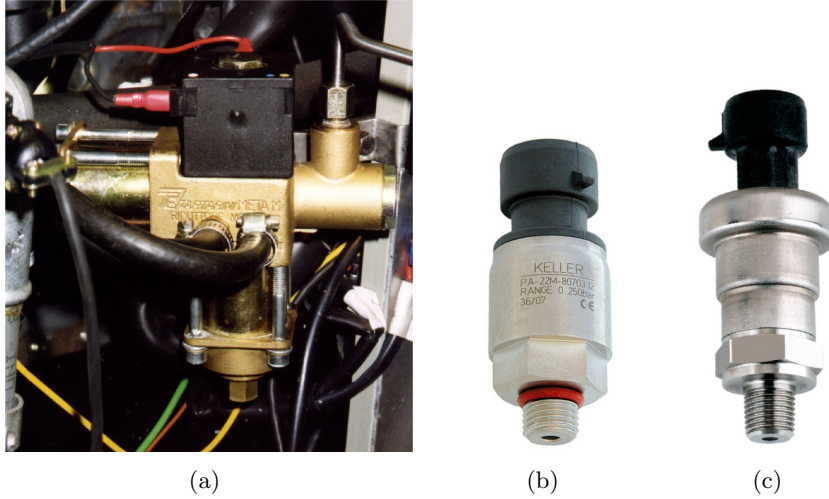


Figure 3.4: (a) *Tartarini* pressure regulator; (b) High pressure sensor *Kelle Pa 22 M*; (c) Low pressure sensor *Kavlico P4000*

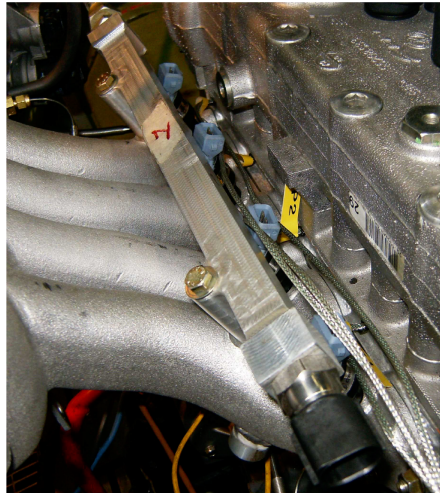


Figure 3.5: Gas feeding rail

3.2.4 Sensors

The measuring system is composed by different sensors and allows monitoring the main physical quantities (e.g. temperature, pressure, mass flow rate, gas components mass fraction). These sensors can be split in four main groups:

- on engine sensors;
- intake system sensors;

- exhaust system sensors;
- on brake sensors.

On engine sensors

The data measured by these sensors are:

- Pressure and temperature in inlet manifold (HF: p_{AMAP} ; LF p_{AMAP}, T_{AMAP});
- pressure in the chamber for each cylinder ($p_{Cyl\#}^1$);
- pressure in the 4 intake runners ($p_{Arun\#}$) and in the exhaust ones ($p_{Erun\#}$);
- additional pressure sensor at the inlet runner of cylinder 2 to analyse the pressure wave in the manifold (p_{Arun22});
- temperature in the inlet ($T_{Arun\#}$) and outlet runners ($T_{Erun\#}$);
- pressure and temperature in the compressor inlet and outlet (inlet: p_{AbTC}, T_{AHyg} ; outlet: p_{AaTC}, T_{AaTC});
- pressure and temperature in the turbine inlet and outlet (inlet: p_{EbTrb}, T_{EbTrb} ; outlet: p_{EaTrb}, T_{EaTrb});
- water and temperature at the inlet and outlet of engine cooling system (T_{H2Oin}, T_{H2Oout});
- pressure and temperature of lubrication oil (p_{oil}, T_{oil}).

Intake system sensors

The intake measurement system , whose data are very crucial for the mixture control, gives the following data:

- environment temperature e pressure (p_{env}, T_{env});
- air mass flow rate (M_A);
- pressure and temperature in the setting chamber (p_{Ainlet}, T_{Ainlet});
- fuel mass flow rate, consumption and temperature (M_F, M_{FFreq}, T_F);
- pressure and temperature after the intercooler (p_{AaIC}, T_{AaIC});
- water temperature at the intercultural inlet and outlet (T_{H2ObIC}, T_{H2OaIC}).

¹the # stands for cylinder number, i.e. $\# = 1, 2, 3, 4$.

Exhaust system sensors

The exhaust measurement system allows monitoring the exhaust gas through the following data:

- air to fuel ratio (A/F) (UEGO_L,UEGO_R);
- pollutions (E_THC, E_CH4, E_HCO, E_LCO, E_CO2, E_O2, E_CO2EGR, E_NOx);

the 2 lambda-sensors made by NGK and mounted at the catalyst exit are known as Universal Exhaust Gas Oxygen (UEGO) sensors. The Figure 3.6 shows the output signal of the sensor which obviously is an electrical voltage.

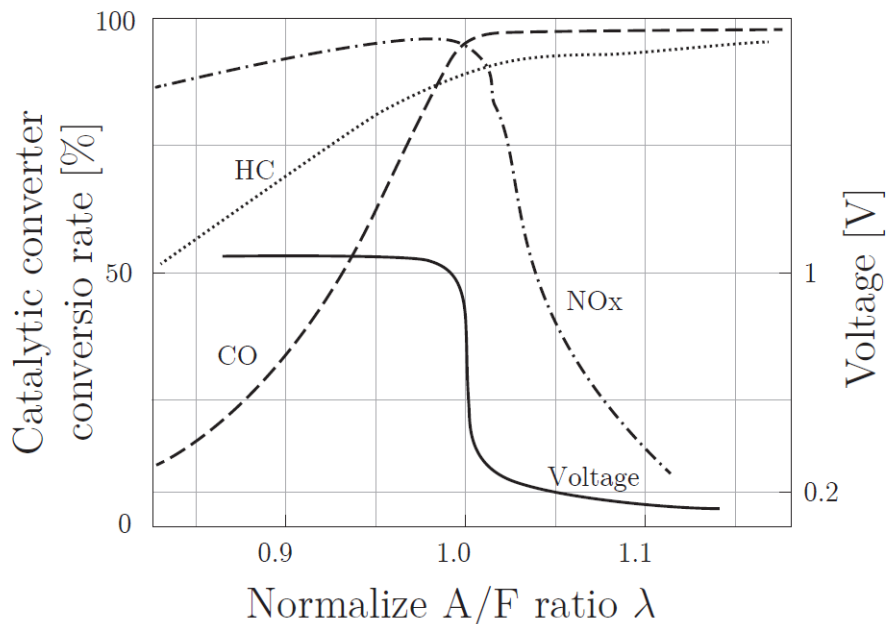


Figure 3.6: Lambda-sensor characteristic

On brake sensors

The following data are collected by using a dynamo-meter FE 260-S *Borghini and Savieri* (Figure 3.7) and a high accuracy incremental encoder 59 CA TX made by *Elcis*.

- Engine torque and speed (Torque, Speed);
- High accuracy speed (Speedenc).

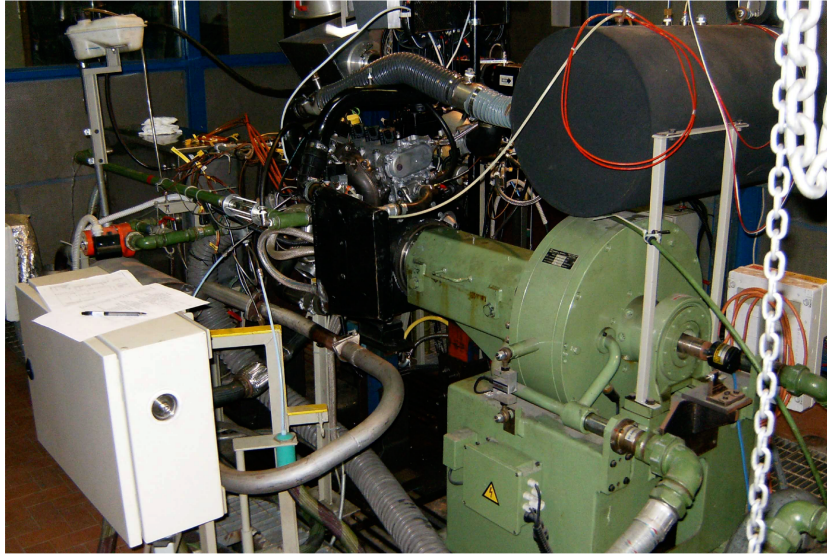


Figure 3.7: Dynamo-meter FE 260-S *Borghini and Savieri*

To sum up, all the sensors and instruments used are shown in their correct position in the following experimental layout:

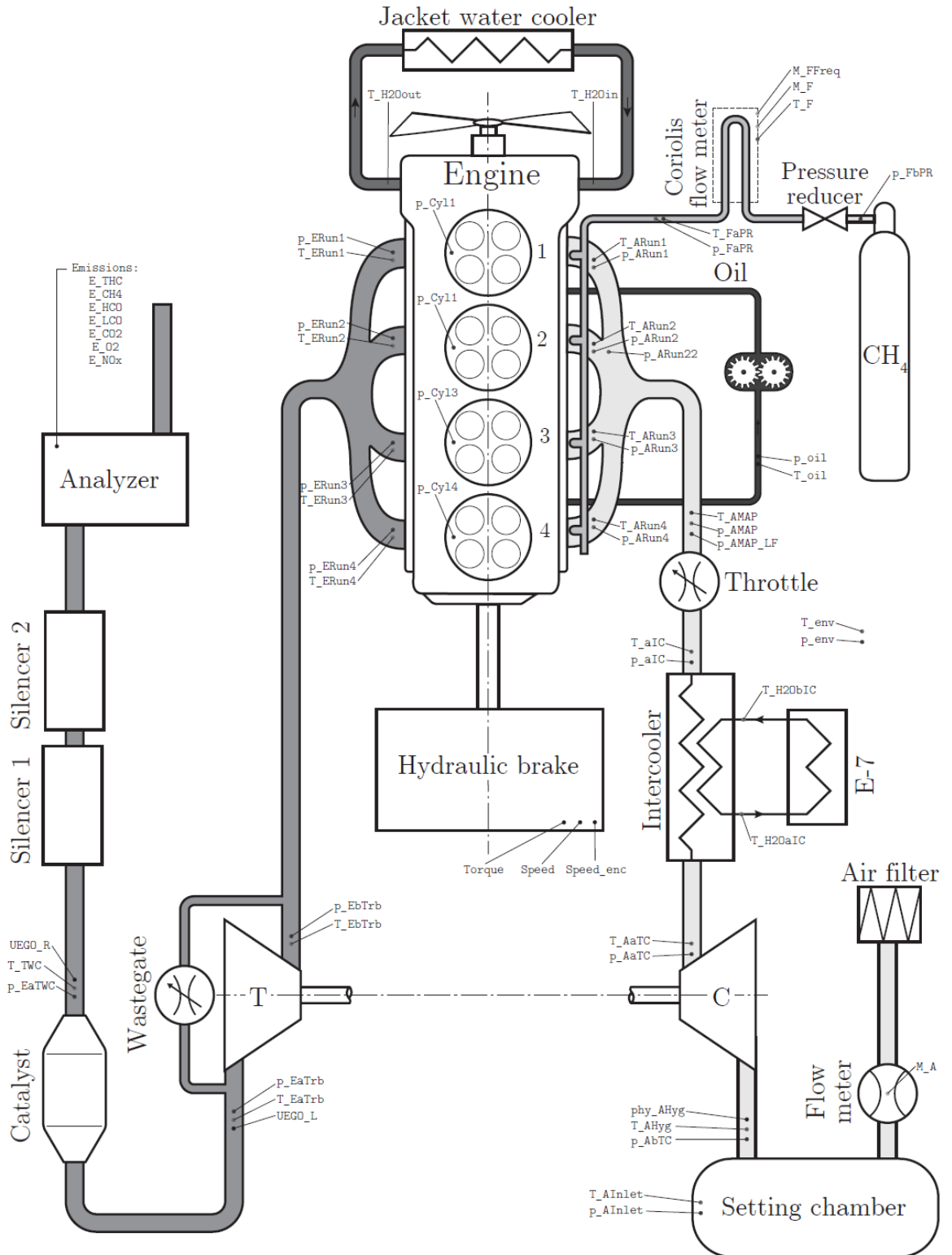


Figure 3.8: Experimental layout

3.3 Experimental parameters for model validation

In this chapter the parameters to consider for the validation of the CFD model are described. It is important to underline that since the boundary conditions available are referred just to the cylinder 1, only that cylinder is considered in this thesis work. Consequently, the experimental data will be manipulated to obtain an *average cycle* (see the next chapter).

The most important experimental data for the validation are:

- average pressure in cylinder 1, $p_{cyl}(\theta)$;
- fuel mass flow rate, \dot{m}_f ;
- air-fuel ratio, α ;
- average exhaust concentration of pollutant emissions: \tilde{x}_{CO} , \tilde{x}_{CO_2} , \tilde{x}_{NO_x} , \tilde{x}_{HC}

and they can be found as follows:

	Name	Sheet	Range
$p_{cyl}(\theta)$ [bar]	p_Cyl1.ens	p_Cyl1.ens	B2:B7201
\dot{m}_f [kg/h]	M_FFReq	p2000_360_04 (root)	K2
α [-]	a_LCO or a_HCO	LFStatistic	BB2 or BJ2 ^a
\tilde{x}_{CO} [ppm]	E_HCO or E_LCO	LFStatistic	AN2 or A02 ^b
\tilde{x}_{CO_2} [ppm]	E_CO2	LFStatistic	AP2
\tilde{x}_{NO_x} [ppm]	E_NOx	LFStatistic	AS2
\tilde{x}_{HC} [ppm]	E_THC	LFStatistic	AL2

Table 3: Where find the parameter in the TSMS file

^aIf A02 < 4996 take cell BB2. Else if A02 ≥ 4996 and AN2 > A02 then take cell BJ2

^bIf A02 < 4996 take cell A02. Else if A02 ≥ 4996 and AN2 > A02 then take cell AN2

The CFD model can be split in two main problems: *Fluid dynamic problem* and *Thermal problem (combustion)*.

Fluid dynamic problem

The *Fluid dynamic problem* gives the velocity field \mathbf{v} and pressure distribution p by using the Navier-Stokes equations. To check the model validity, we will focus on the following data:

p_{int} mean intake pressure in cylinder 1 [bar].

m_f fuel mass in the cylinder [kg]. It is the the value of fuel entered after the suction phase. It is calculated by CONVERGE and can be found in the

file `species_mass_region1.out`². While, for experimental fuel mass we derive it from the fuel mass flow rate:

$$m_{f,exp}[\text{mg}] = \frac{\dot{m}_f[\text{kg/h}]/3600}{n[\text{rpm}]/60} \cdot \frac{10^3}{2} \quad (3.1)$$

m_{cyl} trapped mass in the cylinder [kg]. It is the value of the total mass (air and fuel mixture) in the chamber after the intake phase. It can be computed with two different methods:

1. without considering the combustion residues: involving the air-fuel ratio α and the fuel mass m_f , the trapped mass can be computed as:

$$m_{cyl,exp} = m_{f,exp}(1 + \alpha) \quad (3.2)$$

2. considering the combustion residues: it can be computed as

$$m_{cyl,exp} = m_{f,exp}(1 + \alpha)(1 + x_r) \quad (3.3)$$

where x_r is the mass fraction of residue in the cylinder. It is possible to assume that the percentage of residues in the model is close to the experimental one:

$$x_r = x_{r,model} \approx x_{r,exp} \quad (3.4)$$

To calculate that value, we have to taking into account the model total mass $m_{cyl,model}(\theta_0)$ and the mass of CO_2 , $m_{\text{CO}_2,model}(\theta_1)$ in the chamber. These values can be found in the output files of CONVERGE called `thermo_region1.out` and `species_mass_region1.out`.

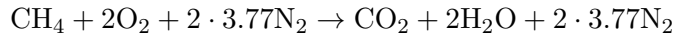
Firstly, we obtain the total mass by taking a value between the intake valve closing angle (θ_{IVC}) and the exhaust valve opening angle (θ_{EVO}):

$$\theta_{IVC} < \theta_0 < \theta_{EVO}$$

Then we compute the mass of CO_2 considering the intake valve closing angle (θ_{IVC}) and the spark advance angle (θ_{SA}):

$$\theta_{IVC} < \theta_1 < \theta_{SA}$$

Manipulating the balance equation of the combustion we can obtain the mass fraction of CO_2 in the exhaust (x_{CO_2}):



$$\Rightarrow m_f(1 + \alpha) = \frac{m_f}{\mathcal{M}_{\text{CH}_4}} (\mathcal{M}_{\text{CO}_2} + 2 \cdot \mathcal{M}_{\text{H}_2\text{O}} + 2 \cdot 3.77 \cdot \mathcal{M}_{\text{N}_2}) = m_{exh}$$

²In the case setup used in this thesis project, the region 0 is the exhaust, the region 1 is the cylinder and the region 2 is the intake.

$$\Rightarrow \frac{m_{CO_2}}{m_{exh}} = x_{CO_2} = \frac{\mathcal{M}_{CO_2}}{\mathcal{M}_{CH_4}(1 + \alpha)} = \frac{44.01[\text{kg/kmol}]}{16.04[\text{kg/kmol}](1 + 17.09)} = 0.152$$

Thus, the mass fraction of combustion residues can be obtained by:

$$x_r = x_{r,model} = \frac{m_{CO_2,model}}{x_{CO_2} \cdot m_{cyl,exp}} \quad (3.5)$$

where $m_{cyl,exp}$ can be computed through eq. 3.2. Now, it is possible to compute the new trapped mass in the chamber with combustion residues following the eq. 3.3.

In this thesis project, the method number 2 is the one considered.

Thermal problem (Combustion)

p_{peak} peak pressure in cylinder 1 [bar].

HRR heat release in cylinder 1 [J/deg]. Heat losses through the walls are always present; for that reason it is necessary to make a distinction between *Gross-HRR* and *Net-HRR*, expressed as:

$$HRR_{Gross} = \frac{dQ_b}{d\theta} = \frac{k}{k-1} p \frac{dV}{d\theta} + \frac{1}{k+1} V \frac{dp}{d\theta} + \frac{dQ_l}{d\theta} \quad (3.6)$$

$$HRR_{Net} = \frac{dQ_b}{d\theta} - \frac{dQ_l}{d\theta} = \frac{k}{k-1} p \frac{dV}{d\theta} + \frac{1}{k+1} V \frac{dp}{d\theta} \quad (3.7)$$

where $\frac{dQ_b}{d\theta}$ is the heat supplied by the burning fuel, $\frac{dQ_l}{d\theta}$ is the heat losses through the walls and k is the heat capacity ratio. As the equations show, the HRR depends on the pressure: it will be a very important parameter for the study of the combustion because a slightly pressure variation produces a high heat release variation.

Since it is very difficult to determine the losses, in this thesis project the *Net-HRR* will be considered. Finally, the evaluation of the heat capacity factor is made by Michael F.J. Brunt methodology [12] according to the following equation:

$$k = 1.338 - 6 \cdot 10^{-5} \cdot T + 6 \cdot 10^{-8} \cdot T^2 \quad (3.8)$$

IHR integrated heat release in cylinder 1 [J]. Integrating the eq.3.7 over the interval between (θ_{SA}) and (θ_{EVO}) we obtain:

$$IHR = Q_b - Q_l = \int_{\theta_{SA}}^{\theta_{EVO}} \left(\frac{dQ_b}{d\theta} - \frac{dQ_l}{d\theta} \right) d\theta \quad (3.9)$$

\tilde{x}_{XY} average exhaust concentration of a generic species XY [ppm]. The model molar fraction, $\tilde{x}_{XY,model}$, is computed by CONVERGE and can be found

in the output file `emission_region0.out`. Thus, its value as [ppm] is $\tilde{x}_{XY,model} \times 10^6$ [1].

However, since the experimental measurements of CO and CO₂ have been made on a dry basis, further corrections on these values must be done; in particular:

$$\tilde{x}_{CO,model,dry} = \frac{\tilde{x}_{CO,model}}{1 - \tilde{x}_{H_2O,model}} \quad (3.10)$$

the same equation will be applied to \tilde{x}_{CO_2} [13]. From now, for the sake of simplicity it is possible to denote $\tilde{x}_{CO,model,dry}$ and $\tilde{x}_{CO_2,model,dry}$ as $\tilde{x}_{CO,model}$ and $\tilde{x}_{CO_2,model}$ respectively.

3.4 Data conditioning

Natural gas engines are characterized by a remarkable cycle-to-cycle variability (CCV). This phenomenon consists in a fluctuation of the combustion intensity, strictly related to the pressure profile (which increases and decreases continuously). Thus, choosing the “most representative engine cycle” is essential to carry out the analysis of the combustion.

For that reason, statistical examinations have been done through the *Ensemble Average method*: it consists in computing all engine cycles through a GNU-Octave script, obtaining an average of experimental pressure at given crank angles, the so-called *Experimental ensemble average*.

Unfortunately, this pressure profile is not a real cycle. In this thesis project the number of simulation cycles computed for each case is not high (3 or 4 cycles per case); thus, the model validation has been performed by referring to the experimental cycle whose pressure profile is the closest to the experimental ensemble average. Then, this pressure profile will be compared to the simulation cycles: the *best simulation model* will be the one whose pressure profile is the closest to the experimental ensemble average.

It is also possible to calculate the *experimental maximum cycle* and the *experimental lowest cycle*, which are the boundaries of the CCV. In this way, it will be possible to determine if the simulation results can be considered acceptable. Finally, after calculating the pressure profile, it is possible to compute other parameters such as *HRR* and *IHR*. Furthermore, it is worth recalling that in this thesis project all the parameters studied are referred just to the cylinder 1.

[5]

3.5 Operating point considered

The engine operating points for the CFD model validation are:

Engine speed [rpm]	bmep [bar]	lambda [-]	Fuel composition
2000	3.6	1	HCNG-15
2000	3.6	1	HCNG-25

Table 4: Engine operating points considered

3.5.1 O.P. 2000 [rpm] x 3.6 [bar] x lambda=1: HCNG-15

This operating point is characterized by:

- Spark advance = 22 deg;
- Air-to-Fuel ratio $\alpha = 17.01308217$;
- Fuel mass flow rate $\dot{m}_f = 2.122$ [kg/h];
- Number of engine cycles measured = 100;
- CO emissions $\tilde{x}_{CO} = 5572.54$ [ppm];
- CO₂ emissions $\tilde{x}_{CO_2} = 103857.20$ [ppm];
- NO_x emissions $\tilde{x}_{NO_x} = 1880.82$ [ppm];
- HC emissions $\tilde{x}_{HC} = 327.87$ [ppm];

The figures 3.9 and 3.10 show the pressure profile of this operating point; as it can be noticed there is a remarkable effect of the cycle to cycle variability. The peak pressure of the experimental closest cycle is about 2.25 MPa and it happens at around 735 crank angle degree.

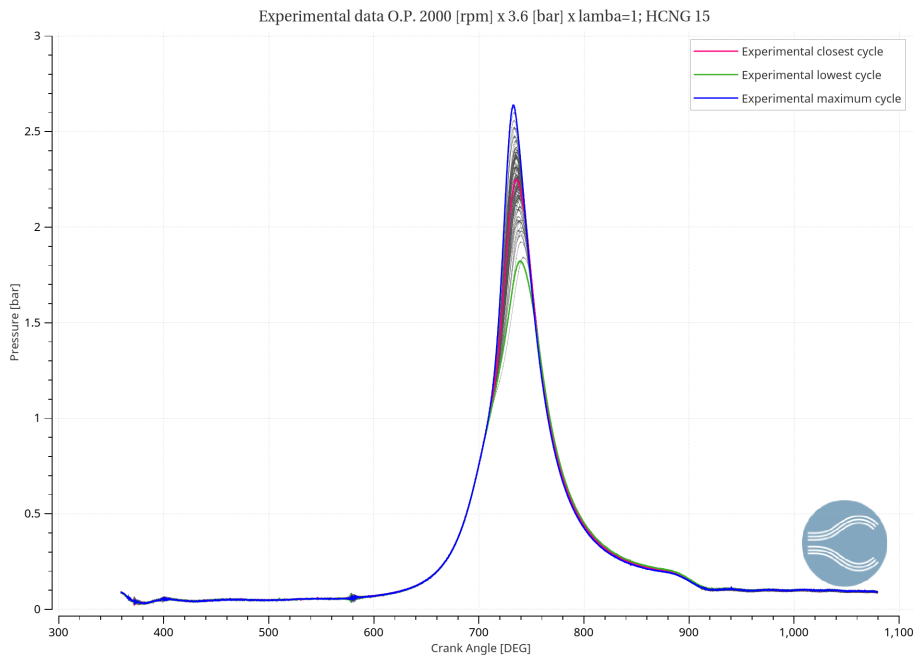


Figure 3.9: Experimental data plot: Pressure in cylinder 1; 2000x3.6x1; HCNG 15

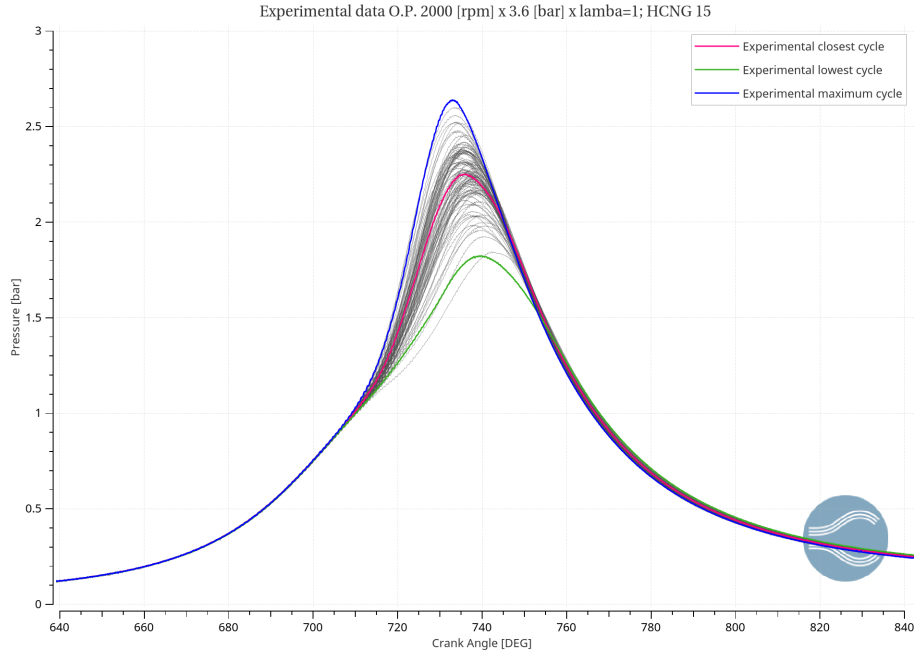


Figure 3.10: Experimental data plot: zoom around peak pressure in cylinder 1; 2000x3.6x1; HCNG 15

3.5.2 O.P. 2000 [rpm] x 3.6 [bar] x lambda=1: HCNG-25

This is the same engine operating point, but with HCNG 25 fuel. It is characterized by:

- Spark advance = 21 deg;
- Air-to-Fuel ratio $\alpha = 17.37336349$;
- Fuel mass flow rate $\dot{m}_f = 2.11196$ [kg/h];
- Number of engine cycles measured = 100;
- CO emissions $\tilde{x}_{CO} = 5650.9$ [ppm];
- CO₂ emissions $\tilde{x}_{CO_2} = 101059.14$ [ppm];
- NO_x emissions $\tilde{x}_{NO_x} = 1818.72$ [ppm];
- HC emissions $\tilde{x}_{HC} = 281.78$ [ppm];

The figures 3.11 and 3.12 show the experimental closest, lowest and maximum cycle of the pressure: the peak pressure of the closest cycle is about 2.25 MPa and it happens at around 735 crank angle degree.

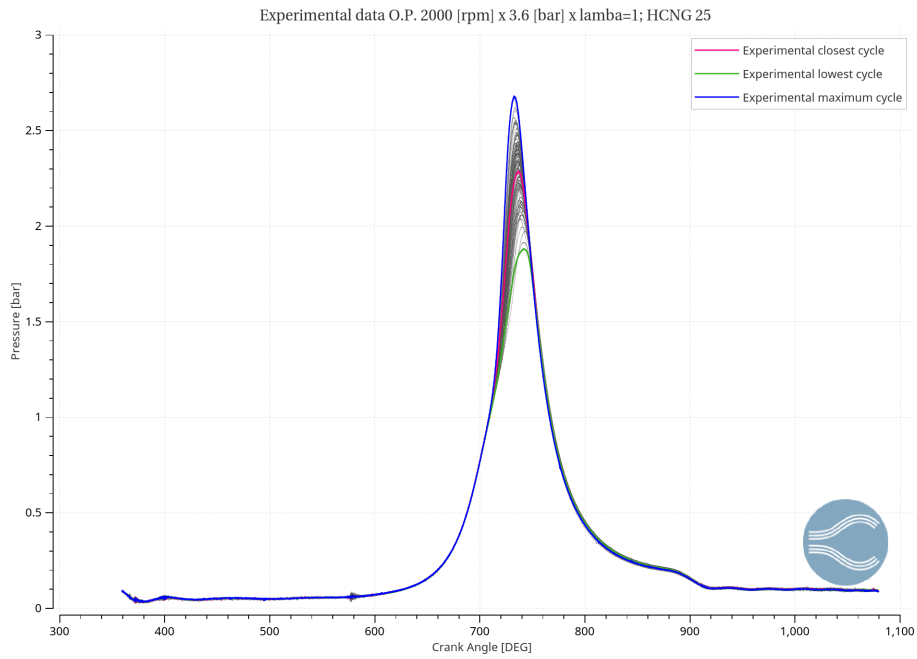


Figure 3.11: Experimental data plot: Pressure in cylinder 1; 2000x3.6x1; HCNG 25

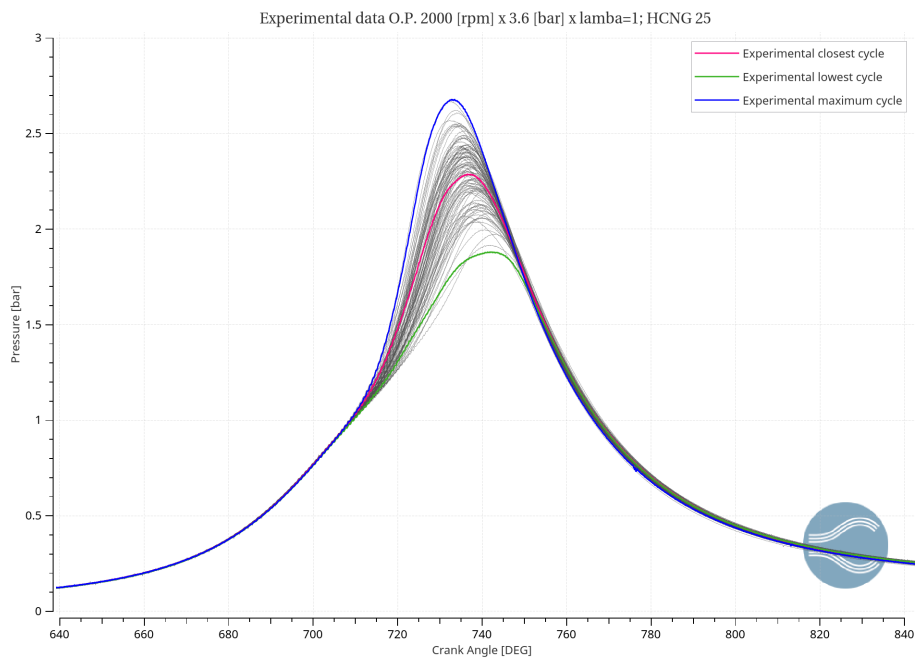


Figure 3.12: Experimental data plot: Pressure in cylinder 1; 2000x3.6x1; HCNG 25

4 CNG/HCNG Engine: Case Setup

This section is dedicate to the discussion about the Engine CAD model and its main features. Starting from the geometry, the whole Case Setup will be introduced, explaining which are the strategies in CONVERGE to set up the boundary and initial conditions, the turbulence modeling as well as the source modeling and the grid control.

4.1 Geometry and regions

The 3-D geometry of the *Fiat FIRE 1.4l 16V Turbo CNG* engine has been provided by CRF as a CAD file. The model is shown in the figures :

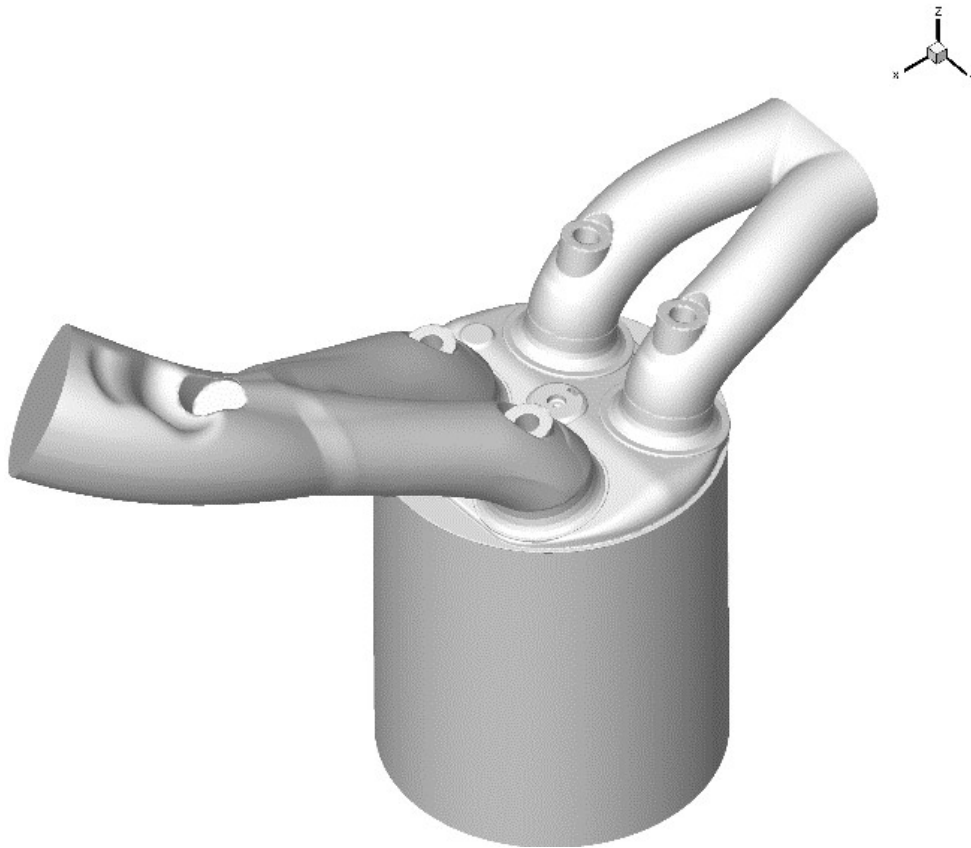


Figure 4.1: Engine CAD geometry: isometric view

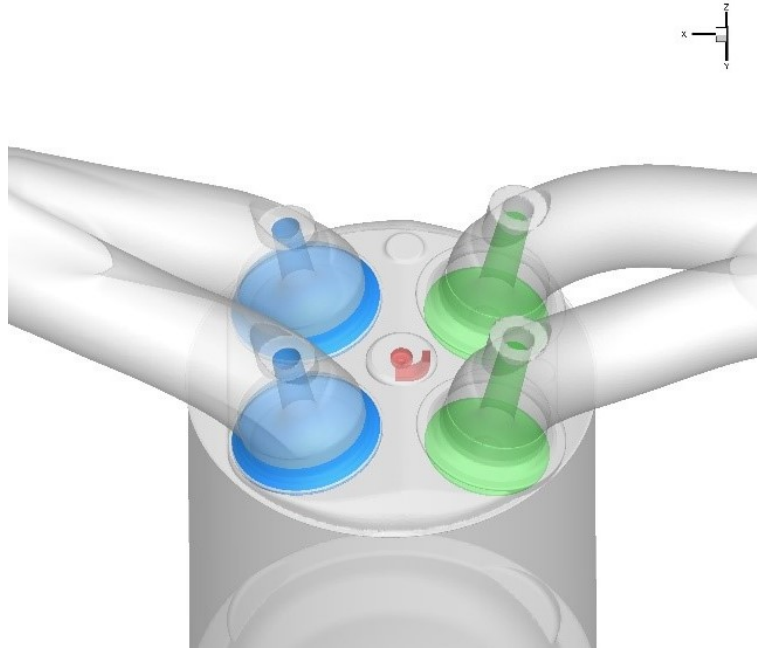


Figure 4.2: Engine CAD geometry: focus on valves and spark plug

The Control Volume V of the engine can be split into three regions (Fig.4.3):

- **Exhaust system**, V_0 or *Region 0*. It is composed by the exhaust runner, exhaust valve top and angle and the outflow. In CONVERGE it is described by `region0`;
- **Cylinder**, V_1 or *Region 1*. It is composed by head, piston, liner, spark plug and intake valve bottom. In CONVERGE it is described by `region1`;
- **Intake system**, V_2 or *Region 2*. It is composed by the intake port, intake valve top and angle and the inflow port. In CONVERGE it is describes by `region2`.

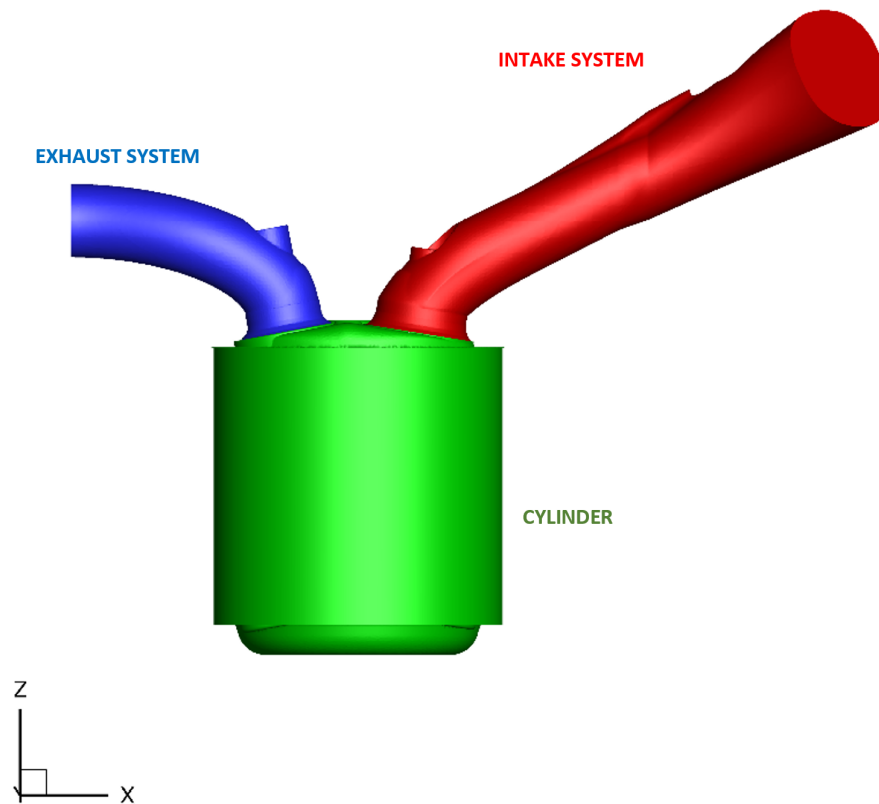


Figure 4.3: Regions

The regions are also subdivided into boundaries (Fig.4.4):

- S_0 is the surface of the outlet runner and exhaust valve top and angle;
- S_1 is the surface that include the piston head, liner, cylinder head, spark plug and valves bottom;
- S_2 is the surface of the inlet runner and intake valve top and angle;
- S_{in} is the inflow port;
- S_{out} is the outflow port.

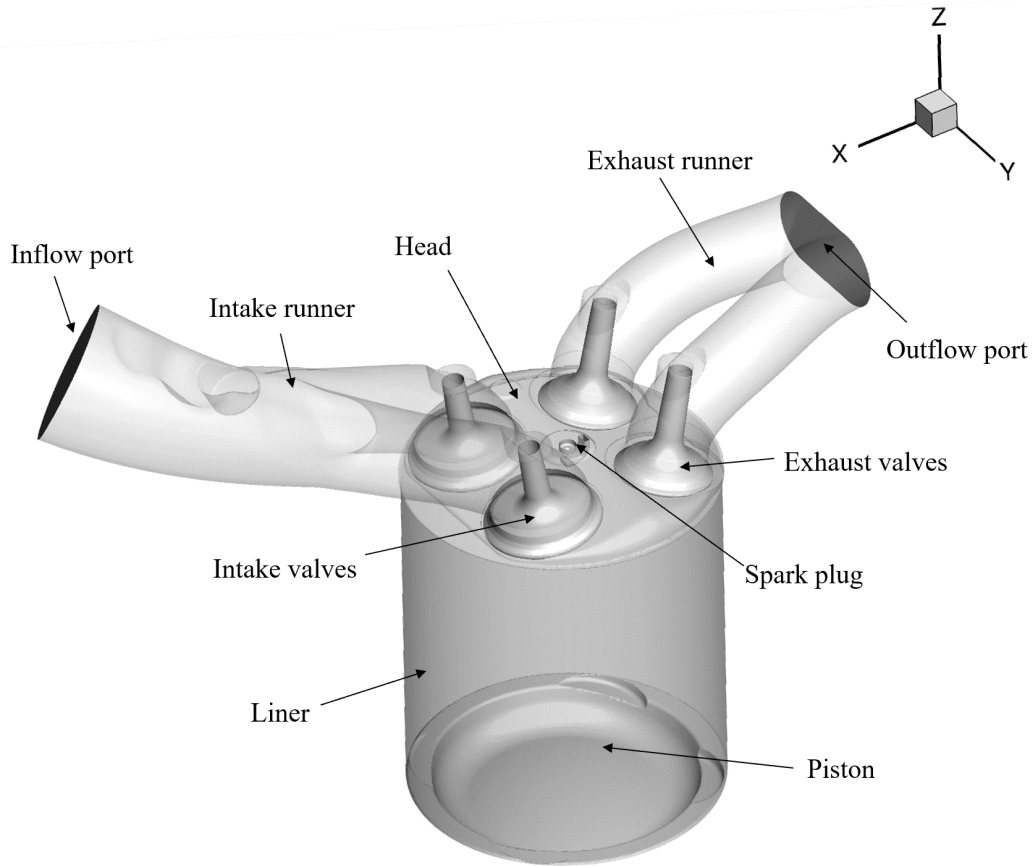


Figure 4.4: Boundaries

4.2 Regions Initialization and Boundary conditions

The regions initialization and the boundary conditions are a set of input parameters, essential to solve the differential equations discussed above. In this section we describe how to find and how to set up these parameters in CONVERGE.

4.2.1 Regions Initialization

The initialization of the regions defines all the thermodynamic and chemical characteristics of each region. In addition to the mass fraction present at the simulation start time, also the pressure and temperature have to be set. In particular we set:

- $T_{int,0}$ ³: initial gases temperature in the intake runner [K];
- $T_{cyl,0}$: initial gases temperature in the cylinder [K];
- $T_{exh,0}$: initial gases temperature in the exhaust runner [K].

³the subscript 0 represents the simulation start time, θ_0

The simulation start time is $\theta_0 = 130$ CAD, exactly before the exhaust valve opening (EVO). Thus, the species composition in the regions has to be:

- in the intake system: fuel composition (see chapter *Fuel composition*);
- in the exhaust system and cylinder: burned species composition.

4.2.2 Boundary conditions

The boundary conditions have been computed by a *Matlab* script, provided by Politecnico di Torino University.

First of all, an important assumption is needed: the engine temperature reaches the steady state value; therefore, constant temperature are set:

- T_{cyl} : cylinder wall temperature⁴ [K]
- T_{int} : intake duct wall temperature [K]
- T_{exh} : exhaust duct wall temperature [K]
- T_{inlet} : inlet temperature [K]
- T_{outlet} : outlet temperature [K]

Concerning the pressure, we also set two values for the intake and exhaust port, using the data obtained from the traducers and computed by the *Matlab* script:

- p_{int} : intake pressure [Pa]
- p_{exh} : exhaust pressure [Pa]

The Table 5 and the Fig.4.5 show how to find and how to set the initial and boundary conditions (for further information about data treatment with the *Matlab* script see [11]):

⁴Since it is hard to measure the temperature near to the spark plug, we set a spark plug wall temperature at arbitrary value of 550 K and a spark plug electrode wall temperature of 600 K

	Name	Sheet	Range
$T_{int,0}$	T_AMAP	LFStatistic	B2
$T_{exh,0}$	T_ERun1	LFStatistic	G2
$T_{cyl,0}^a$	T_ERun1	LFStatistic	G2
T_{cyl}		$T_{cyl} = \frac{T_{H_2O,in} + T_{H_2O,out}}{2} + 70$	
$T_{H_2O,in}$	T_H2Oin	LFStatistic	N2
$T_{H_2O,out}$	T_H2Oout	LFStatistic	O2
T_{int}		$T_{int} = T_{cyl} - 50$	
T_{exh}		$T_{exh} = T_{cyl} + 50$	
T_{inlet}	T_AMAP	LFStatistic	B2
T_{outlet}	T_ERun1	LFStatistic	G2
p_{int}	p_ARun22	HF	I2:I734401
p_{exh}	p_ERun1	HF	M2:M734401

Table 5: where to find the value for ICs and BCs

^asince the starting phase is the exhaust phase, then $T_{cyl,0} = T_{exh,0}$

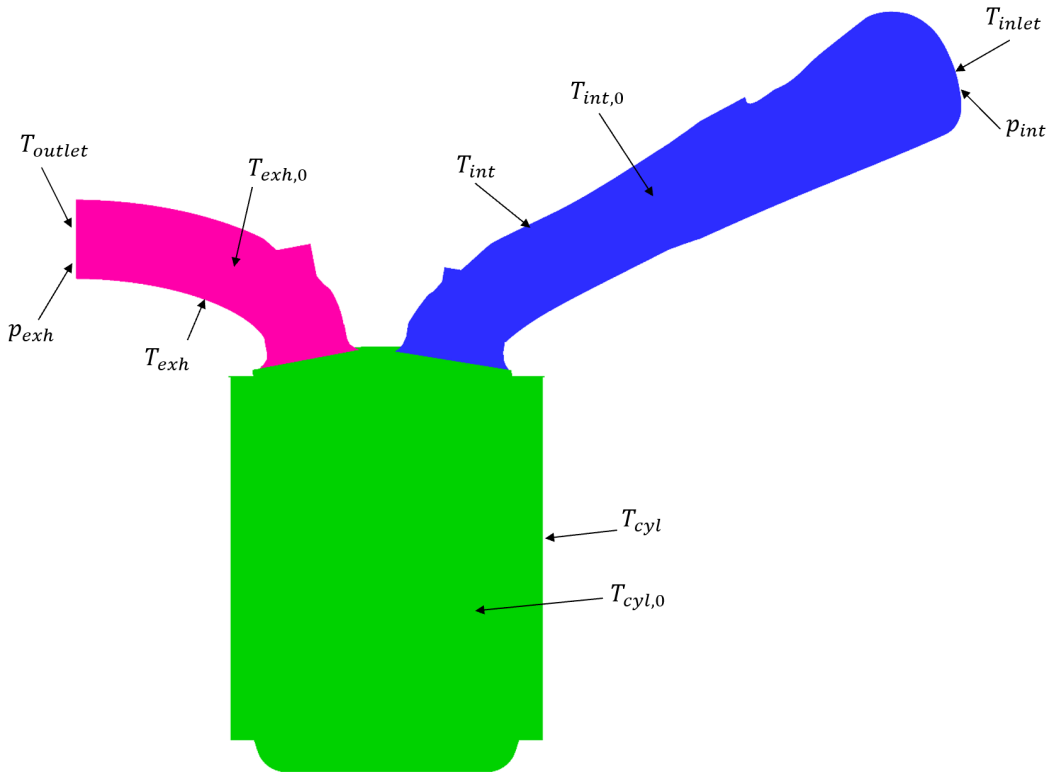


Figure 4.5: schematic representations of the Boundary and Initial condition

4.3 Fuel composition

Another important parameter to set in the Case Setup is the fuel composition. In particular, it must be set as mass fraction and as boundary condition of the inflow.

As mentioned above, in the previous works of Lorenzo Testa and Luca Ferretti two different fuel compositions have been used: CNG and HCNG 15. In this thesis project, the fuel compositions are HCNG 15 and HCNG 25.

Concerning HCNG 15, the percentage of the components into the mixture is:

- $\text{CH}_4 = 83.3\%$
- $\text{C}_2\text{H}_6 = 0.85\%$
- $\text{CO}_2 = 0.85\%$
- $\text{H}_2 = 15\%$

For the HCNG 25 fuel composition the same ratios between the species have been adopted, but this time with 25% of hydrogen; thus:

- $\text{CH}_4 = 73.5\%$
- $\text{C}_2\text{H}_6 = 0.75\%$
- $\text{CO}_2 = 0.75\%$
- $\text{H}_2 = 25\%$

4.4 Turbulence modeling

4.4.1 Introduction

The phenomenon of the turbulence is a key factor for the analysis of fluid flow problems in engineering applications. As already cited before, a fundamental parameter which describes the properties of the fluid is the Reynolds number, Re , defined as:

$$Re = u \cdot \frac{l}{\nu} \quad (4.1)$$

From a series of experiments on fluid systems, it has been demonstrated that under a specific value of the Re , the flow is smooth and, if the boundary conditions applied to the system do not change with time, the steady flow is called *Laminar flow*.

Conversely, the flow is described as *Turbulent flow* over a characteristic value of Re , which indicates that the particles have a random motion and their position cannot be described accurately.

In numerical environment, and in particular for the CFD simulations, there are several methods for capturing and modelling the turbulence and its properties:

- correlations as function between heat transfer and Reynolds number, Nusselt number or Prandtl numbers;
- integral equations, derived from the equations of motion;
- the **Turbulence models for Reynolds-Averaged-Navier-Stokes (RANS) equations**, focused on the effect of the turbulence on the mean flow properties. The equations of motion in fact are averaged over time, over coordinate in which the mean flow does not vary or over ensemble of realizations. The set of partial differential equations obtained, the RANS equations, contain also extra terms which will be modelled with different methods, for example the *k-ε model*;
- equations, or their Fourier transform, for the correlation of velocity components at two spatial points;
- the **Large Eddy Simulation (LES)** which, filtering and solving the larger eddies, is a compromise between one-point closure methods and direct numerical simulation. It is suitable for unsteady flows.
- the **Direct numerical simulation (DNS)**; it computes the mean flow and the turbulent velocity fluctuations. It involves a fine spatial grid and very small time steps, so the computational cost is very high.

For this thesis work the RANS equations and in particular the k-ε model have been used, because they are the best compromise in terms of accuracy of the results and computational cost.

[2] [4] [5]

4.4.2 The RANS equations and the k-ε model

In this thesis project, the RANS equations have been implemented with Renormalization Group, RNG, k - ε as turbulence model, which is based on two equations where the flow variables are decomposed in two terms:

$$u_i = \bar{u}_i + u_i' \quad (4.2)$$

where u_i is the instantaneous velocity, \bar{u}_i the ensemble mean velocity and u_i' the fluctuating velocity term.

Considering the continuity and momentum equations and substituting the eq.4.2:

$$\frac{\partial \bar{\rho}}{\partial t} + \frac{\partial \bar{\rho} \tilde{u}_j}{\partial x_j} = 0 \quad (4.3)$$

$$\frac{\partial \bar{\rho} \tilde{u}_i}{\partial t} + \frac{\partial \bar{\rho} \tilde{u}_i \tilde{u}_j}{\partial x_j} = -\frac{\partial \bar{P}}{\partial x_i} + \frac{\partial}{\partial x_j} \left[\mu \left(\frac{\partial \tilde{u}_i}{\partial x_j} + \frac{\partial \tilde{u}_j}{\partial x_i} \right) - \frac{2}{3} \mu \frac{\partial \tilde{u}_k}{\partial x_k} \delta_{ij} \right] + \frac{\partial}{\partial x_j} (-\bar{\rho} \tilde{u}_i' u_j') \quad (4.4)$$

where $\tilde{u}_i = \frac{\bar{\rho} \tilde{u}_i}{\bar{\rho}}$ is the *Favre* average.

The new generated by the ensemble averaging of the equations is the Reynolds stress τ_{ij} and it represents the effect of the turbulence:

$$\tau_{ij} = -\bar{\rho}\tilde{u}_i' u_j' \quad (4.5)$$

it is already included in eq.4.4.

The k - ε models are based on an effective turbulent viscosity as model Reynolds stress term. Thus, the turbulent convective mixing is modelled with an additional turbulent diffusion.

Only the Standard and RNG k - ε model has been used in this thesis, but actually there are others two models which are: *Rapid Distortion RNG k - ε model* and *Realizable RNG k - ε model*.

The *Standard and RNG k - ε model* is expressed by:

$$\tau_{ij} = -\bar{\rho}\tilde{u}_i' u_j' = 2 \cdot \mu_t S_{ij} - \frac{2}{3} \delta_{ij} \left(\rho k + \mu_t \frac{\partial \tilde{u}_i}{\partial x_i} \right) \quad (4.6)$$

where k is the turbulent kinetic energy defined as:

$$k = \frac{1}{2} \tilde{u}_i' u_j' \quad (4.7)$$

and μ_t is the turbulent viscosity:

$$\mu_t = c_\mu \rho \frac{k^2}{\varepsilon} \quad (4.8)$$

where c_μ is a model constant, ε is the dissipation of turbulent kinetic energy and S_{ij} is the mean strain rate tensor defined as:

$$S_{ij} = \frac{1}{2} \left(\frac{\partial \tilde{u}_i}{\partial x_j} + \frac{\partial \tilde{u}_j}{\partial x_i} \right) \quad (4.9)$$

The turbulent diffusion and conductivity terms used by the Standard k - ε and RNG models are respectively:

$$D_t = \frac{1}{Sc_t} \mu_t \quad (4.10)$$

$$K_t = \frac{1}{Pr_t} \mu_t c_p \quad (4.11)$$

where Sc_t is the turbulent Schmidt number, Pr_t is the turbulent Prandtl number, D_t is the turbulent diffusion and K_t is the turbulent conductivity.

Furthermore, the RANS k - ε requires two additional transport equations to solve the turbulent viscosity: one equation for the turbulent kinetic energy and one for the dissipation of ε .

The turbulent kinetic energy transport equation is given by:

$$\frac{\partial \rho k}{\partial t} + \frac{\partial \rho u_i k}{\partial x_i} = \tau_{ij} \frac{\partial u_i}{\partial x_j} + \frac{\partial}{\partial x_j} \frac{\mu}{Pr_k} \frac{\partial k}{\partial x_j} - \rho \varepsilon + \frac{c_s}{1.5} S_s \quad (4.12)$$

while the transport equation for the dissipation of turbulent kinetic energy is given by:

$$\frac{\partial \rho \varepsilon}{\partial t} + \frac{\partial \rho u_i \varepsilon}{\partial x_i} = \frac{\partial}{\partial x_j} \frac{\mu}{Pr_\varepsilon} \frac{\partial \varepsilon}{\partial x_j} - \rho \varepsilon + c_{\varepsilon 3} \rho \varepsilon \frac{\partial u_i}{\partial x_i} + \left(c_{\varepsilon 3} \frac{\partial u_i}{\partial x_j} \tau_{ij} - c_{\varepsilon 2} \rho \varepsilon + c_s S_s \right) \frac{\varepsilon}{k} + S + \rho R \quad (4.13)$$

where S is the user-supplied source term and S_s is the source term that represents the interactions with discrete phase. The $c_{\varepsilon i}$ terms are constants related with the compression and the expansion. Finally, the term R is given by:

$$R = \frac{C_\mu \eta^3 (1 - \eta/\eta_0) \varepsilon^2}{(1 + \beta \eta^3) k} \quad (4.14)$$

where $\eta = \frac{k}{\varepsilon} |S_{ij}|$
[6]

4.5 Source/sink modeling

CONVERGE allows to use different types of source, e.g. energy, momentum (in x,y and z direction), TKE and passives. In this thesis work, the Energy source type has been used which allows to define the spark, in different shapes: box, sphere, cylinder and circle. In this case, the shape adopted is the sphere.

The spark plug discharge can be split in:

- Breakdown: it occurs earlier and it has a short duration;
- Arc/glow: it take place after the breakdown and it has a longer duration

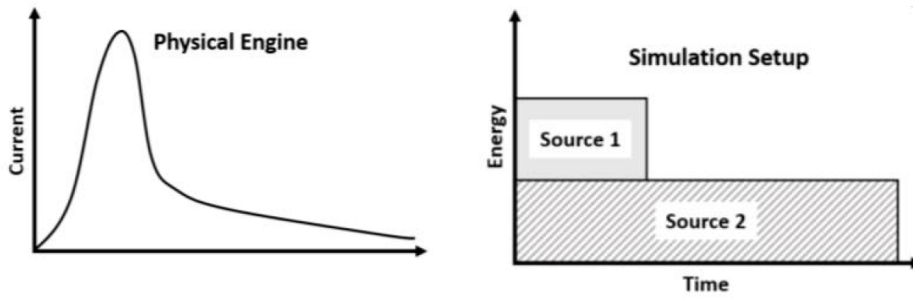


Figure 4.6: Source models

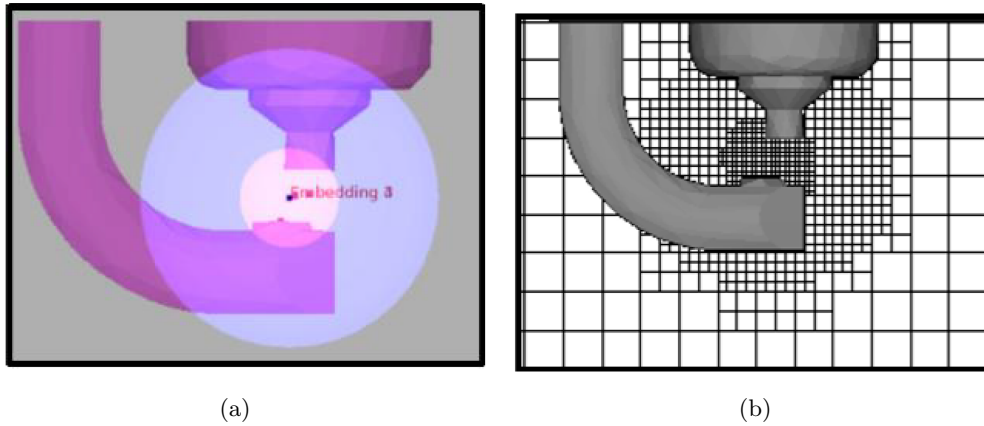


Figure 4.7: (a) source model on the geometry; (b) additional fixed embedding

4.6 Mesh settings

Since the operating point considered in this thesis work is the same studied by Lorenzo Testa, also the mesh settings chosen for this case setup are the same; in particular the *Coarse* mesh settings found in his work is the best compromise between good simulation results and computational cost.

The *Coarse* mesh settings is characterized by a base grid of $dx = 0.004\text{m}$; $dy = 0.004\text{m}$ and $dz = 0.004\text{m}$.

Fixed embedding settings

Concerning the *Fixed embedding settings*, the minimum mesh size of the spark area is 0.125mm ; for piston and head is 1mm . The table 6 shows all the *Fixed embedding settings* used for this case setup.

Head	<i>Type:</i>	Boundary
	<i>Mode:</i>	Permanent
	<i>Scale:</i>	2 (2 layers)
Liner	<i>Type:</i>	Boundary
	<i>Mode:</i>	Permanent
	<i>Scale:</i>	2 (2 layers)
Piston	<i>Type:</i>	Boundary
	<i>Mode:</i>	Permanent
	<i>Scale:</i>	2 (2 layers)
Intake valve angle	<i>Type:</i>	Boundary
	<i>Mode:</i>	Cyclic (340-600 deg)
	<i>Scale:</i>	3 (2 layers)
Intake valve top	<i>Type:</i>	Boundary
	<i>Mode:</i>	Cyclic (340-600 deg)
	<i>Scale:</i>	3 (2 layers)
Intake valve bottom	<i>Type:</i>	Boundary
	<i>Mode:</i>	Permanent
	<i>Scale:</i>	3 (2 layers)
Exhaust valve angle	<i>Type:</i>	Boundary
	<i>Mode:</i>	Cyclic (130-380 deg)
	<i>Scale:</i>	2 (2 layers)
Exhaust valve top	<i>Type:</i>	Boundary
	<i>Mode:</i>	Cyclic (130-380 deg)
	<i>Scale:</i>	3 (2 layers)
Exhaust valve bottom	<i>Type:</i>	Boundary
	<i>Mode:</i>	Permanent
	<i>Scale:</i>	3 (2 layers)
Spark 1	<i>Type:</i>	Sphere (r=0.005m)
	<i>Mode:</i>	Cyclic (690-750 deg)
	<i>Scale:</i>	4
Spark 2	<i>Type:</i>	Sphere (r=0.003m)
	<i>Mode:</i>	Cyclic (690-730 deg)
	<i>Scale:</i>	5

Table 6: *Coarse mesh: Fixed embedding settings*

AMR settings

The Adaptive mesh refinement settings are described on the following tables. The minimum mesh size is 0.5mm.

Intake port top	<i>Type:</i>	Boundary
	<i>Mode:</i>	Cyclic (340-600 deg)
	<i>Scale:</i>	2 (2 layers)
Intake port bottom	<i>Type:</i>	Boundary
	<i>Mode:</i>	Cyclic (340-600 deg)
	<i>Scale:</i>	2 (2 layers)
Exhaust port	<i>Type:</i>	Boundary
	<i>Mode:</i>	Cyclic (130-380 deg)
	<i>Scale:</i>	2 (2 layers)
Cylinder embed	<i>Type:</i>	Cylinder (r1=r2=0.04m)
	<i>Mode:</i>	Permanent
	<i>Scale:</i>	2

Table 7: *Coarse* mesh: AMR settings specifications

Cylinder	<i>Mode:</i>	Permanent
	<i>Velocity max embedding level:</i>	3
	<i>Velocity sub-grid criterion:</i>	1
	<i>Temperature max. embedding level:</i>	3
Intake system	<i>Mode:</i>	Permanent
	<i>Velocity max embedding level:</i>	3
	<i>Velocity sub-grid criterion:</i>	1
	Exhaust system	<i>Mode:</i>
<i>Velocity max embedding level:</i>		2
<i>Velocity sub-grid criterion:</i>		1
<i>Temperature max. embedding level:</i>		2
	<i>Temperature sub-grid criterion:</i>	2.5

5 Chemistry and Emissions modeling

5.1 Introduction

The combustion is one of the main processes in engineering applications and at the same time, is one of the most complex phenomena: it involves different physical and chemical processes like turbulent fluid flow, heat transfer and chemical kinetics. Basically, the combustion is a “*high-temperature exothermic redox chemical reaction between a fuel...and an oxidant*” which produce “...*a large amount of energy*” used for example to move objects (e.g. vehicles) and in general to make work through “...*all the machines where a thermal engine is installed*”.^[14]

The internal combustion engines are a typical application of this process. It is essential to understand in details the main features of the combustion, in order to predict the behaviour of the engine under different conditions (e.g. different engine speed and load) through (like in this work) CFD simulations. The combustion of ICEs can be divided in two categories: combustion in *Spark ignition engine (S.I.)* and in *Compression ignition engine (C.I.)*. In the first case, the fuel has a low reactivity; it is generally premixed outside the cylinder and then compressed. The combustion process starts by means of an electric spark and it propagates under a turbulent regime condition. For the *C.I.* engine, the fuels have a relatively short ignition delays; in this case there is not the electric spark in fact the combustion starts spontaneously thanks to high reactivity of the fuel. Furthermore, the combustion process in the *S.I.* engines can be subdivided in three steps:

- A small part of the fuel starts burning thanks to the spark electrical energy; the temperature and pressure inside the cylinder raise.
- Turbulent propagation of the flame, at high velocity (considered instantaneous). Thus, the volume of the chamber can be considered constant.
- Combustion completion.

Since in this thesis work a CNG/HCNG engine has been studied, only the combustion for *S.I.* engines has been modelled.

Chemical Kinetics

The *Chemical Kinetics* is a branch of the chemistry that studies the rate and mechanisms of chemical reactions, taking into account all the factors, like concentrations of reacts and temperature, which affect them. The oxidation of CH_4 , for example, is subdivided in a large number of intermediate reactions where chemical reaction rates control the rate of the combustion itself.

Let us consider for example a binary reaction, which means that two reactant

molecules called M_a and M_b collide and generate two product molecules, M_c and M_d :



A real binary reaction might be the oxidation of the hydrogen, according to:



Thus, the reaction rate is proportional to the product of the concentrations; in particular R^+ and R^- are the forward and backward direction reaction rate respectively:

$$R^+ = -\frac{d[M_a]^+}{dt} = \frac{d[M_c]^+}{dt} = k^+[M_a][M_b] \quad (5.3)$$

$$R^- = -\frac{d[M_c]^+}{dt} = \frac{d[M_a]^+}{dt} = k^-[M_c][M_d] \quad (5.4)$$

where k^+ and k^- are the rate constants in the forward and backward directions. They follows the Arrhenius form, which is:

$$k = A \cdot \exp\left(-\frac{E_A}{RT}\right) \quad (5.5)$$

where A is the pre-exponential factor (function of temperature) and E_A is the activation energy. The term $-\frac{E_A}{RT}$ is the Boltzmann factor: it represents the amount of collision with a higher energy than the activation energy.

The net reaction rate is:

$$R^+ - R^- = k^+[M_a][M_b] - k^-[M_c][M_d] \quad (5.6)$$

Thus, it is possible to write all the results in a general form:

$$\sum_{i=1}^n \nu_{R_i} M_{R_i} = \sum_{i=1}^m \nu_{P_i} M_{P_i} \quad (5.7)$$

where ν_i is the stoichiometric coefficient, R and P indicate the reactants and products respectively, n is the number of reactants and m the number of the products. So, by using this nomenclature:

$$R^+ = k^+ \prod_{i=1}^n [M_{R_i}]^{\nu_{R_i}} \quad (5.8)$$

$$R^- = k^- \prod_{i=1}^m [M_{P_i}]^{\nu_{P_i}} \quad (5.9)$$

Finally, deriving all in the time difference:

$$-\frac{d[M_{R_i}]}{dt} = \nu_{R_i}(R^+ - R^-) \quad (5.10)$$

$$-\frac{d[M_{P_i}]}{dt} = \nu_{P_i}(R^+ - R^-) \quad (5.11)$$

5.2 Combustion Models in CONVERGE

5.2.1 Models

The CONVERGE software allows the use of different combustion models, including models for general combustion, premixed and non-premixed combustion, turbulent and diesel combustion.

The model used in this thesis work is *SAGE detailed chemistry solver* which is one of the most accurate combustion models. However, other models are implemented in CONVERGE but they are less predictive and accurate, even if they require, at the same time, less computational power and time. We can split the models in *Premixed turbulent combustion models* and *Non-premixed turbulent combustion models*. The first group includes:

- Chemical Equilibrium (CEQ);
- G_Equation;
- Extended Coherent Flame Model (ECFM);
- Flamelet Generated Manifold (FGM);

while the second group is composed by:

- Characteristic Time Combustion (CTC);
- Shell ignition;
- Chemical Equilibrium (CEQ);
- Representative Interactive Flamelet (RIF);
- Extended Coherent Flame Model with 3 zones model (ECFM3Z).

5.2.2 SAGE Detailed Chemical Kinetics Solver

The *SAGE* combustion model is based on a set of elementary reactions: the chemical reaction mechanism. Thanks to this mechanism in fact, *SAGE* computes the reactions rate of each elementary reaction and so it allows to modelling the combustion of different fuels.

In addition to the mechanism, others files are needed to run a *SAGE* simulation:

- the already cited reaction mechanism file, called `mech.dat`;
- A species-specific thermodynamic properties file, called `therm.dat`;
- The `gas.dat` file, which contains the molecular transport properties or the `transport.dat` file for mixture-averaged diffusion

The constant rate k for the SAGE model follows the Arrhenius form:

$$k^+ = AT^b \exp\left(\frac{E_a}{RT}\right) \quad (5.12)$$

where, A is the pre-exponential factor, b is the temperature exponent, E_a is the activation energy and R is the universal gas constant. Defining the equilibrium coefficient k_{cr} as:

$$k_{cr} = k_{pr} \left(\frac{P_{atm}}{RT}\right)^{\sum_{m=1}^M \nu_{mr}} \quad (5.13)$$

the reverse constant rate can be expressed as:

$$k^- = \frac{k^+}{k_{cr}} \quad (5.14)$$

Thus, k_{pr} in eq.5.13 is obtained by:

$$k_{pr} = \exp\left(\frac{\Delta S_r^0}{R} - \frac{\Delta H_r^0}{RT}\right) \quad (5.15)$$

where ΔS and ΔH are the variation of entropy and enthalpy that occurs to pass from reactants to products; in particular:

$$\frac{\Delta S_r^0}{R} = \sum_{m=1}^M \nu_{mr} \frac{S_m^0}{R} \quad (5.16)$$

$$\frac{\Delta H_r^0}{RT} = \sum_{m=1}^M \nu_{mr} \frac{H_m^0}{RT} \quad (5.17)$$

It is now possible to solve the mass and energy conservation governing equations, indeed:

$$\frac{d[\chi_m]}{dt} = \dot{\omega}_m \quad (5.18)$$

$$\frac{dT}{dt} = \frac{V \frac{dP}{dt} - \sum_m (\bar{h}_m \dot{\omega}_m)}{\sum_m ([\chi_m] \bar{c}_{p,m})} \quad (5.19)$$

where V is the volume, P is the pressure, \bar{h}_m and $\bar{c}_{p,m}$ are the molar specific enthalpy and the molar constant-pressure specific heat respectively. The SAGE model solves all these equations in each computational time step and updates the species velocity coefficient by using the temperature obtained from eq. 5.19. Conversely, the temperature cells will be updated after the calculation of the species concentrations.

[6] [5]

5.3 Mechanisms used

As previously described, the SAGE combustion model is based on a set of elementary reactions called *Chemical reaction mechanisms*.

The operating point studied in this thesis work has been analysed by Lorenzo Testa. In its work, the best results have been obtained by using two mechanisms: the *GRI Mech 3.0* and the *USC mech II*. This thesis work is a further development of the previous projects; thus, these two mechanisms have been used again as first approach. However, since this time the study of the pollutant emissions has been carried out, these mechanisms have not proved to be suitable for the analysis; then a merging between *USC* and a third mechanism has been necessary: the *USCD NOx v2* reaction mechanism.

5.3.1 GRI Mech 3.0

The *GRI Mech 3.0*, composed by 325 chemical reactions, has been developed for NG engine at *University of California* at Berkeley, *Stanford University*, *The University of Texas* at Austin and *SRI International*. A part of the *mech.dat* file is shown in Figure 5.1.

5.3.2 USC mech II

The *USC mech II* mechanism contains more reactions than *GRI*, for that reason the simulation run time cost is higher: there are in fact 111 species and 784 elementary chemical reactions. However, since it does not include species and reactions between CO, CO₂ and NO_x, it is not suitable for the emission analysis. Thus, an extension of *USC*, the *USCD* mechanism, has been used.

```

! GRI-Mech Version 3.0 7/30/99  CHEMKIN-II format
! See README30 file at anonymous FTP site unix.sri.com,
directory gri;
! WorldWideWeb home page http://www.me.berkeley.edu/gri_mech/
or
! through http://www.gri.org , under 'Basic Research',
! for additional information, contacts, and disclaimer
ELEMENTS
O H C N AR
END
SPECIES
H2      H      O      O2      OH      H2O      HO2      H2O2
C       CH      CH2     CH2(S)  CH3     CH4      CO       CO2
HCO     CH2O     CH2OH   CH3O    CH3OH   C2H      C2H2     C2H3
C2H4    C2H5     C2H6    HCCO    CH2CO   HCCOH   N        NH
NH2     NH3      NNH     NO      NO2     N2O     HNO     CN
HCN     H2CN    HCNN    HCNO    HOCN   HNCO    NCO     N2
AR      C3H7    C3H8    CH2CHO  CH3CHO
END
!THERMO
! Insert GRI-Mech thermodynamics here or use in default file
!END
REACTIONS
2O+M<=>O2+M          1.200E+
17  -1.000          .00
H2/ 2.40/ H2O/15.40/ CH4/ 2.00/ CO/ 1.75/ CO2/ 3.60/ C2H6/
3.00/ AR/ .83/
O+H+M<=>OH+M          5.000E+
17  -1.000          .00
H2/2.00/ H2O/6.00/ CH4/2.00/ CO/1.50/ CO2/2.00/ C2H6/3.00/
AR/ .70/
O+H2<=>H+OH          3.870E+04    2.700
6260.00
O+HO2<=>OH+O2        2.000E+
13  .000          .00
O+H2O2<=>OH+HO2      9.630E+06    2.000
4000.00
O+CH<=>H+CO          5.700E+

```

Figure 5.1: *GRI Mech 3.0*; mech.dat file

5.3.3 USCD NO_x v2

This mechanism is an extension of the *USC mech II* and includes species and reactions not considered in the *USC*. The figure 5.2 shows the species included in *USC* and *USCD mech.dat* file. These two mechanisms have been merged in order to obtain a single set of reactions and to analyze the pollutant emissions in the exhaust gas of the model.

```

ELEMENTS
O H C N AR
END
SPECIES
!
AR N2
! HE
!
H O OH HO2 H2 H2O H2O2
O2
!
C CH CH2 CH2* CH3 CH4
HCO CH2O CH3O CH2OH CH3OH CO CO2
C2O
!
C2H C2H2 H2CC C2H3 C2H4 C2H5 C2H6
HCCO HCCOH CH2CO CH3CO CH2CHO CH2OCH
CH3CHO CH2OCH2
!
C3H3 pC3H4 aC3H4 cC3H4 aC3H5 CH3CCH2
CH3CHCH
C3H6 nC3H7 iC3H7 C3H8
CH2CHCO C2H3CHO CH3CHOCH2 CH3CH2CHO CH3COCH3
!
C4H2 nC4H3 iC4H3 C4H4 nC4H5 iC4H5
C4H5-2 c-C4H5
C4H6 C4H612 C4H6-2 C4H7 iC4H7 C4H81
C4H82 iC4H8
pC4H9 sC4H9 iC4H9 tC4H9 C4H10 iC4H10
!
H2C4O C4H4O CH2CHCHCHO CH3CHCHCO
C2H3CHOCH2
C4H6O23 CH3CHCHCHO C4H6O25
!
C5H4O C5H5O(1,3) C5H5O(2,4) C5H4OH C5H5OH C5H5
C5H6
1C5H7
!
C6H2 C6H3 1-C6H4 o-C6H4 C6H5 C6H6
!
C6H5CH2 C6H5CH3 C6H5C2H C6H5O C6H5OH C6H4O2
C6H5CO C6H5CHO C6H5CH2OH OC6H4CH3 HOC6H4CH3
C6H4CH3

```

(a)

```

ELEMENTS
N AR O H C
END
SPECIES
N2 AR O NO N
O2 OH H CH HCN
NCO CO NH H2 HNCO
HCCO NH2 CO2 H2O CN
HNO N2O N2H NH3 CH3
T-CH2 HO2 NO2
END
-----

```

(b)

Figure 5.2: (a) *USC mech II*; (b) *USCD NOx v2*

5.4 Emissions Modeling

CONVERGE allows to use two specific emission models: one for the soot modelling and one for the NO_x modelling. Since the engine studied in this thesis work is a port-fuel injection engine fuelled with NG, the soot formation is not an interesting topic. For that reason, only the NO_x modelling is briefly described.

NO_x Modeling

The method to calculate the NO_x emissions by CONVERGE is the extended Zel'dovich mechanism. It is based on the following set of reactions:



where a rate constant k is defined for each reactions and it is function of the temperature T :

$$k_{Ri,j} \propto \exp(1/T) \quad (5.23)$$

where i indicates the number of the reaction and j can be $f = forward\ reaction$ or $r = reverse\ reaction$.

Thus, it is possible to express the rate of formation of NO as:

$$\begin{aligned} \frac{d[NO]}{dt} = & k_{R1,f}[O][N_2] - k_{R1,r}[NO][N] + \\ & k_{R2,f}[N][O_2] - k_{R2,r}[NO][O] + \\ & k_{R3,f}[N][OH] - k_{R3,r}[NO][H] \end{aligned} \quad (5.24)$$

where $[NO]$ denotes the species concentration of NO in mol/cm^3 . After several steps and assuming the steady state approximation for the concentration of N, O, O₂, OH, H and N₂, the equation 5.24 can be written as:

$$\frac{d[NO]}{dt} = \frac{2R_1 \left[1 - ([NO]/[NO]_e)^2 \right]}{1 + ([NO]/[NO]_e) R'} \quad (5.25)$$

where:

$$R_1 = k_{R1,r}[NO]_e[N]_e \quad (5.26)$$

$$R_2 = k_{R2,f}[N]_e[O_2]_e \quad (5.27)$$

$$R_3 = k_{R3,f}[N]_e[OH]_e \quad (5.28)$$

$$R' = \frac{R_1}{R_2 + R_3} \quad (5.29)$$

Then, in order to convert the NO to NO_x, CONVERGE assumes that the measured NO is converted in NO₂ mass by a factor of 1,533.

A fundamental parameter which affect the NO_x of the model is the Schmidt Number, which is set in the `inputs.in` file. Typically, larger values of the Schmidt Number reduce the NO_x; conversely, smaller values tend to increase it without making important differences to the global combustion characteristics.

[6]

6 Results

6.1 Introduction

In this chapter the comparison between the simulation results, carried out in CONVERGE, and the experimental data will be shown; the discussion is split in two main cases, one for each fuel composition.

The aim of this comparison is to define the best model setup which can predict approximately the real engine in specific conditions. In particular, as already cited before, the model validation is focused on the following parameters:

Pressure in cylinder 1: the pressure of the *simulation closest cycle* is compared with the pressure of the *experimental closest cycle*; in addition, the *experimental maximum* and *minimum cycle* define the validity range where the simulation has to be considered valid;

Heat release in cylinder 1: the *HRR* of the simulation, calculated with an Octave script, will be compared with the *experimental closest cycle*. In addition, for the calculation of the heat release also the trapped mass will be taken into account;

Integrated heat release in cylinder 1: the *IHR* will be evaluated with the same method explained for *HRR*;

Pollutant emissions produced in cylinder 1: the CO, CO₂, NO_x and HC emissions will be compared with the experimental concentration (as ppm) in the exhaust region.

6.2 O.P. 2000[rpm] x 3.6[bar] x lambda=1; HCNG 15

The operating point 2000[rpm] x 3.6 [bar] x lambda=1, with CNG fuel has been studied by Lorenzo Testa [4]: as we can note in his thesis work, the simulation has been carried out by using a *coarse* mesh setting and *GRI Mech 3.0* as mechanism, which represent the best compromise between accuracy of the results and simulation run time. For that reason, as first attempt, the base simulation ran for the study of the HCNG 15 fuel composition (in the same operating point) presents the same mesh settings and the same mechanism.

6.2.1 Base simulation: GRI Mech 3.0

The Figure 6.1 shows a comparison between the results of the pressure in cylinder 1 obtained with the simulation *SAGE-GRI Mech 3.0* and the experimental data. The image is focused on the range between 640-840 crank angle degree.

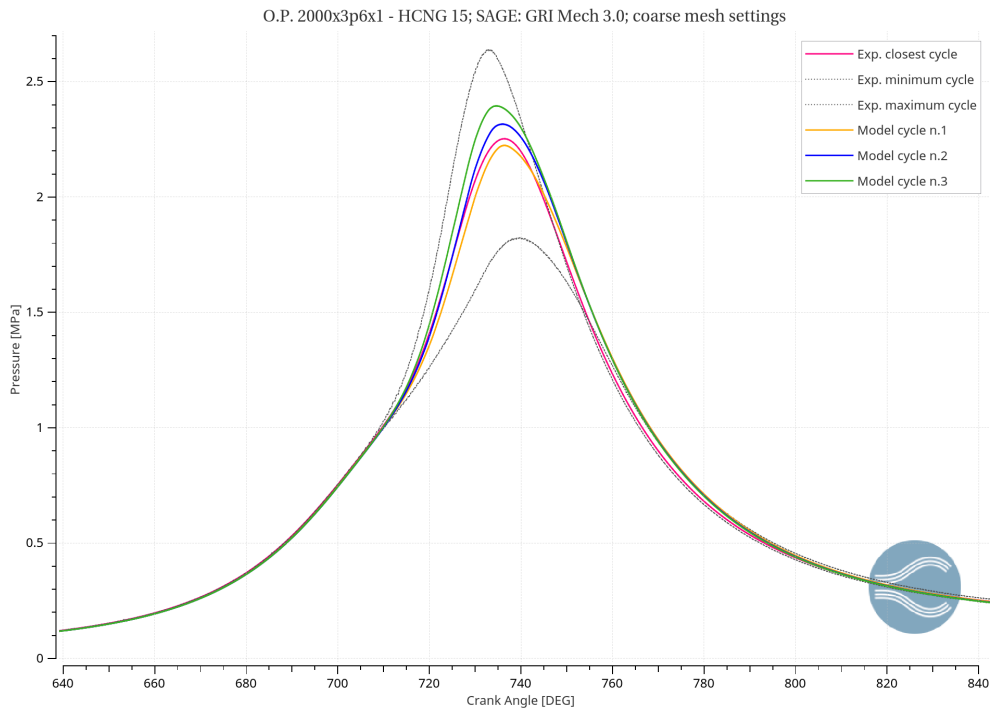


Figure 6.1: Pressure in cylinder 1; *SAGE-GRI Mech 3.0* and experimental data; coarse mesh settings, HCNG 15

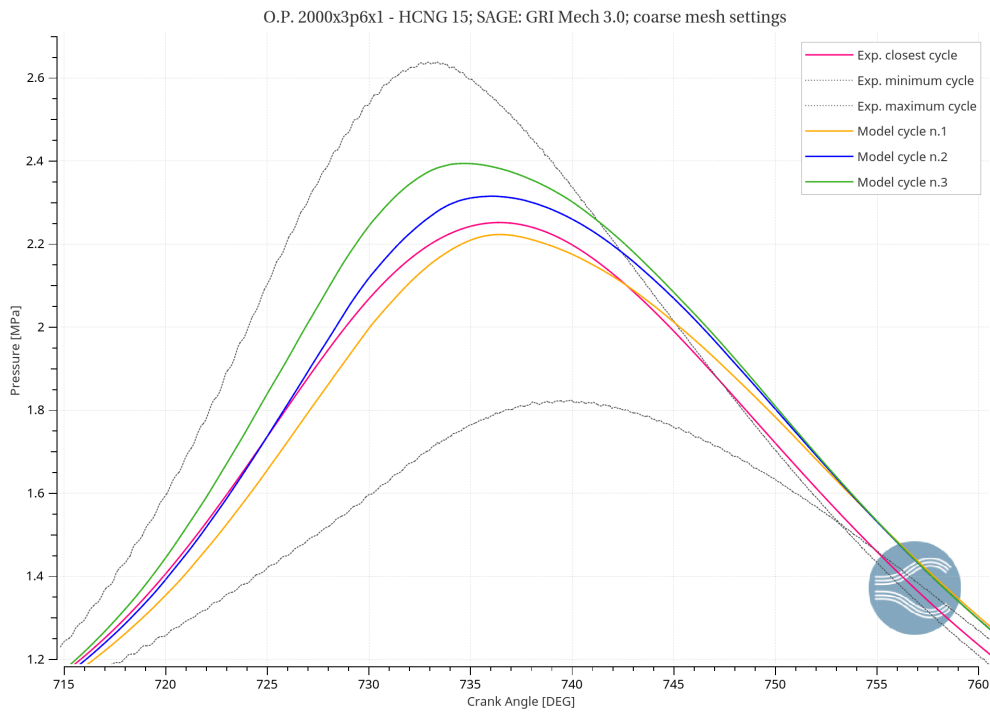


Figure 6.2: Pressure in cylinder 1 - Zoom; *SAGE-GRI Mech 3.0* and experimental data; coarse mesh settings, HCNG 15

The best cycle is the cycle number 1; however, this cycle is usually not taken into account for our analysis because is just useful for the initialization of the simulation. Thus, the best cycle is the cycle number 2 which presents a little overestimation of the peak pressure: 2,3 MPa against 2,25 MPa of the experimental closest cycle (Figure 6.2). The Figure 6.3 shows the compression phase (between 680-720 crank angle degree), which is acceptable:

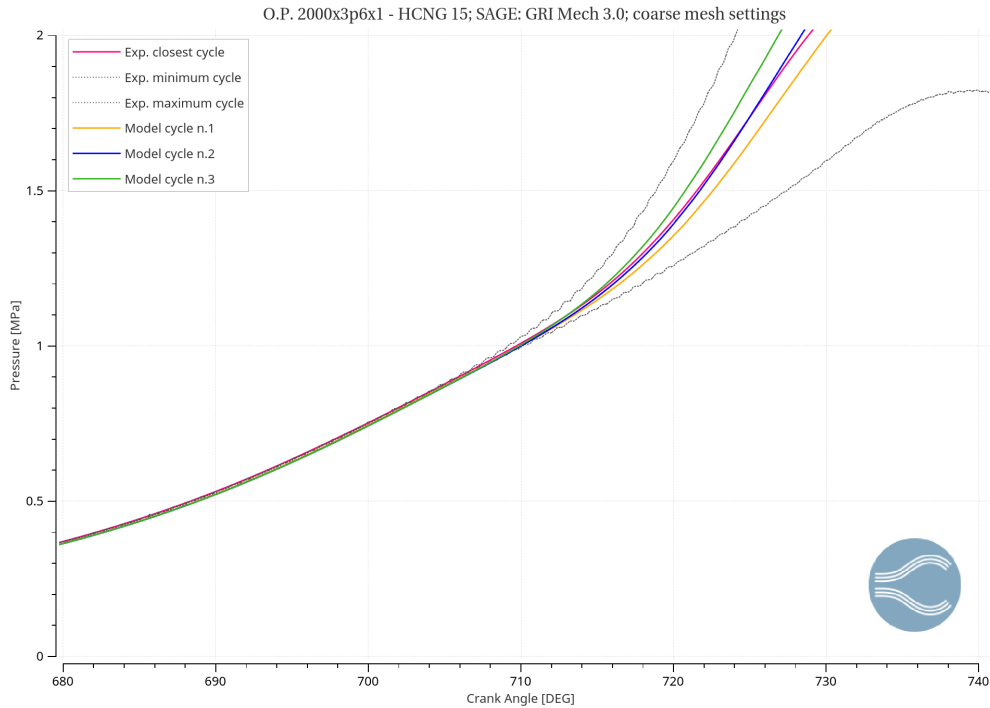


Figure 6.3: Pressure in cylinder 1 - Compression phase; *SAGE-GRI Mech 3.0* and experimental data; coarse mesh settings, HCNG 15

The Figures 6.4 and 6.5 show the *HRR* and the *AIHR* respectively. For this analysis, only the best model cycle will be considered and for this simulation it is the model cycle number 2:

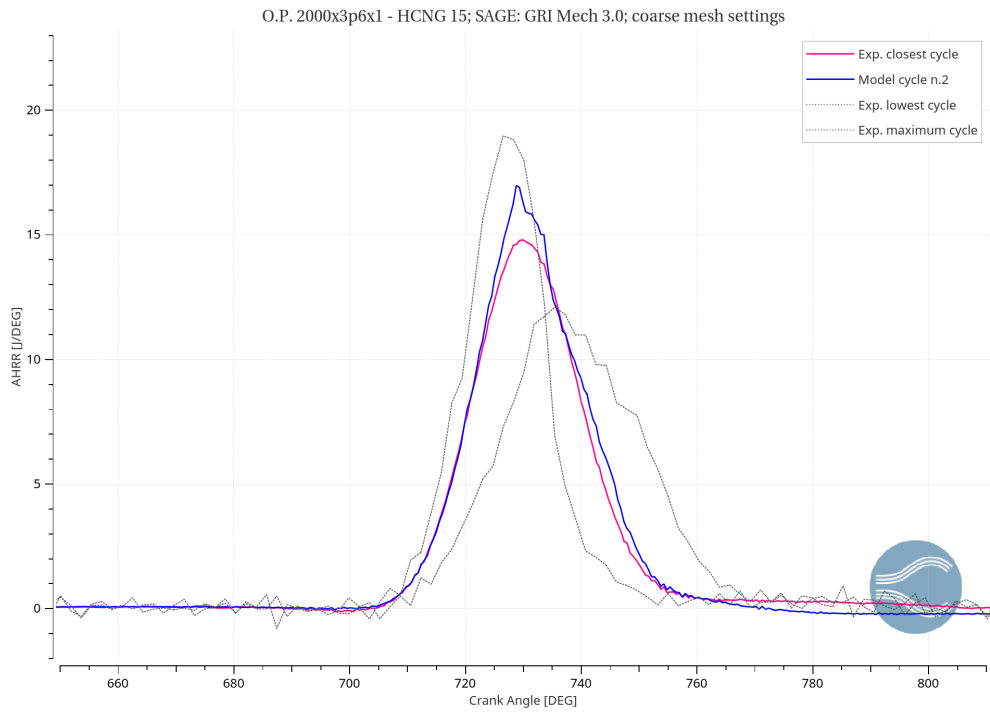


Figure 6.4: Heat release rate; *SAGE-GRI Mech 3.0* and experimental data; coarse mesh settings, HCNG 15

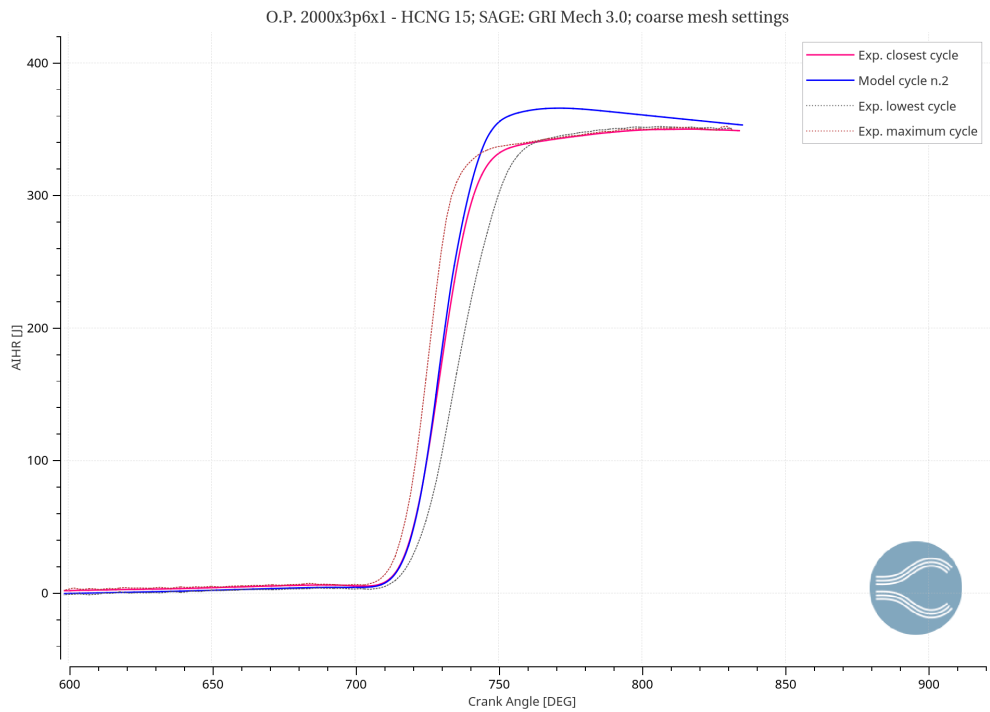


Figure 6.5: Integrated heat release rate; *SAGE-GRI Mech 3.0* and experimental data; coarse mesh settings, HCNG 15

From figure 6.4 it is possible to note that the model cycle follows very well the experimental profile, except around 730 CAD where there is a higher peak of energy of about 13%. Thus, also the *AIHR* will be different from the experimental data (as we can see in figure 6.5): the burn duration is longer and at around 750 CAD there is more energy released in comparison with the experimental cycle.

Concerning the trapped mass, the error obtained is around -0,84% which means that the model trapped mass inside the cylinder is 0,84% less than the measurements; thus, it is acceptable.

Finally, the analysis is now focused on the emissions. The Table 8 shows the comparison between the experimental measurements and the simulation results:

	Experimental value [ppm]	Simulation results [ppm]	Error
\tilde{x}_{CO}	5572	7590	+36,2%
\tilde{x}_{NO_x}	1880	1310	-30%
\tilde{x}_{CO_2}	103857	97933	-5,7%
\tilde{x}_{HC}	327	46,8	-83,7%

Table 8: Pollutant emissions results; *SAGE-GRI Mech 3.0* and experimental data; coarse mesh settings, HCNG 15

It is clear that the concentration of the species for the model is completely different from the experimental data, in particular for CO and HC; thus, several changes to the model case setup must be performed.

In the previous thesis work [5] it has been demonstrated that the mechanism which best simulates the behavior of the fuel with a percentage of hydrogen is the *USC mech II*. As it has been already shown, this mechanism gives an underestimation of the pressure (which is an improvement, since there are high pressure peaks for the base simulation); in addition, it will affect the *HRR* and *AIHR* as well as the emissions.

6.2.2 USC mech II

The following figures show the results obtained by using this new mechanism:

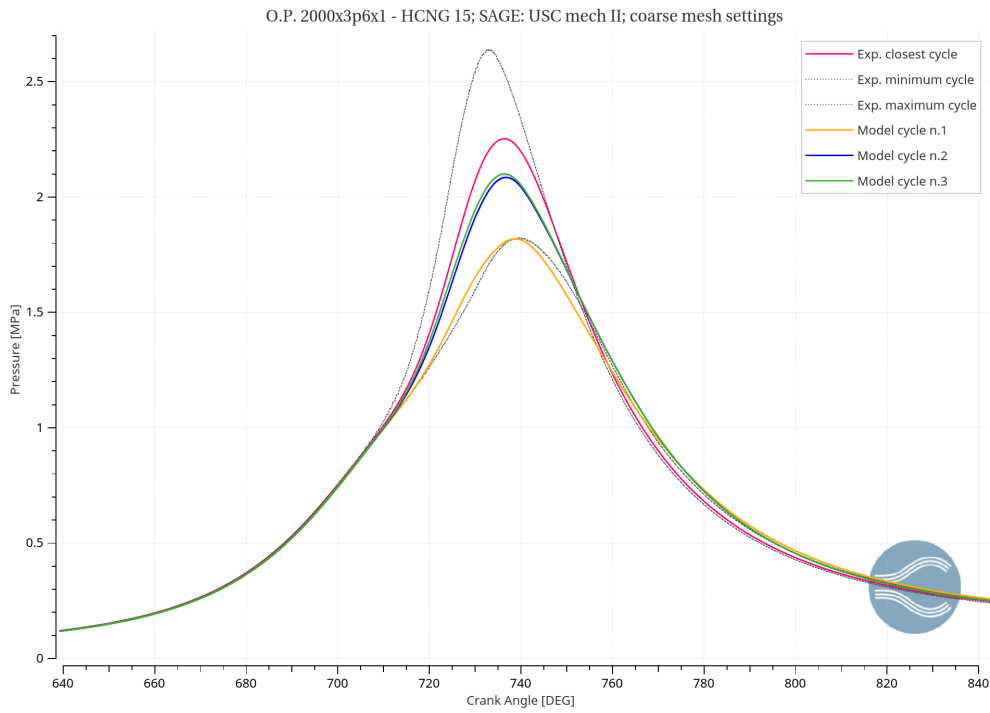


Figure 6.6: Pressure in cylinder 1; *SAGE-USC mech II* and experimental data; coarse mesh settings, HCNG 15

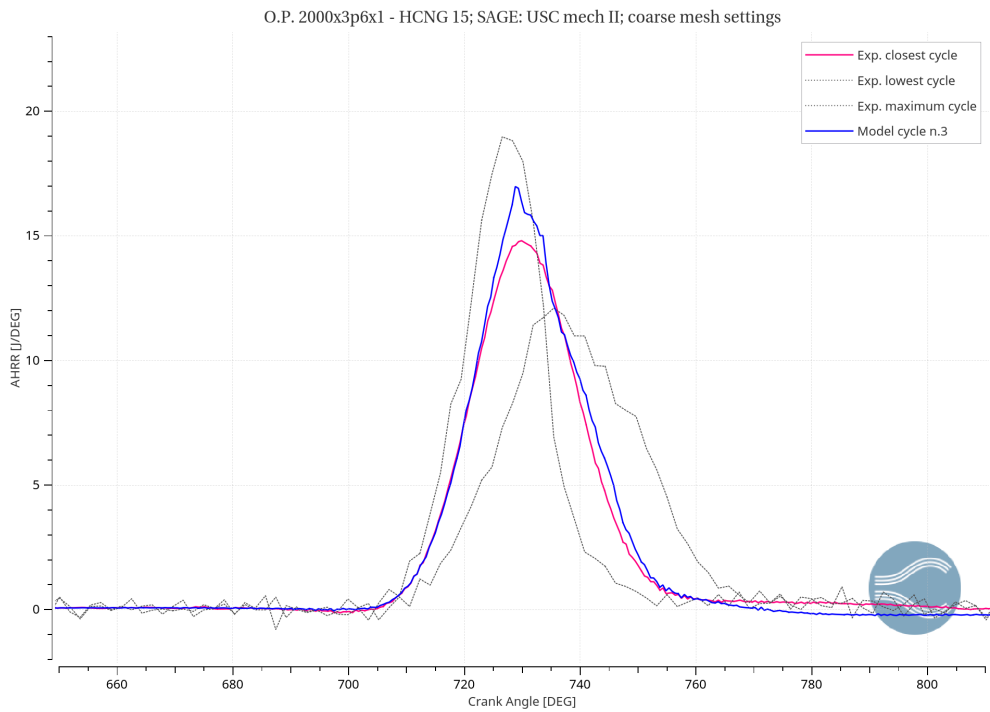


Figure 6.7: Heat release rate; *SAGE-USC mech II* and experimental data; coarse mesh settings, HCNG 15

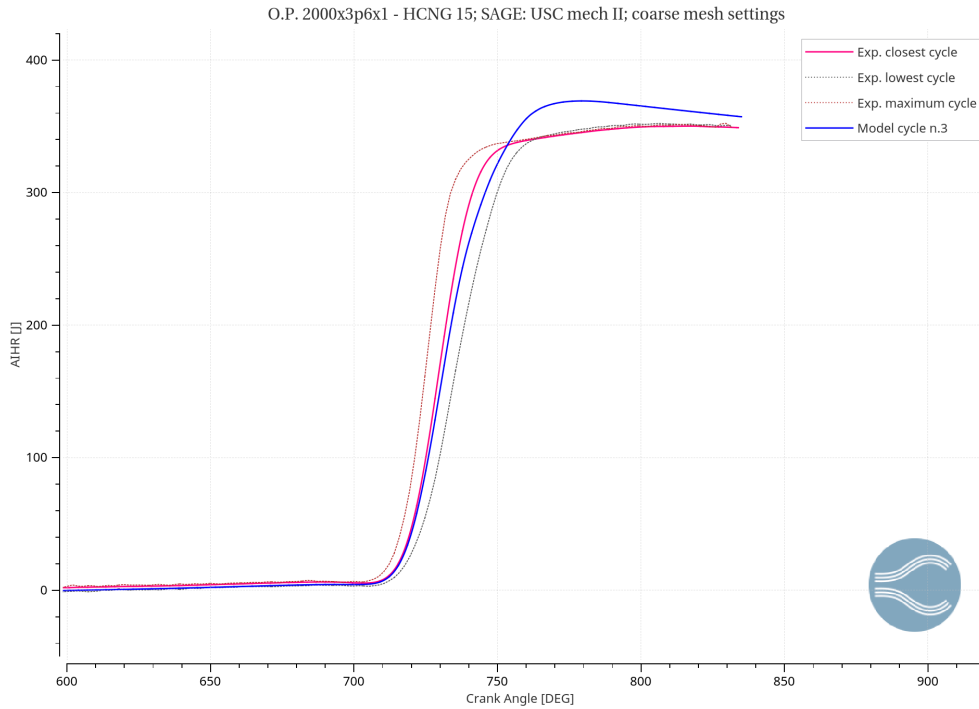


Figure 6.8: Integrated heat release rate; *SAGE-USC mech II* and experimental data; coarse mesh settings, HCNG 15

From Figure 6.6 it is possible to note that the model cycles have lower peaks of pressure of almost 7%: 2,1 MPa as maximum pressure value instead of 2,25 MPa of the experimental measure so the error is higher in comparison with the previous case (Figure 6.1).

In terms of heat release rate, there are not important differences with the base simulation: there is still an overestimation of energy at around 730 CAD (Figure 6.7) and of course we have a different slope of the curve for the integrated heat release (Figure 6.8) which means that the burn duration is longer than the experimental one.

The trapped mass is good also in this case, with an error of -1,33% which is acceptable.

Concerning the emissions, the Table 9 shows that the *USC mech II* fits better than the *GRI Mech 3.0* ; indeed, there is a great improvement for CO (from +36,2% to +18,6%) and NO_x (from -30% to +12,3%). However, the errors (in particular for the hydrocarbons) are still too high and not acceptables:

	Experimental value [ppm]	Simulation result [ppm]	Error
\tilde{x}_{CO}	5572	6608	+18,6%
\tilde{x}_{NO_x}	1880	2112	+12,3%
\tilde{x}_{CO_2}	103857	99101	-4,6%
\tilde{x}_{HC}	327	30,8	-90,6%

Table 9: Pollutant emissions results; *SAGE-USC mech II* and experimental data; coarse mesh settings, HCNG 15

As described in the previous chapters, unfortunately the *USC mech II* is not suitable for the emission analysis, in fact it does not include some species like NO and NO₂ and some reactions among NO_x, CO and CO₂. Therefore, for a better evaluation of the emissions, the *USCD NOx v2* extension is needed and the two mechanisms will be merged.

6.2.3 USC + USCD mechanisms merged

The three model cycles obtained by using the *USC mech II + USCD NOx v2* mechanisms merged are shown in the following figure:

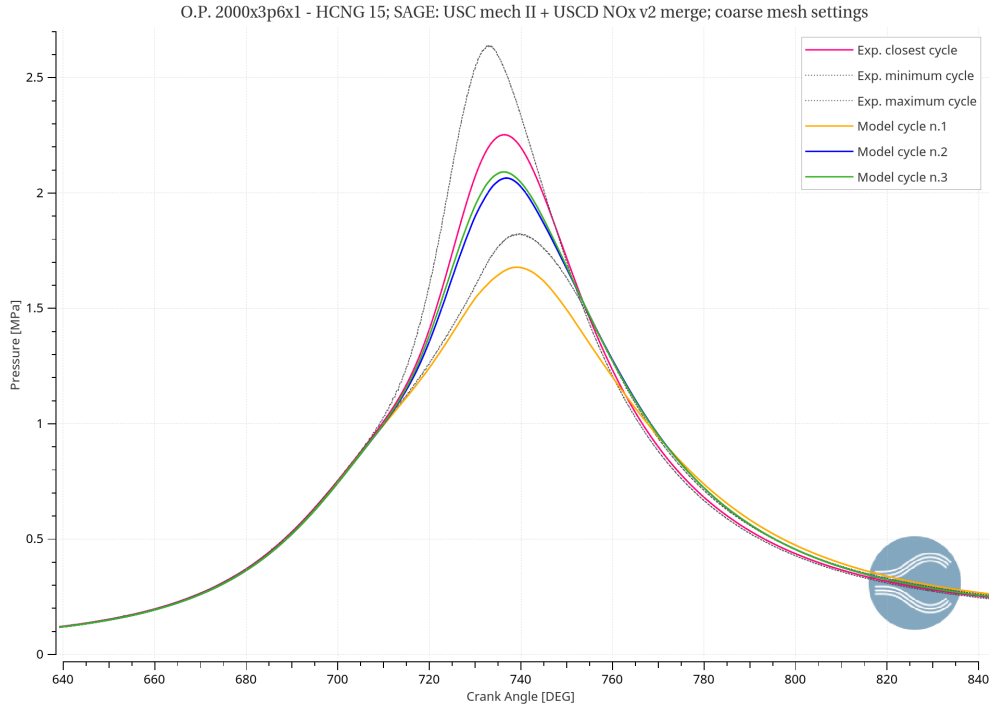


Figure 6.9: Pressure in cylinder 1; *SAGE - USC+USCD mechanisms merged* and experimental data; coarse mesh settings, HCNG 15

Once again, the first cycle is not considered. The second and the third cycle (which is the best cycle) are quite far from the experimental closest cycle with an error of almost 7% of the peak pressure; in addition, there is also a difference between the crank angle degrees where these peaks happen: 737 CAD for the experimental cycle and 735 CAD for the model cycles.

The compression phase is acceptable, while the expansion phase is slightly overestimated: this higher value of the pressure affects the *HRR* profile (and obviously the *AIHR* curve). The *heat release rate* and the *integrated heat release* are shown in Figure 6.10 and 6.11 :

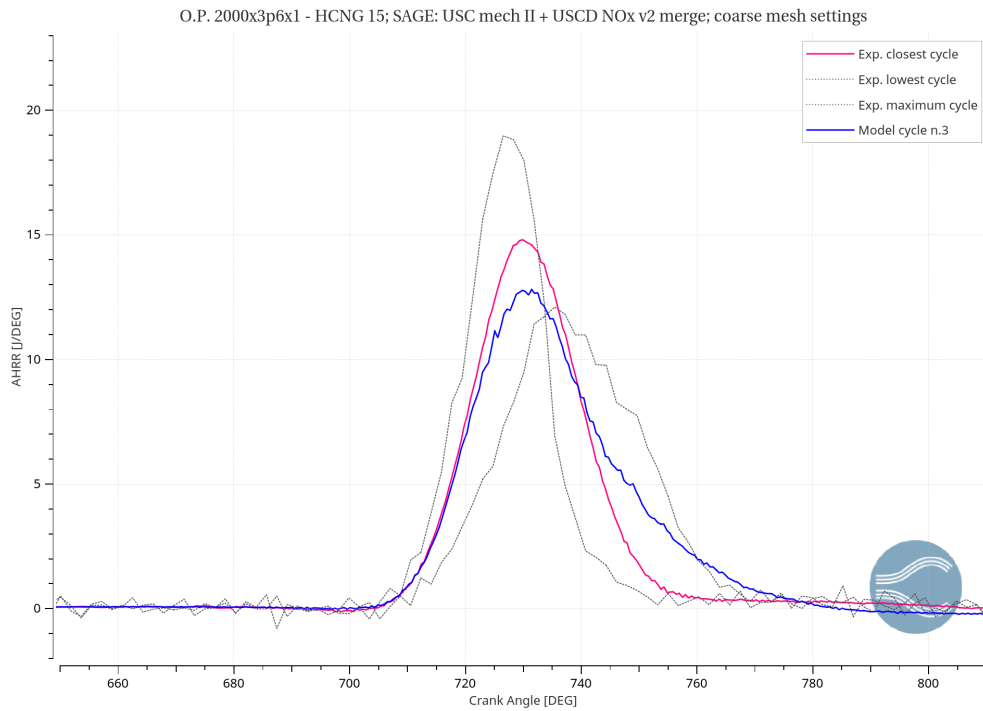


Figure 6.10: Heat release rate; *SAGE - USC+USCD mechanisms merged* and experimental data; coarse mesh settings, HCNG 15

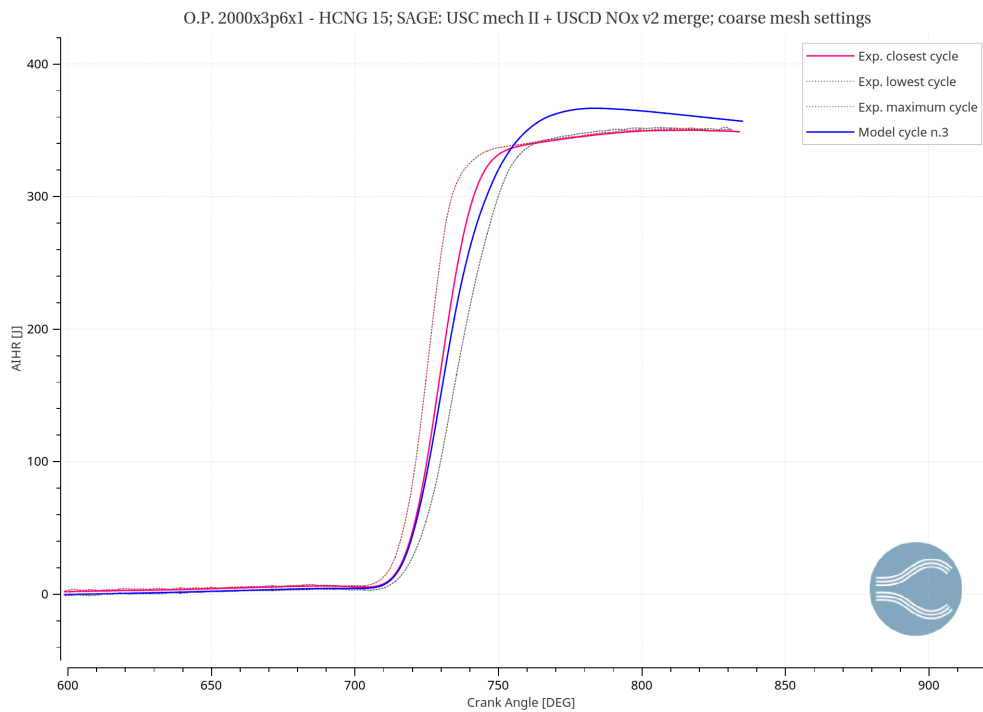


Figure 6.11: Integrated heat release; *SAGE - USC+USCD mechanisms merged* and experimental data; coarse mesh settings, HCNG 15

As it can be noticed, there is a quite remarkable difference between experimental and model *HRR* and *AIHR*; in fact the model cycle reaches a lower pressure peak and so a lower value of energy, with $HRR = 12,5$ J/DEG against 15 J/DEG of the experimental cycle at 730 CAD. Furthermore, there is an important difference of the heat release profiles between 750 CAD and 780 CAD that demonstrate that the combustion of the simulation is slower than the real one. This gap is highlighted also by the different slope of the curve and by the peak of the *AIHR* profile in Figure 6.11.

The trapped mass is 2,6% less than the experimental value, which is an acceptable error.

It is interesting to compare the different results provided by the two mechanisms. The Figure 6.12, 6.13 and 6.14 show the comparison of the pressure profiles, *HRR* and *AIHR* respectively:

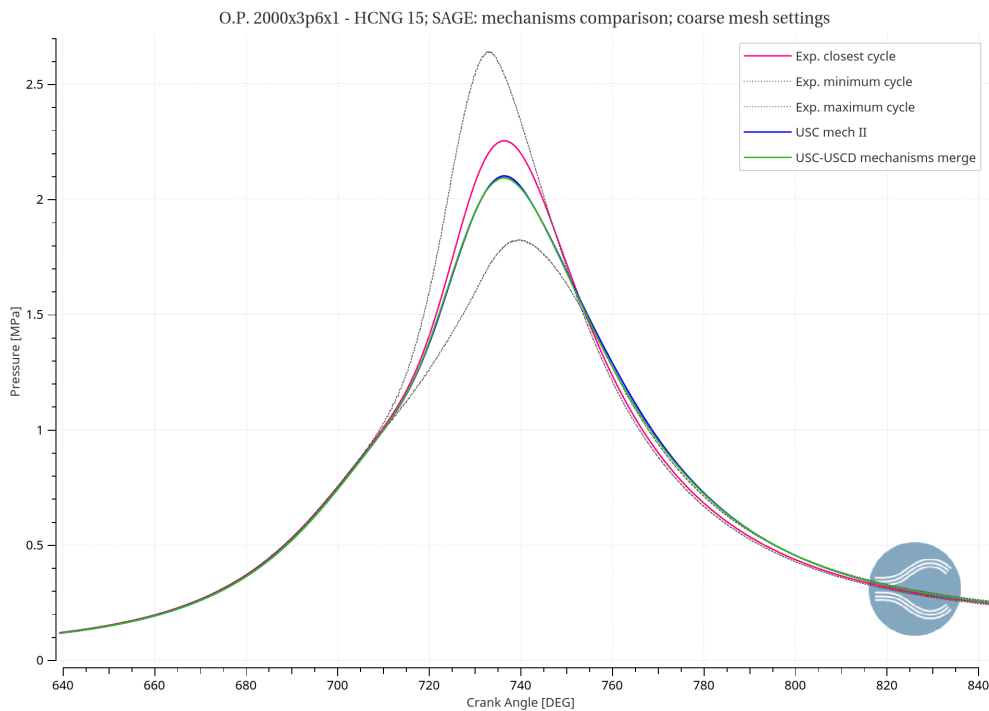


Figure 6.12: Pressure in cylinder 1; comparison between *USC mech II* and *USC+USCD mechanisms merged*; coarse mesh settings, HCNG 15

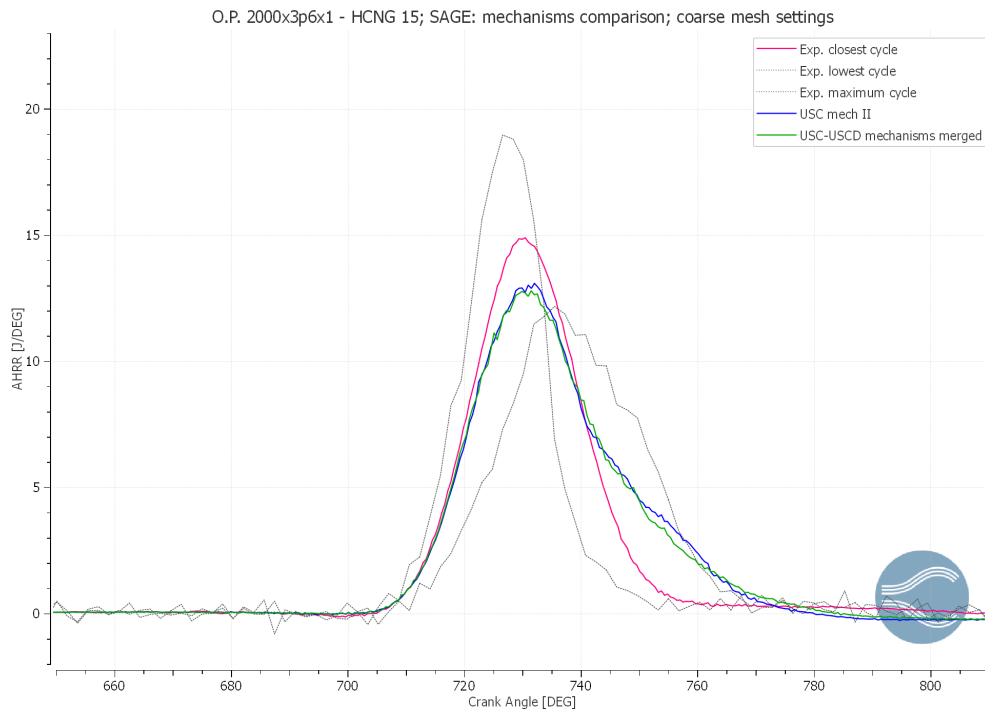


Figure 6.13: Heat release rate; comparison between *USC mech II* and *USC+USCD mechanisms merged*; coarse mesh settings, HCNG 15

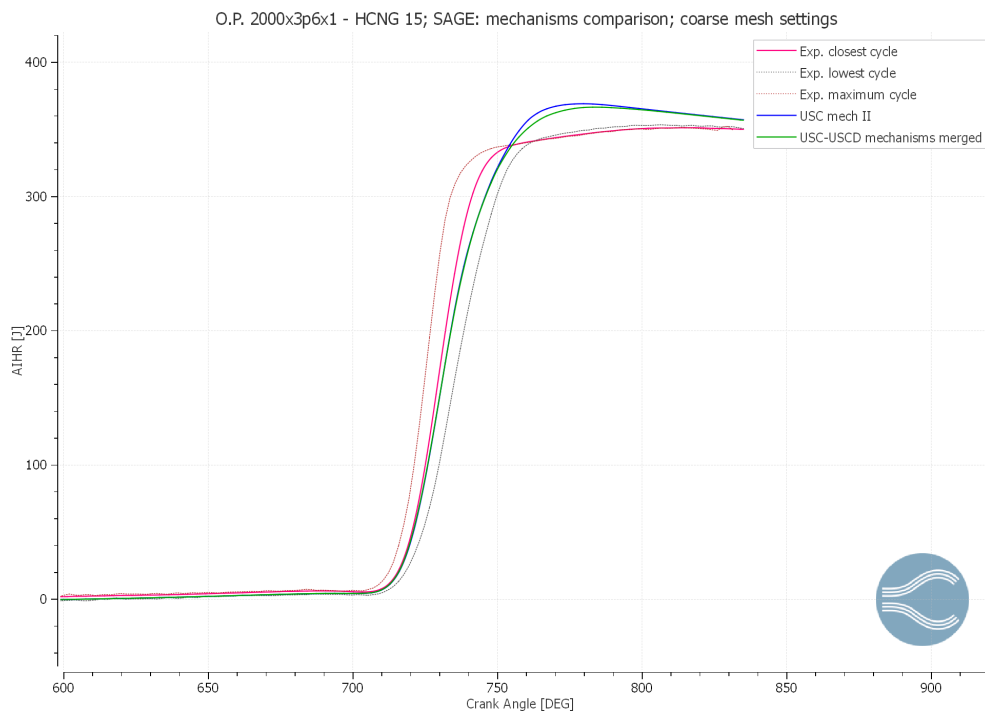


Figure 6.14: Integrated heat release rate; comparison between *USC mech II* and *USC+USCD mechanisms merged*; coarse mesh settings, HCNG 15

It is clear that there are not important improvements between the two mechanisms, which show the same errors and differences from the experimental data. However, in terms of pollutant emissions the values provided by *USC+USCD* mechanisms merged are different, as shown in the following table:

	Experimental value [ppm]	USC mech - Error	USC+USCD - Error
\tilde{x}_{CO}	5572	+18,6%	+24%
\tilde{x}_{NO_x}	1880	+12,3%	-7,6%
\tilde{x}_{CO_2}	103857	-4,6%	-5,8%
\tilde{x}_{HC}	327	-90,6%	-86%

Table 10: Pollutant emissions comparison: *USC mech II* and *USC+USCD mechanisms merged*; coarse mesh settings, HCNG 15

From Table 10 it is possible to note that there is a reduction of the error for NO_x and HC but unfortunately the error for CO and CO_2 increases. In particular, the hydrocarbons are still too few in comparison with the experimental data and the new mechanism used does not provide any improvements from this point of view. However, since there are more species and reactions involved in the simulation, *USC + USCD* mechanism is more accurate than *USC mech II* and *GRI Mech 3.0*; thus, further developments have been done starting from this latter model.

6.2.4 Schmidt Number sensitivity

A method to adjust the pressure peak location and magnitude is to change the Schmidt Number Sc . This number is a dimensionless numerical value which can increase or decrease the mass diffusivity; it is defined by the following relation:

$$D = \frac{\nu}{Sc} \quad (6.1)$$

where D is the mass diffusivity and ν is the kinematic viscosity [$\frac{m^2}{s}$].

As it is noticeable from eq.6.1, an increase of the Schmidt Number value causes a decrease of the diffusivity and it makes the combustion slower. For that reason, usually the effect of a higher value of Sc on the pressure is to decrease the peak magnitude. Conversely, a lower Schmidt Number causes a rise of the mass diffusivity which means a faster combustion and higher pressure peaks. As it will be shown in this chapter, the influence of Sc on the pressure will affect also the pollutant emissions, in particular the NO_x which are strictly related to the pressure (and temperature) inside the cylinder. For the previous simulations the preset value of Sc of 0,78 has been used. Since in the last results the pressure obtained from the simulations is lower than the experimental one, a Schmidt Number sensitivity has been performed reducing the Sc value; thus, two additional simulations have been ran with the following parameters:

	Base simulation	Case 2	Case 3
Sc	0,78	0,765	0,75

Case 2: Schmidt Number equal to 0,765

The figure 6.15 shows the pressure profiles obtained by using $Sc = 0,765$.

The best cycle is the model cycle number 2 where the error of the pressure peak magnitude is again almost 7% like the case with $Sc = 0,78$.

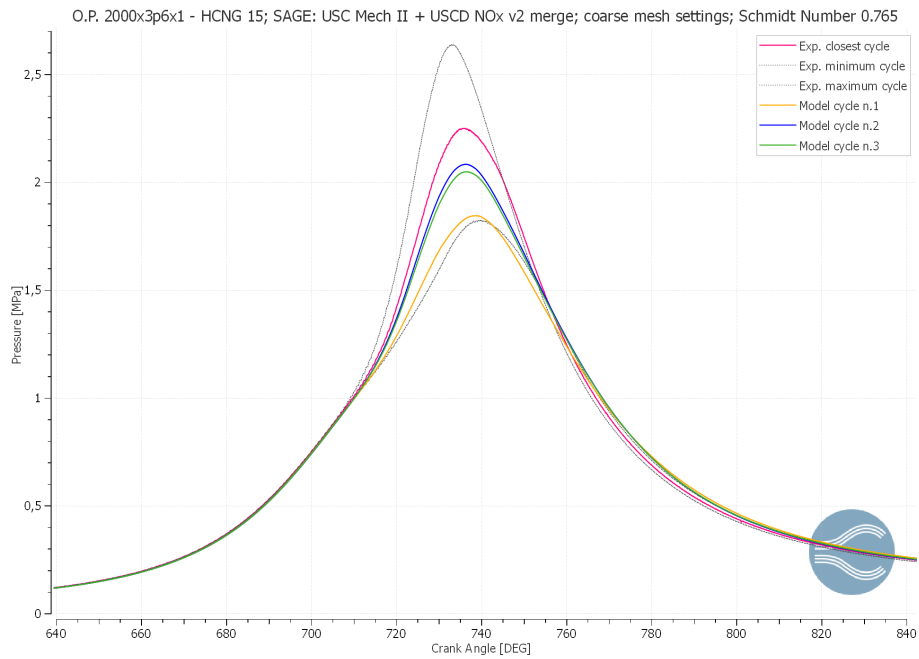


Figure 6.15: Pressure in cylinder 1; *SAGE: USC+USCD mechanisms merged*; Schmidt Number = 0,765; coarse mesh settings, HCNG 15

The *HRR* and *AIHR* of the model cycle number 2 are shown in figure 6.16 and 6.17.

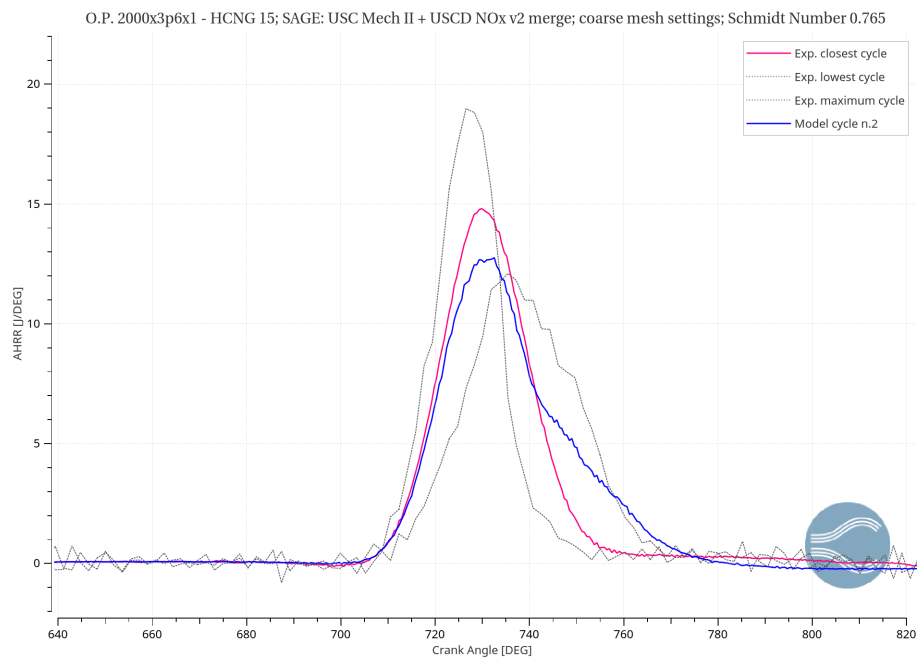


Figure 6.16: Heat release rate; *SAGE: USC+USCD mechanisms merged*; Schmidt Number = 0,765; coarse mesh settings, HCNG 15

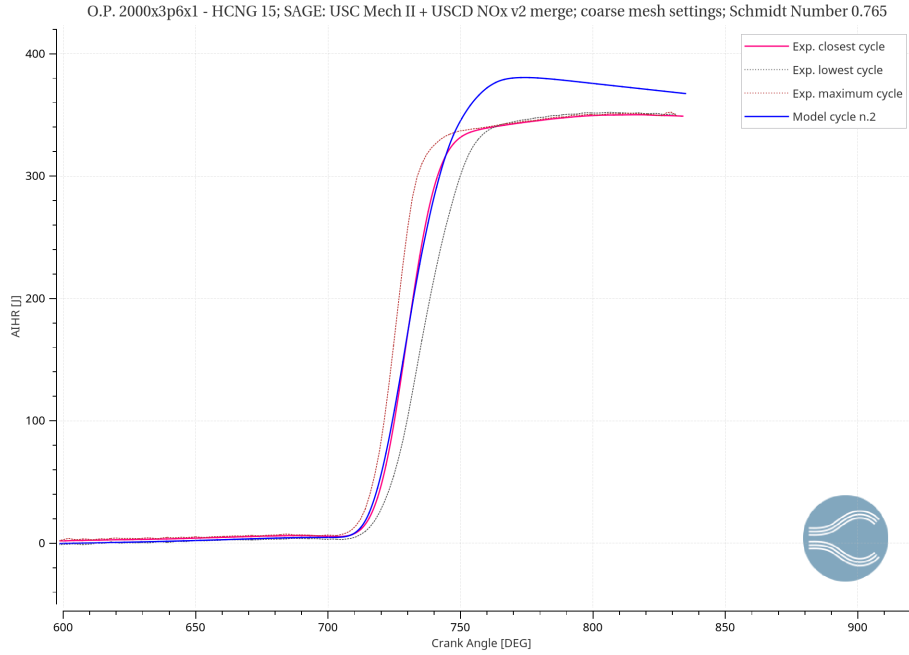


Figure 6.17: Integrated heat release; *SAGE: USC+USCD mechanisms merged*; Schmidt Number = 0,765; coarse mesh settings, HCNG 15

The reduction of Sc value to 0,765 is not enough in fact there are not improvements for the pressure peaks and neither for the heat release and the integrated heat release. In fact, the pressure is still lower than the experimental closest cycle; the HRR curve shows that the combustion is still slower than the real one, in particular during the expansion phase (between 740 CAD and 780 CAD). Finally, the $AIHR$ curve presents a higher peak of energy at 750 CAD.

Considering the emissions, it is interesting to note that since the diffusivity is higher also the NO_x concentration increases until the 3,7% of error. However, as shown in Table 11, the results for the others species are still far from the experimental measurements (in particular for CO and HC).

	Experimental value [ppm]	Simulation result [ppm]	Error
\tilde{x}_{CO}	5572	7619	+36,7%
\tilde{x}_{NO_x}	1880	1949	+3,7%
\tilde{x}_{CO_2}	103857	97811	-5,8%
\tilde{x}_{HC}	327	62,6	-80,9%

Table 11: Pollutant emissions results; *SAGE-USC+USCD merged*; Schmidt Number = 0,765; coarse mesh settings, HCNG 15

Case 3: Schmidt Number equal to 0,75

The following figures show the results of this specific case.

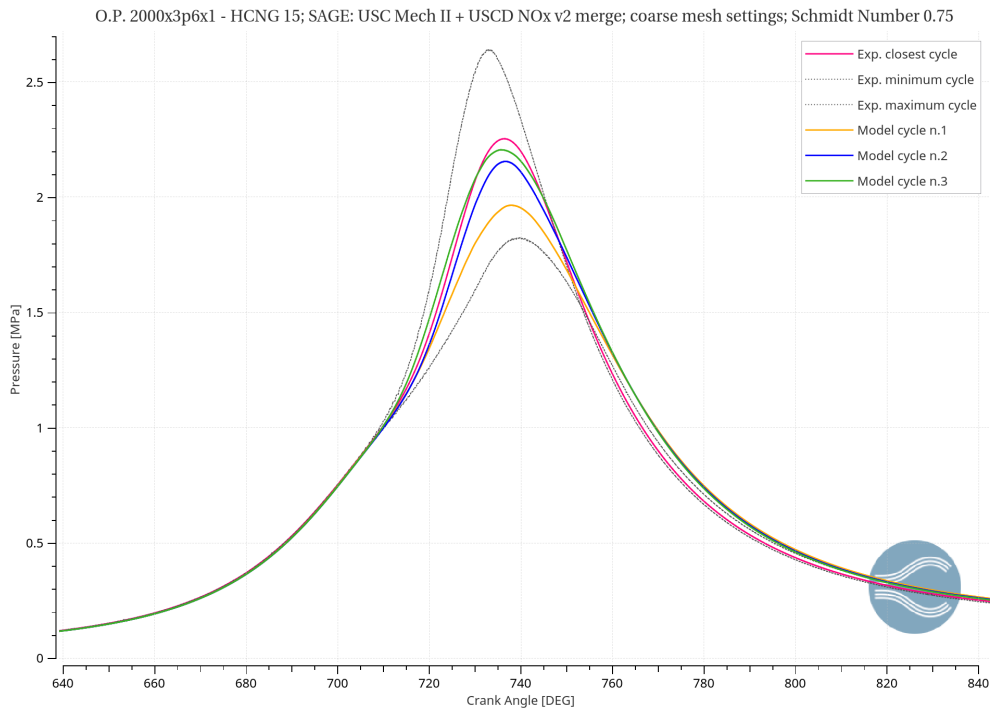


Figure 6.18: Pressure in cylinder 1; *SAGE: USC+USCD mechanisms merged*; Schmidt Number = 0,75; coarse mesh settings, HCNG 15

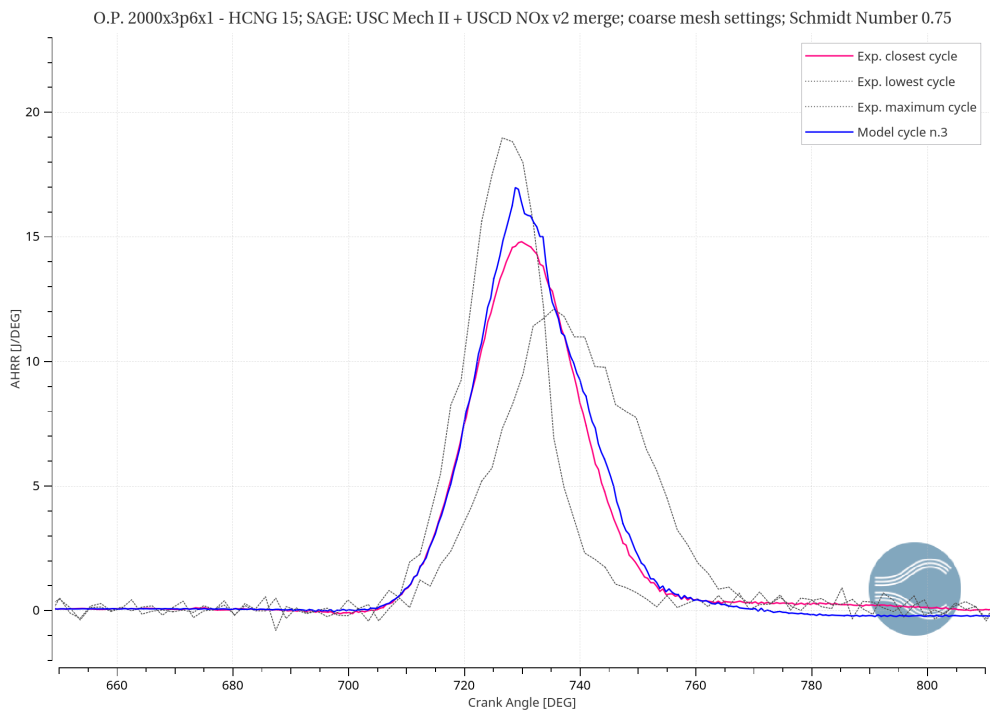


Figure 6.19: Heat release rate; *SAGE: USC+USCD mechanisms merged*; Schmidt Number = 0,75; coarse mesh settings, HCNG 15

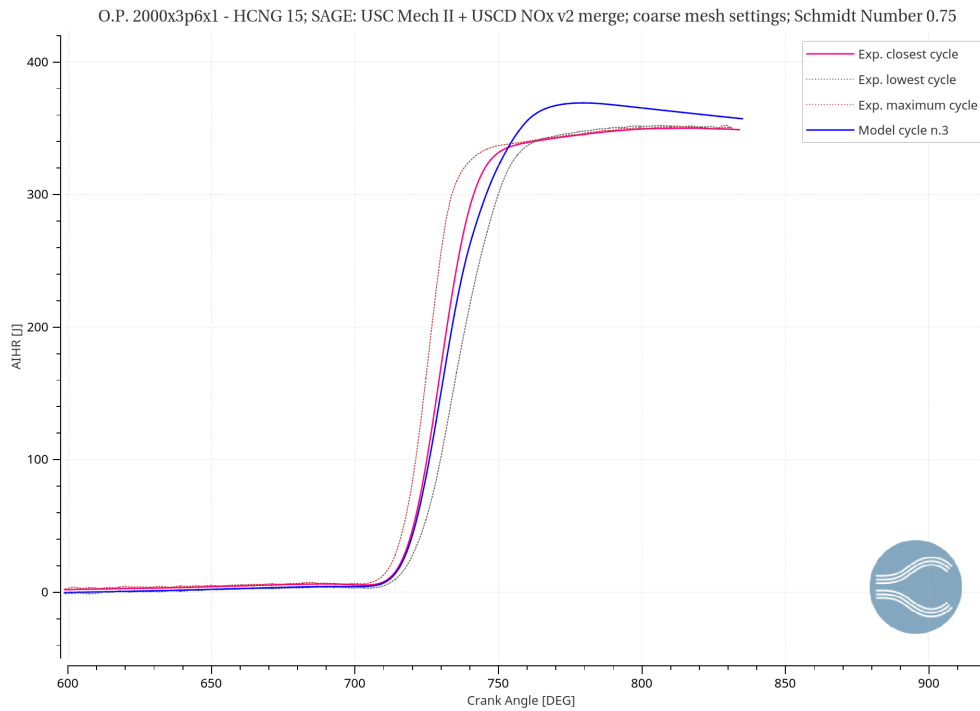


Figure 6.20: Heat release rate; *SAGE: USC+USCD mechanisms merged*; Schmidt Number = 0,75; coarse mesh settings, HCNG 15

From Figure 6.18 it is clear that there is an improvement for the pressure inside the cylinder 1: the CCV between the model cycle number 2 and the model cycle number 3 (which is the best cycle) is very small. Furthermore, the peak pressure of the cycle number 3 is 2,2 MPa, only 2,2% less than the peak of the experimental closest cycle. Finally, also the compression and expansion phase are acceptable because the model cycle is very close to the experimental one.

Another improvement is achieved for *HRR* and *AIHR*, as shown in figures 6.19 and 6.20: before and after the peak location of *HRR*, 730 CAD, the model cycle follows very well the experimental heat release rate profile. However, there is still a higher peak of energy which means that the *AIHR* of the model cycle reach higher values of energy in comparison with the experimental average.

The following table sums up the emission results obtained by setting this value as Sc :

	Experimental value [ppm]	Simulation result [ppm]	Error
\tilde{x}_{CO}	5572	5731	+2,9%
\tilde{x}_{NO_x}	1880	2013	+7%
\tilde{x}_{CO_2}	103857	96262	-7,3%
\tilde{x}_{HC}	327	62,3	-81%

Table 12: Pollutant emissions results; *SAGE-USC+USCD merged*; Schmidt Number = 0,75; coarse mesh settings, HCNG 15

Finally the error of the CO emissions has been reduced and it is less than 3%, which is acceptable, and for that reason the best value of Sc is 0,75. Furthermore, to better understand the effect of the reduction of Sc a comparison of the three cases is needed.

Comparison

The Figure 6.21 shows the different pressure profiles:

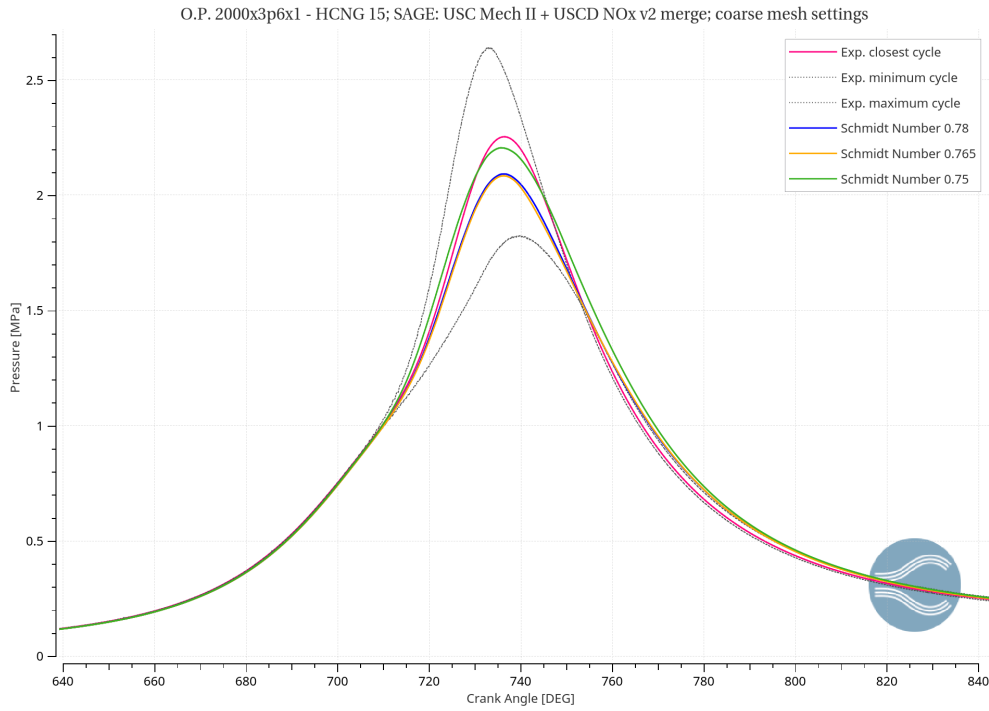


Figure 6.21: Pressure in cylinder 1; *SAGE: USC+USCD mechanisms merged*; Schmidt Number sensitivity; coarse mesh settings, HCNG 15

From this plot it is clear that there is no difference in terms of pressure for the cases with $Sc = 0,78$ and $0,765$. However, the value of $0,75$ is enough to increase the peak pressure until $2,2$ MPa at 736 CAD (as shown in Figure 6.22). Thus, the error on the peak pressure magnitude for $Sc=0,75$ is around 2% which is acceptable.

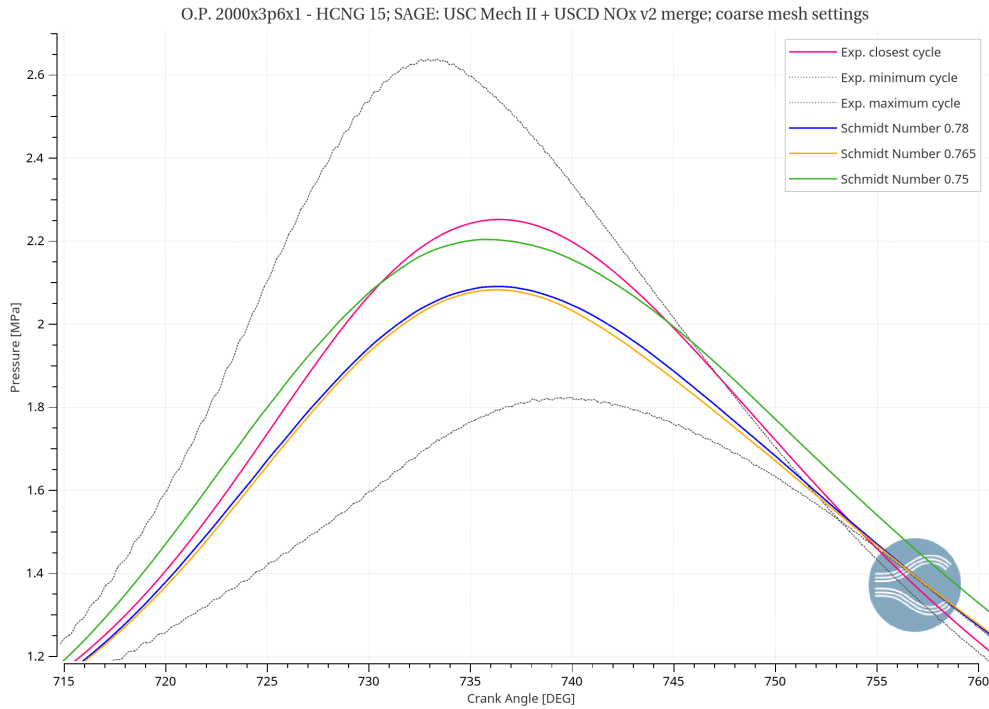


Figure 6.22: Pressure in cylinder 1 - zoom; *SAGE: USC+USCD mechanisms merged*; Schmidt Number sensitivity; coarse mesh settings, HCNG 15

Concerning the *HRR* and *AIHR*, the figures 6.23 and 6.24 show the improvements reached with the *Case 3* of the sensitivity. From Figure 6.23 in particular is easy to note how the model with the smallest value of Sc fits better to the case, especially during the compression and expansion phases where the model follows very well the experimental profile.

The trapped mass is acceptable in all three cases, as shown in the following table:

	$Sc=0,78$	$Sc=0,765$	$Sc=0,75$
Trapped mass error	-2,63%	-2,8%	-0,4%

Table 13: Trapped mass comparison; *SAGE-USC+USCD merged*; Schmidt Number sensitivity; coarse mesh settings, HCNG 15

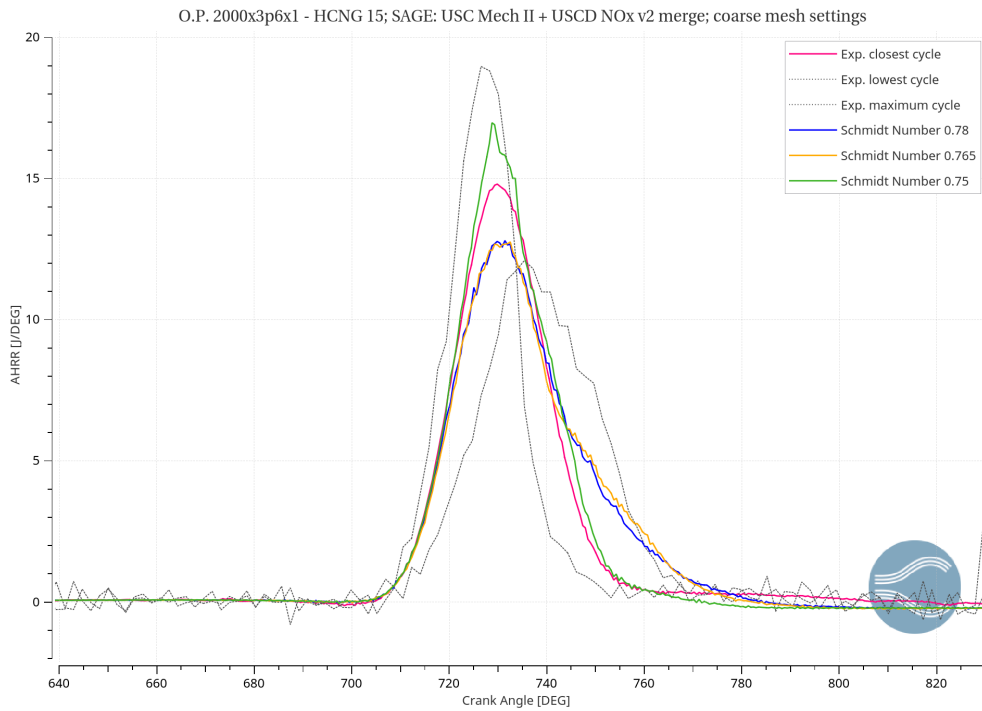


Figure 6.23: Heat release rate; *SAGE: USC+USCD mechanisms merged*; Schmidt Number sensitivity; coarse mesh settings, HCNG 15

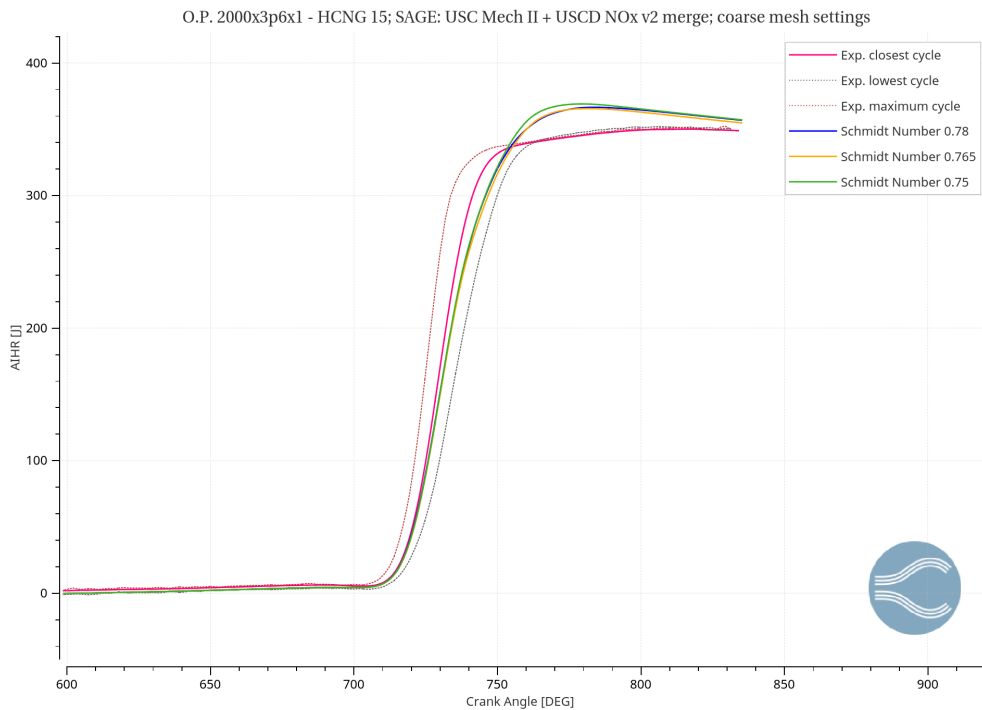


Figure 6.24: Heat release rate; *SAGE: USC+USCD mechanisms merged*; Schmidt Number sensitivity; coarse mesh settings, HCNG 15

Finally, from table 14 it is possible to understand how the pollutant emissions results change according to Sc :

	Experimental value	$Sc=0,78$	$Sc=0,765$	$Sc=0,75$
\tilde{x}_{CO} error	5572 ppm	6910 ppm +24%	7619 ppm +36,7%	5731 ppm +2,9%
\tilde{x}_{NO_x} error	1880 ppm	1737 ppm -7,6%	1949 ppm +3,7%	2913 ppm +7%
\tilde{x}_{CO_2} error	103857 ppm	97803 ppm -5,8%	97811 ppm -5,8%	96262 ppm -7,3%
\tilde{x}_{HC} error	327 ppm	46 ppm -86%	62,6 ppm -80,9%	62,2 ppm -81%

Table 14: Pollutant emissions results; *SAGE-USC+USCD merged*; Schmidt Number sensitivity; coarse mesh settings, HCNG 15

Although the error for NO_x , CO_2 and HC remains approximately constant, the best result is achieved for CO, where there is a strong reduction of the error from 24% and 36,7% to 2,9%. To understand why there is this difference and how the combustion process changes among the cases, an analysis of the burning process inside the cylinder might be interesting.

The Figure 6.25 shows the difference of the CH_4 mass fraction, which is the main component of the fuel. Using the smallest Schmidt Number we can see that there is less CH_4 into the combustion chamber which means that the combustion is faster and similar to the real process.

For that reason, even the formation of CO is different and the mass fraction is more close to the real one, as shown in the Figure 6.26 .

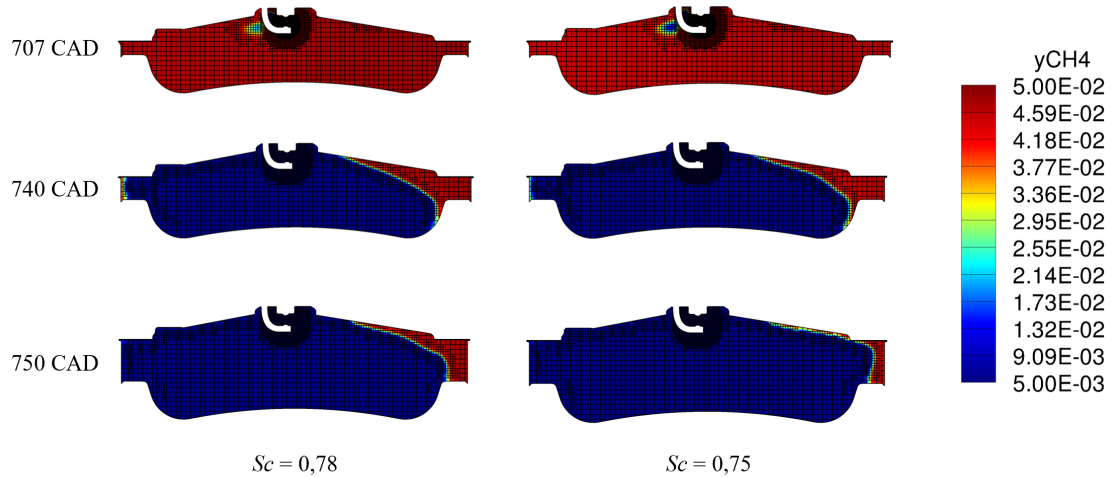


Figure 6.25: Comparison of mass fraction of CH_4 with two different values of Schmidt Number

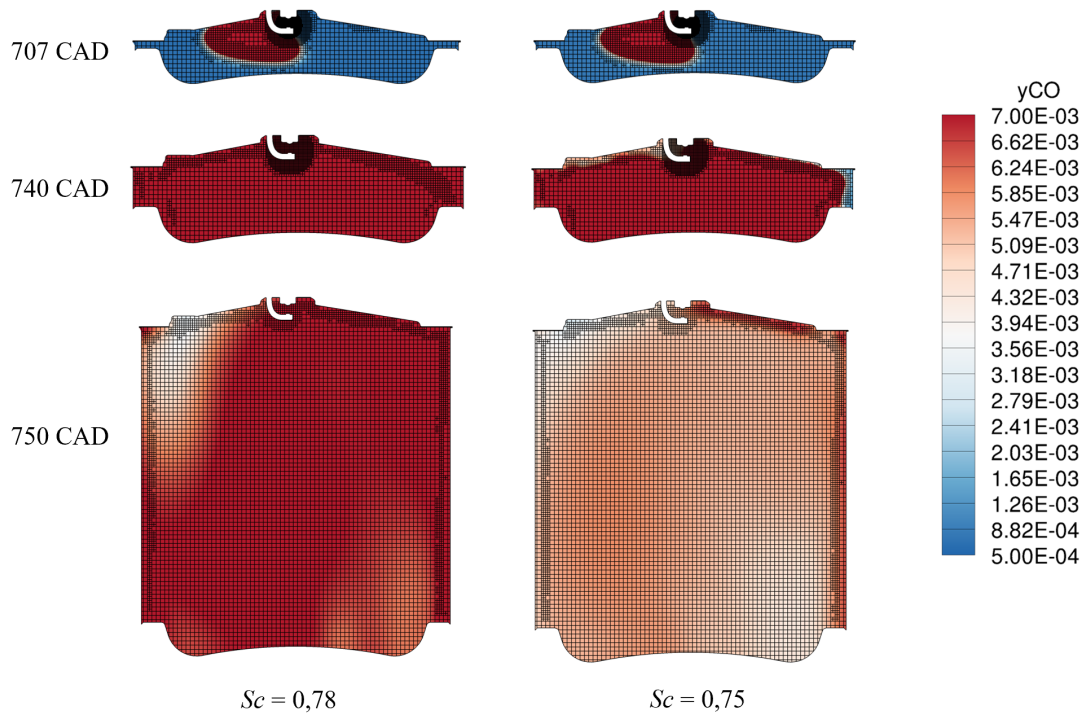


Figure 6.26: Comparison of mass fraction of CO with two different values of Schmidt Number

In conclusion, the Schmidt Number chosen is $Sc = 0,75$ because it allows to obtain very good results for pressure, heat release rate and integrated heat release, trapped mass and emissions. However, although the errors for CO, CO₂ and NO_x are acceptable, the unburned hydrocarbons are still too far from the experimental data. For that reason, three additional modifications have been made in order to increase the HC concentration: reduction of the temperature of the wall, LHV correction and modeling of the crevice volume.

6.2.5 Reduction of the temperature of the wall

A method to increase the formation of hydrocarbons during the combustion might be to reduce the temperature of the wall, which is a constant value set as boundary condition. In this way, the heat transfer with the wall is fostered and the temperature reached during the combustion decreases; thus, the combustion process gets worse and even less fuel burns causing a greater production of unburned hydrocarbons.

In order to understand the influence of the temperature of the wall, the preset value of $T = 427$ K has been reduced two times by 30 K and 50 K, so the others two values of the temperature are $T' = 397$ K and $T'' = 377$ K respectively.

Reduction of 30 K ($T = 397$ K)

The following figure shows the results obtained by using $T' = 397$ K:

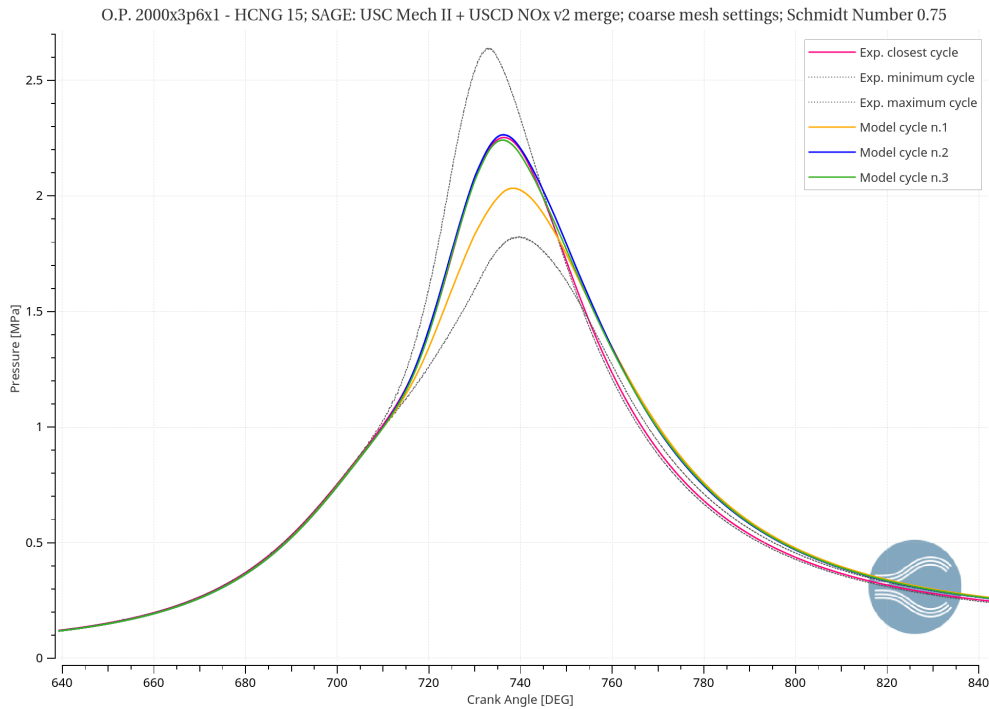


Figure 6.27: Pressure in cylinder 1; Temperature of the wall reduced by 30 K; *SAGE*: *USC+USCD mechanisms merged*; coarse mesh settings, HCNG 15

From the Figure 6.27 appears that the best cycles is the model cycle number 3, which presents a very small pressure peak error of 0,7%. The trapped mass is also good (almost -2%) and it is acceptable.

The *HRR* profile (shown in Figure 6.28) is different in comparison with the previous case, in fact the compression phase and the peak of energy follow the experimental curve; however, since the combustion is worse the burn duration is longer and the heat release rate is high between 740 CAD and 780 CAD. Obvi-

ously, the $AIHR$ is influenced by these effects and presents a high peak of energy as well (Figure 6.29).

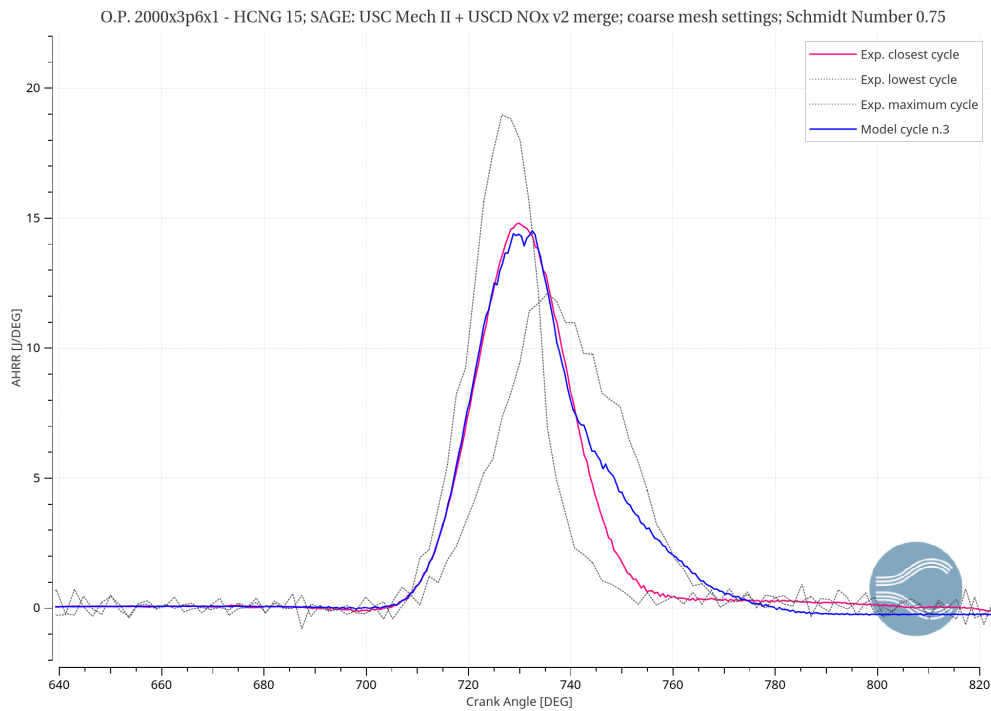


Figure 6.28: Heat release rate; Temperature of the wall reduced by 30 K; *SAGE*: *USC+USCD mechanisms merged*; coarse mesh settings, HCNG 15

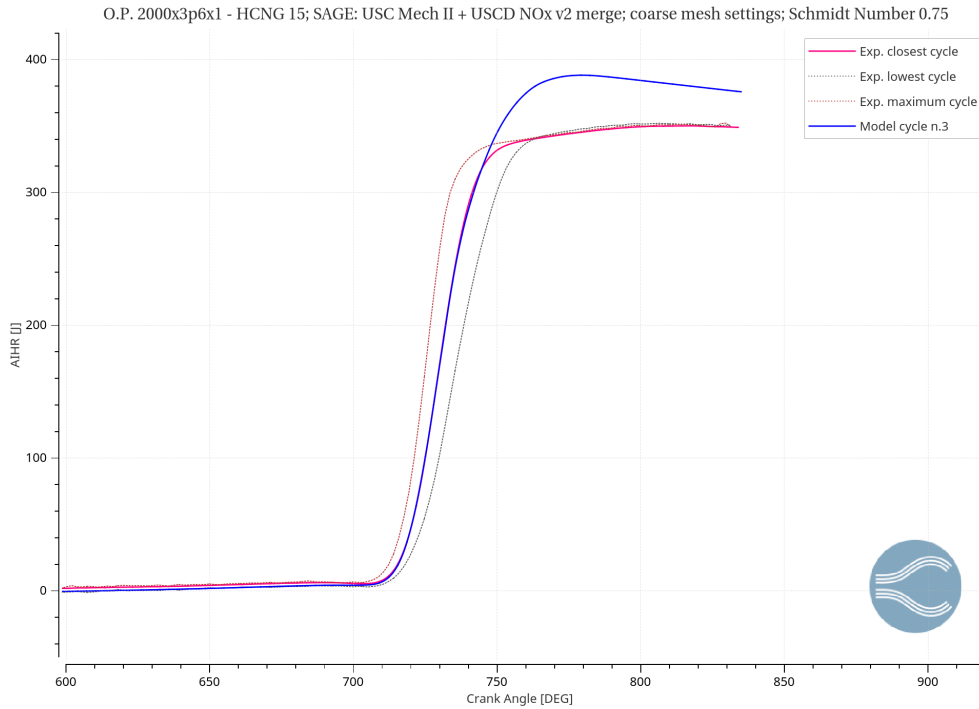


Figure 6.29: Integrated heat release; Temperature of the wall reduced by 30 K; *SAGE*: *USC+USCD mechanisms merged*; coarse mesh settings, HCNG 15

Finally, the following table sums up the emission results:

	Experimental value [ppm]	Simulation result [ppm]	Error
\tilde{x}_{CO}	5572	5731	+2,8%
\tilde{x}_{NO_x}	1880	1884	+0,2%
\tilde{x}_{CO_2}	103857	96187	-7,4%
\tilde{x}_{HC}	327	70,3	-78,5%

Table 15: Pollutant emissions results; Temperature of the wall = 397 K; *SAGE-USC+USCD merged*; Schmidt Number = 0,75; coarse mesh settings, HCNG 15

Although the unburned hydrocarbons increase, the error is still very high so the reduction of 30 K is not enough.

Reduction of 50 K (T = 377 K)

For this specific case the results of pressure, *HRR* and *AIHR* are shown in the following figures:

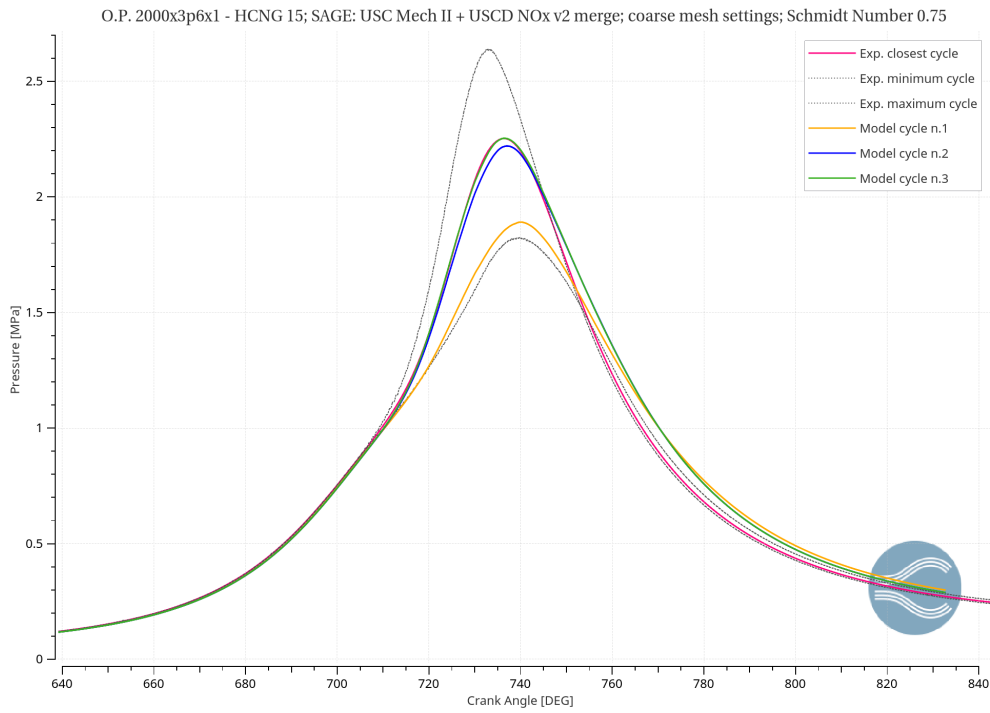


Figure 6.30: Pressure in cylinder 1; Temperature of the wall reduced by 50 K; *SAGE*: *USC+USCD mechanisms merged*; coarse mesh settings, HCNG 15

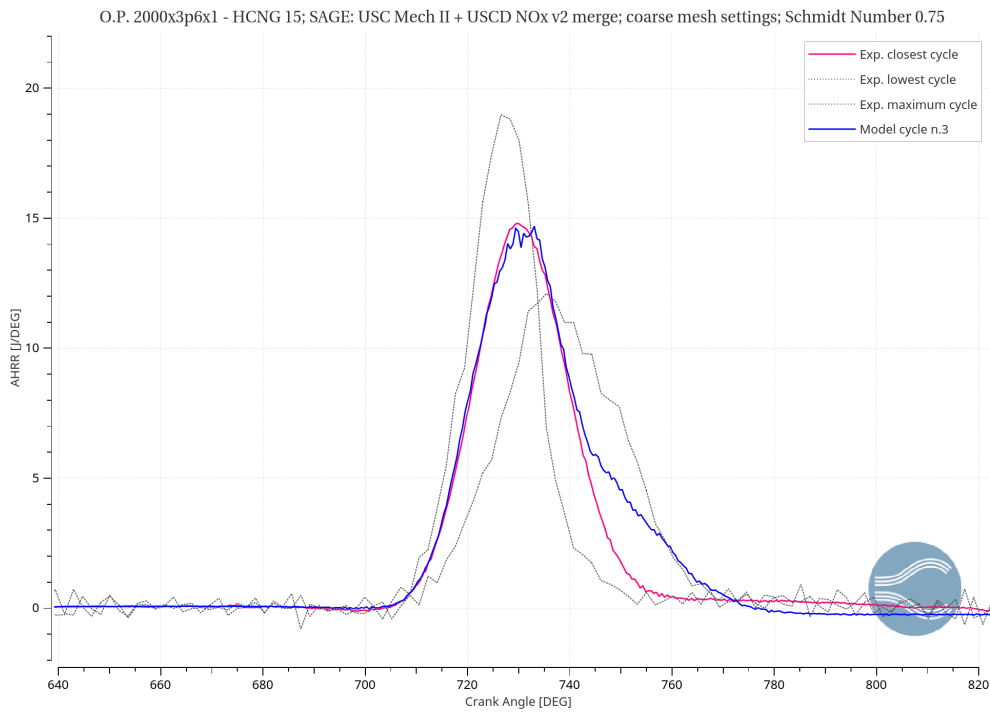


Figure 6.31: Heat release rate; Temperature of the wall reduced by 50 K; *SAGE*: *USC+USCD mechanisms merged*; coarse mesh settings, HCNG 15

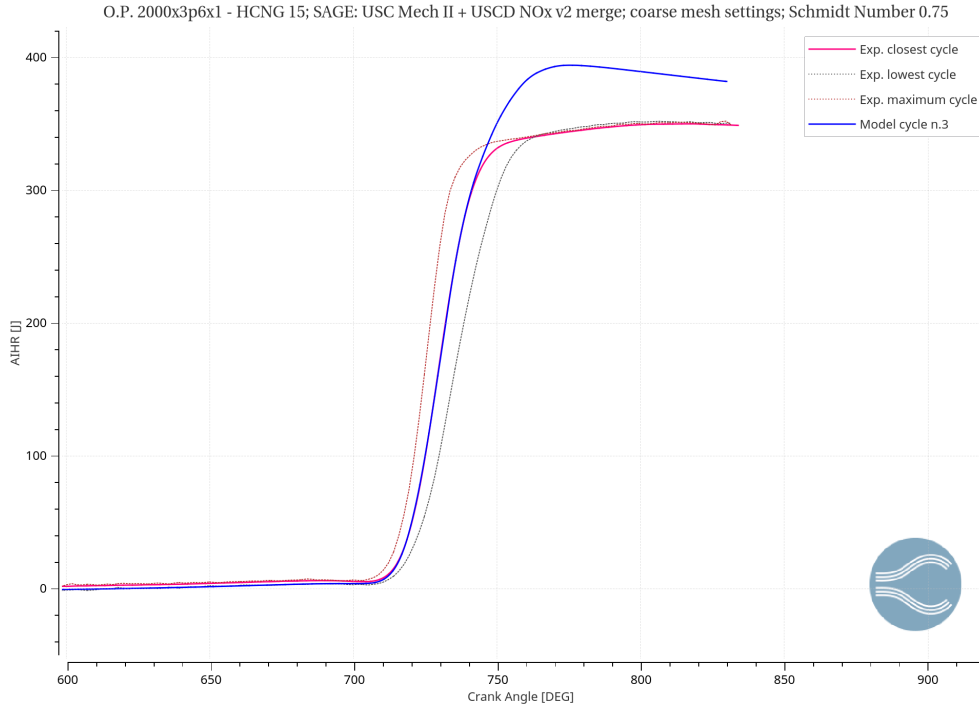


Figure 6.32: Integrated heat release; Temperature of the wall reduced by 50 K; *SAGE*: *USC+USCD mechanisms merged*; coarse mesh settings, HCNG 15

From Figure 6.30 it is clear that the best cycle is the model cycle number 3, which presents basically the same pressure profile of the experimental cycle (with a small error in the expansion phase); the error of the pressure peak is in fact almost -0,1%.

Comparing the results shown in the figures 6.31 and 6.32 with the previous case, it can be noted that the curves are very similar, with the same peak of energy and the same excess between 740 CAD and 780 CAD.

Finally, the Table 16 sums up the emission results. Unfortunately, neither in this case the rise of the HC is not enough and the error is still extremely high. In order to understand the influence of the reduction of the wall temperature, a comparison of the three cases might be useful.

	Experimental value [ppm]	Simulation result [ppm]	Error
\tilde{x}_{CO}	5572	5613	+0,7%
\tilde{x}_{NO_x}	1880	1624	-13,6%
\tilde{x}_{CO_2}	103857	96277	-7,3%
\tilde{x}_{HC}	327	75,6	-76,9%

Table 16: Pollutant emissions results; Temperature of the wall = 377 K; *SAGE-USC+USCD merged*; Schmidt Number = 0,75; coarse mesh settings, HCNG 15

Comparison

The comparison of the pressure obtained with $T = 427$ K, $T' = 397$ K and $T'' = 377$ K is shown in Figure 6.33: as we can see, although the three cycles are acceptable, the best results are achieved by using T' and T'' .

However, the HRR shown in figure 6.34 is different: although the peak of energy is lower for T' and T'' , the curves present a higher value of heat release between 740 CAD and 780 CAD; thus, the integrated heat release in figure 6.35, reaches higher values of energy in comparison with the experimental profile.

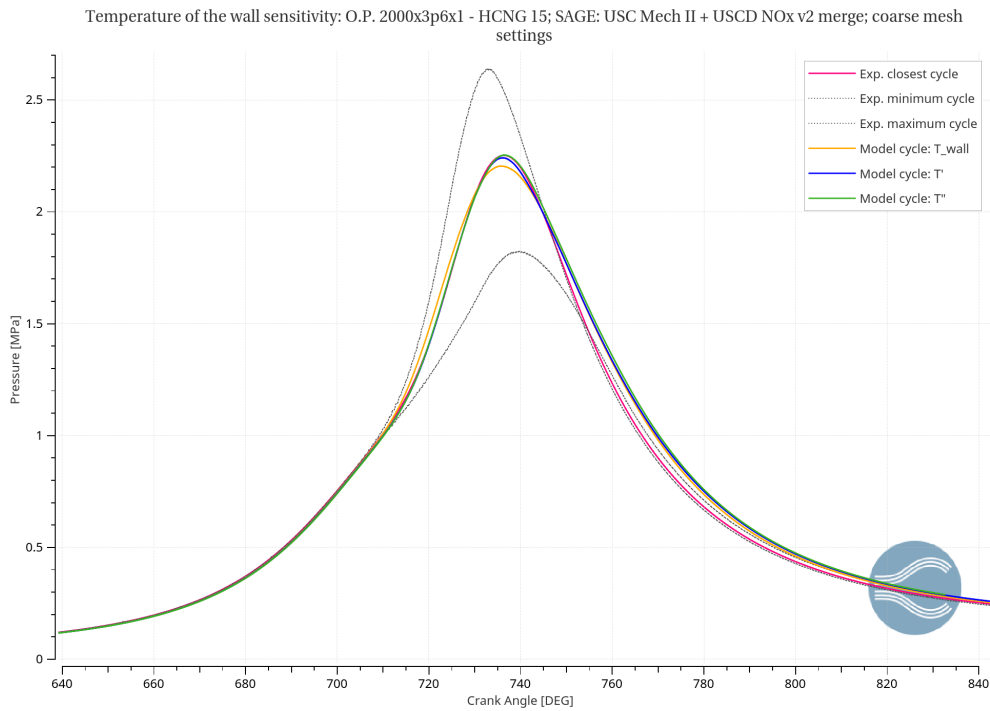


Figure 6.33: Pressure in cylinder 1; Temperature of the wall sensitivity; *SAGE*: *USC+USCD mechanisms merged*; coarse mesh settings, HCNG 15

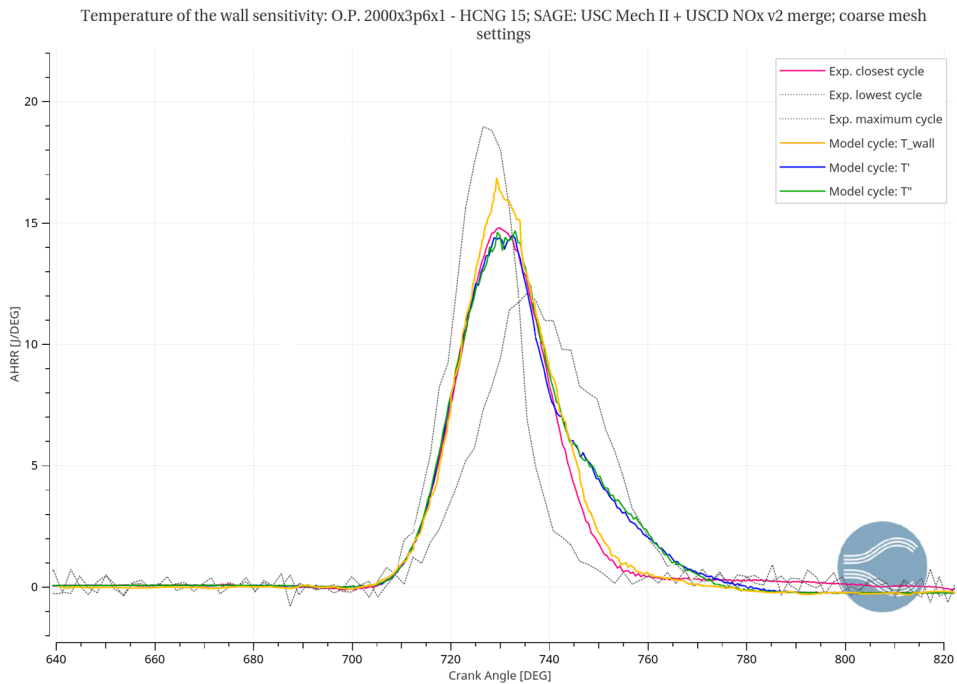


Figure 6.34: Heat release rate; Temperature of the wall sensitivity; *SAGE: USC+USCD mechanisms merged*; coarse mesh settings, HCNG 15

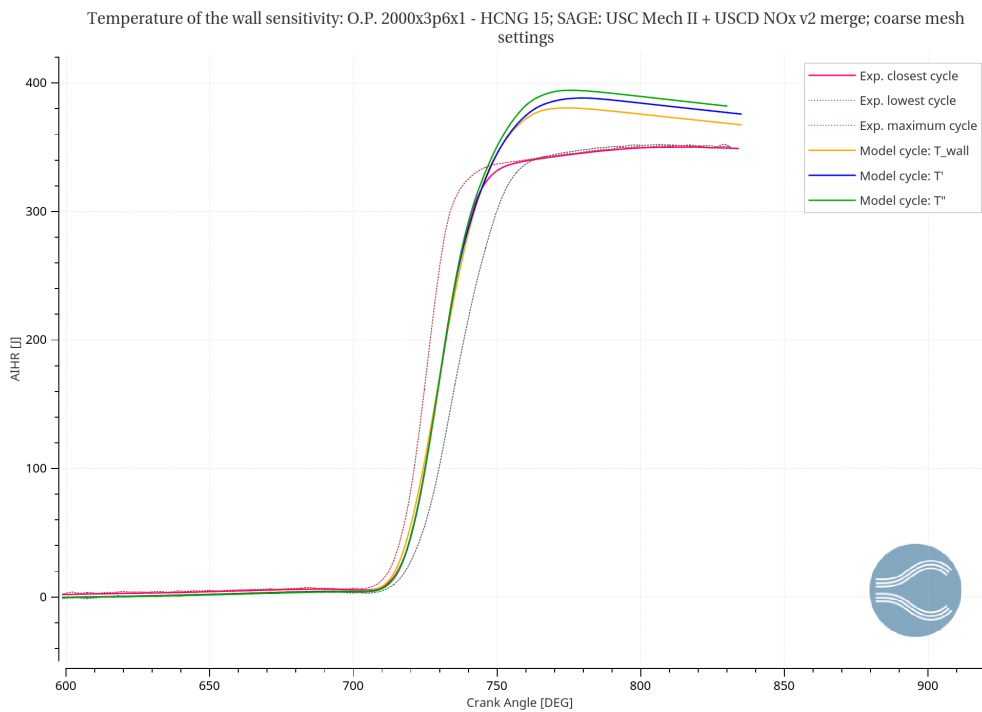


Figure 6.35: Integrated heat release; Temperature of the wall sensitivity; *SAGE: USC+USCD mechanisms merged*; coarse mesh settings, HCNG 15

Concerning the pollutant emissions, the table 17 sums up the different concentration errors obtained for each case. It is interesting to note that as the concentration of HCs increases, the NO_x decrease: since the temperature of the wall is reduced and then the heat exchange is encouraged, the temperature reached during the combustion process is lower. Thus, the fuel does not burn correctly and then even more unburned hydrocarbons are produced; conversely, the NO_x are less because the reaction mechanisms require more energy (and then temperature), hence the process slows down.

	Experimental value	$T=427\text{ K}$	$T=397\text{ K}$	$T=377\text{ K}$
\tilde{x}_{CO} error	5572 ppm	5731 ppm +2,9%	5730 ppm +2,8%	5613 ppm +0,7%
\tilde{x}_{NO_x} error	1880 ppm	2013 ppm +7%	1884 ppm +0,2%	1624 ppm -13,6%
\tilde{x}_{CO_2} error	103857 ppm	96262 ppm -7,3%	96187 ppm -7,4%	96277 ppm -7,3%
\tilde{x}_{HC} error	327 ppm	62 ppm -81%	70,3 ppm -78,5%	75,6 ppm -76,9%

Table 17: Pollutant emissions results; *SAGE-USC+USCD merged*; Temperature of the wall sensitivity; coarse mesh settings, HCNG 15

Unfortunately, even if there is a raise of the hydrocarbons, the values obtained from these three simulations are still far from the experimental measurements. Thus, the reduction of the wall temperature does not provide satisfactory improvements and then the case with T' and T'' have been rejected. Another strategy should be adopted like the LHV correction or the addition of the crevice volume.

6.2.6 LHV correction

There are two reasons why the LHV (lower heating value) has been corrected:

- **Energy:** the total energy in the chamber (HRR and $AIHR$) and the burn rate obtained are too high and too slow respectively, thus a reduction of the LHV can give better results.
- **Emissions:** since the hydrocarbons obtained from the model are very few, a reduction of the LHV may get worse the combustion process, promoting the formation of HC. Obviously, also the other species will be influenced by this correction.

The LHV is computed by CONVERGE by means of the `hidden.in` file, where the components of the fuel are specified as mass fraction. For the case with HCNG-15, the LHV computed is 50,87 MJ; thus, other two value reduced by 3,5% and 5% respectively are carried out obtaining $LHV = 48,15$ MJ and 48,45 MJ.

The Figures 6.36 and 6.42 show the best cycles obtained with the three LHVs:

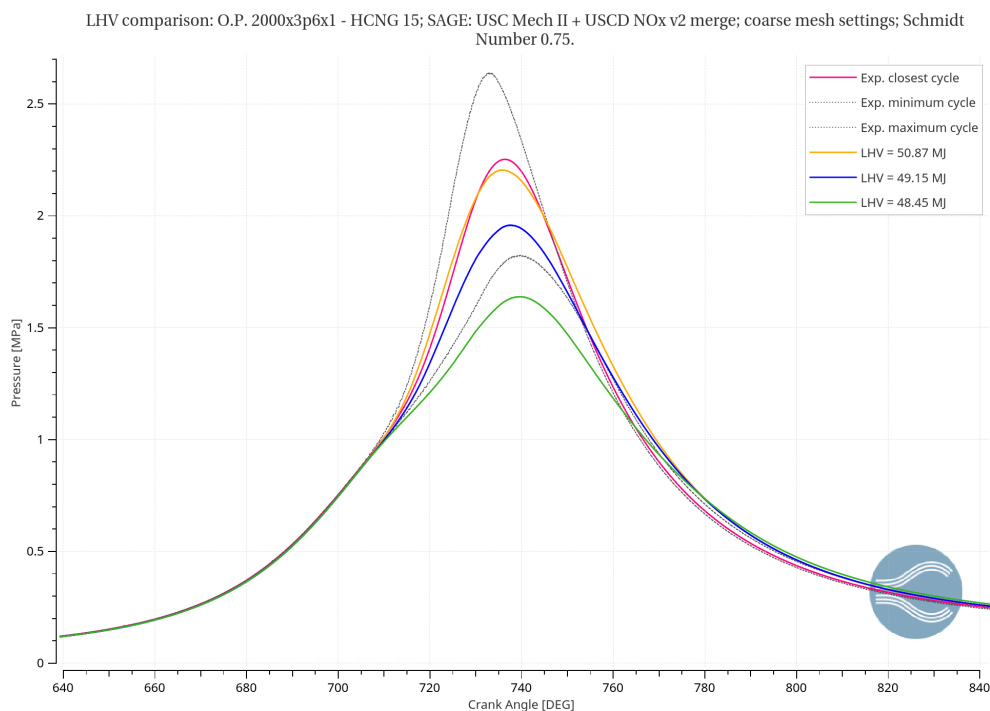


Figure 6.36: Pressure in cylinder 1; LHV sensitivity; *SAGE: USC+USCD mechanisms merged*; coarse mesh settings, HCNG 15

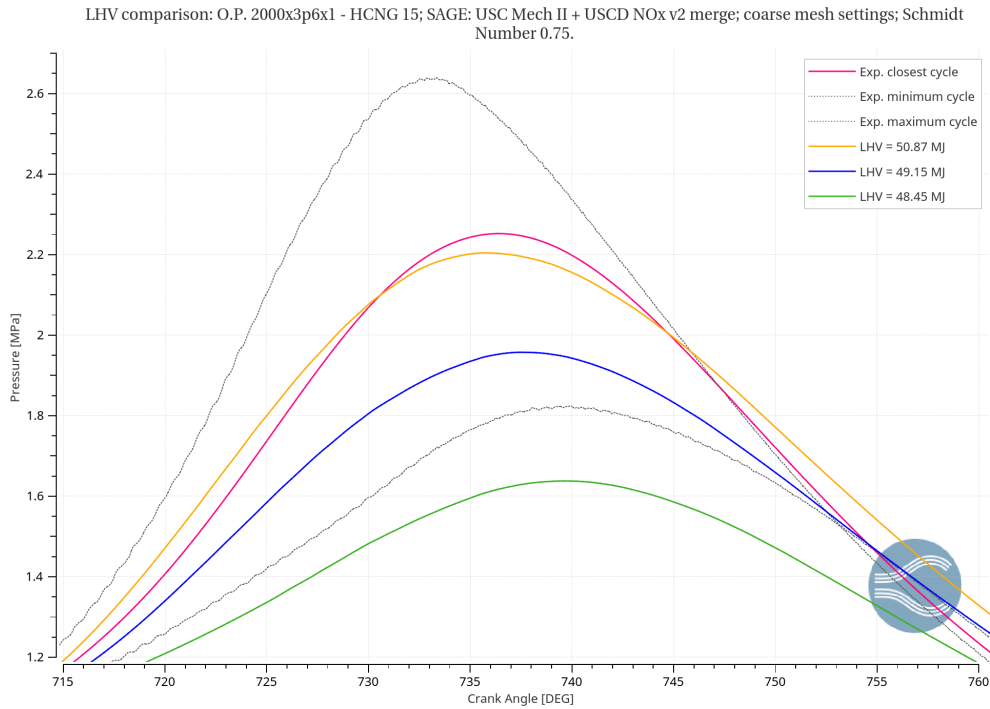


Figure 6.37: Zoom: Pressure in cylinder 1; LHV sensitivity; *SAGE*: *USC+USCD mechanisms merged*; coarse mesh settings, HCNG 15

As we can see, the pressure is very sensitive to the LHV variation in fact the pressure peaks are far apart from the experimental one and they are not acceptable: 1,98 MPa for LHV = 49,15 MJ (error of -13%) and 1,63 MPa for LHV = 48,45 MJ (error of -27%).

The *HRR* and *AIHR* get worse as well, as shown in Figure 6.38 and 6.39:

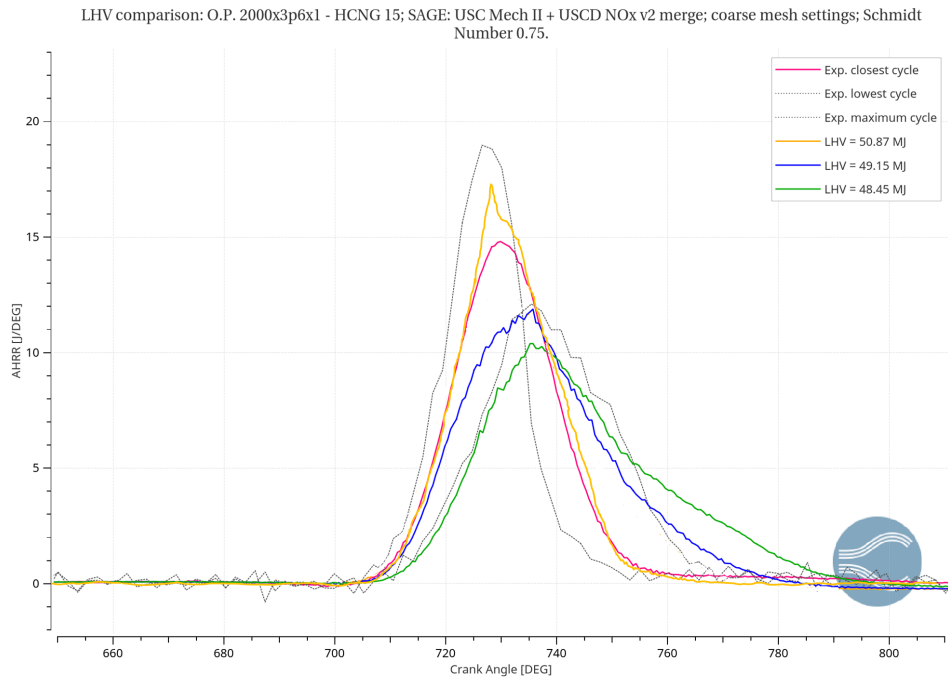


Figure 6.38: Heat release rate; LHV sensitivity; *SAGE: USC+USCD mechanisms merged*; coarse mesh settings, HCNG 15

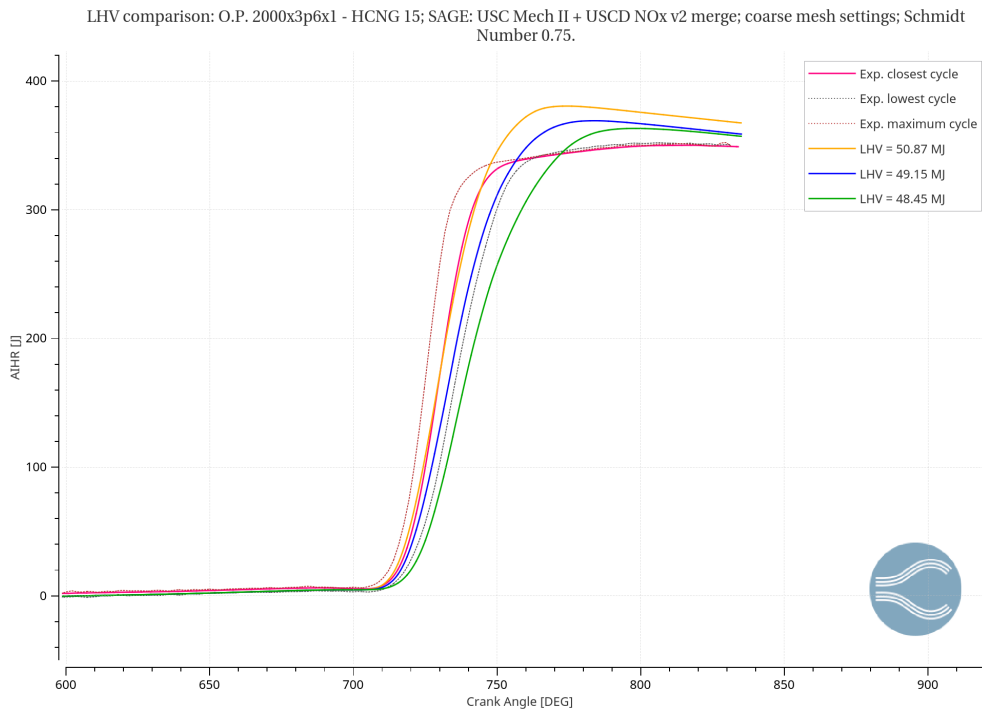


Figure 6.39: Integrate heat release; LHV sensitivity; *SAGE: USC+USCD mechanisms merged*; coarse mesh settings, HCNG 15

As expected, the peaks of energy decrease but unfortunately their location is shifted rightward by almost 10 CAD (figure 6.38); then the heat release rate between 740 CAD and 780 CAD (expansion phase) is higher than the experimental profile. All this has consequences on the *AIHR* where, although the energy peaks decrease as well, the slope of the curve is different and the burn rate is getting slower.

Finally, considering the pollutant emissions results (table 18) we can see that all the species are affected by the LHV reduction, in particular the NOx which are extremely few in comparison with the experimental values (53,6% and 81,7% less). In addition, no improvement has been achieved for the HCs so also in this case the two models with LHV reduced have been rejected.

	Exp. value	LHV=50,87 MJ	LHV=49,15 MJ	LHV=48,45 MJ
\tilde{x}_{CO}	5572 ppm	5731 ppm	5330 ppm	5301 ppm
error		+2,9%	-4,3%	-4,9%
\tilde{x}_{NO_x}	1880 ppm	2013 ppm	871 ppm	343 ppm
error		+7%	-53,6%	-81,7%
\tilde{x}_{CO_2}	103857 ppm	96262 ppm	96830 ppm	96632 ppm
error		-7,3%	-6,8%	-7%
\tilde{x}_{HC}	327 ppm	62 ppm	49 ppm	71 ppm
error		-81%	-84,8%	-78%

Table 18: Pollutant emissions results; *SAGE-USC+USCD merged*; LHV sensitivity; coarse mesh settings, HCNG 15

6.2.7 Crevice volume

One of the major sources for the formation of hydrocarbons is the crevice volume, in particular between cylinder and piston and around the intake and exhaust valves. In order to simplify the model, the crevice volume has not been included in the geometry so far; however, since the emission analysis is now discussed in this thesis work, the model must be more detailed and has to include this fundamental source of hydrocarbons.

Geometry

The Figure 6.40 shows a 3D plot of the crevice volume and a section of the cylinder:

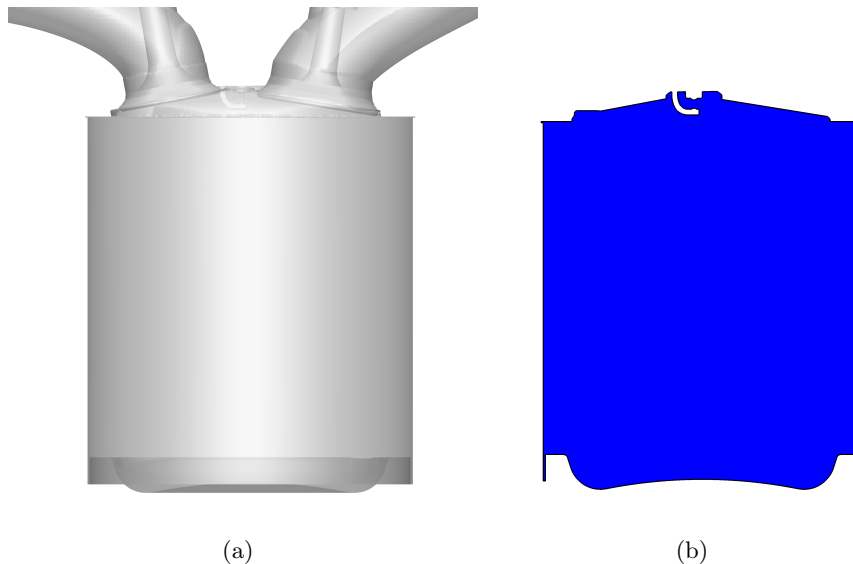


Figure 6.40: (a) 3D picture of the cylinder; (b) section of the cylinder

As first attempt, a volume of height 6,1 mm has been created between cylinder and piston. Obviously, the addition of volume changes the compression ratio of the cylinder; for that reason, the TDC of the piston has been changed in order to maintain constant that value. Thus, the new value of the compression ratio is 9,83707 instead of 9,79906 with an error of 0,4%, which is acceptable.

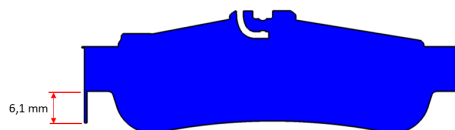


Figure 6.41: Height of the crevice volume

Crevice volume sensitivity

The pressure profiles obtained by using the crevice volume are shown in the following figures:

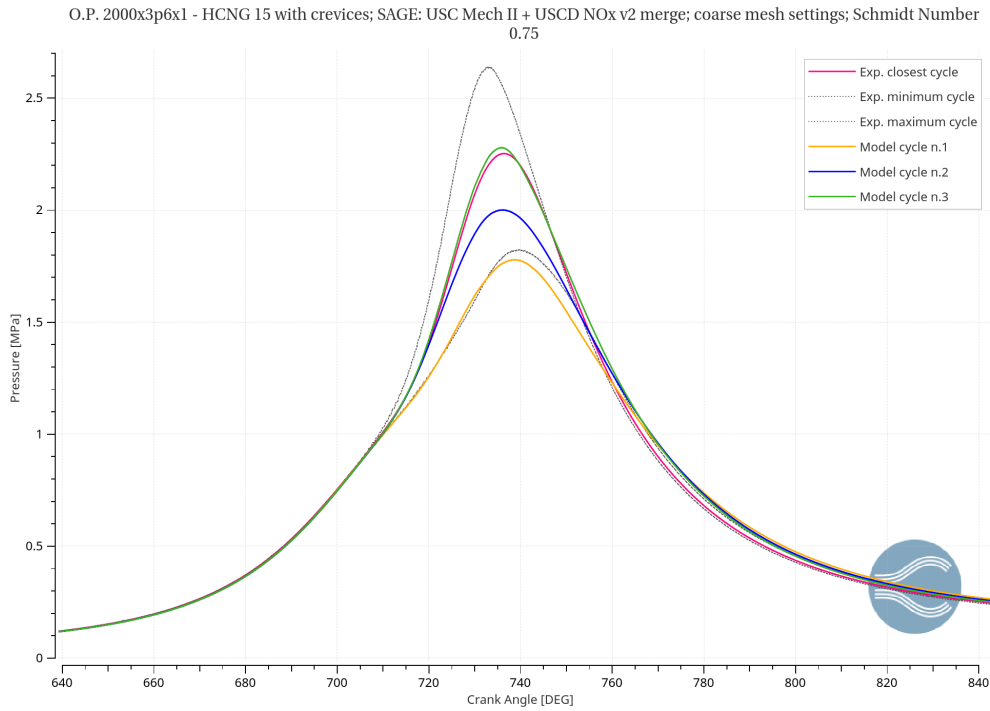


Figure 6.42: Pressure in cylinder 1; crevice volume addition; *SAGE: USC+USCD mechanisms merged*; coarse mesh settings, HCNG 15

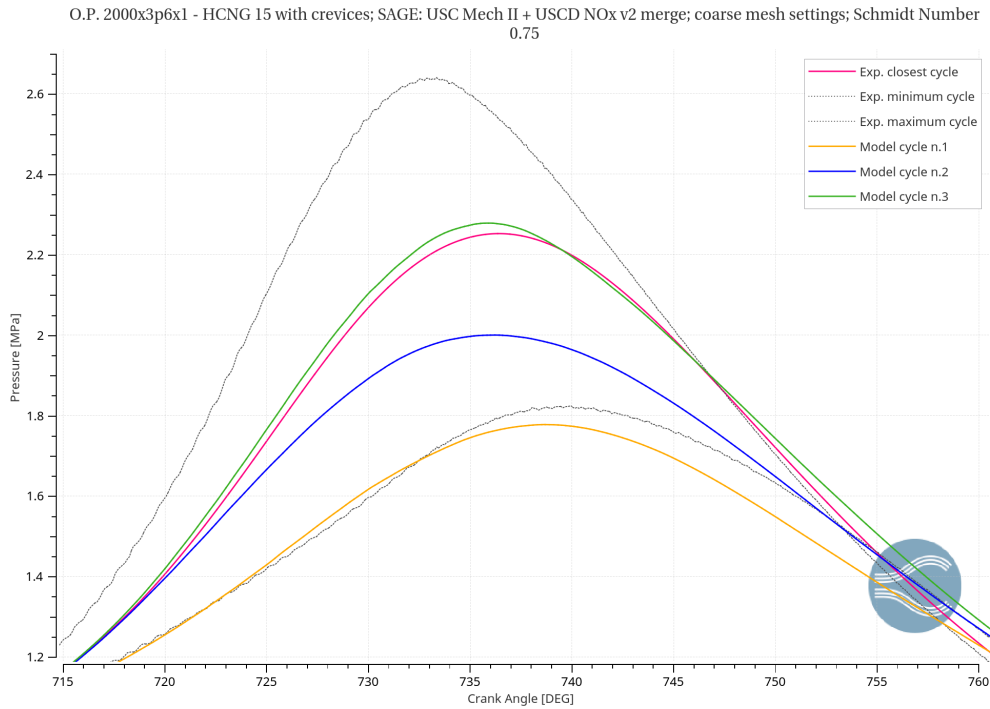


Figure 6.43: Zoom: Pressure in cylinder 1; crevice volume addition; *SAGE*: *USC+USCD mechanisms merged*; coarse mesh settings, HCNG 15

The best cycle is the model cycle number 3, with a peak pressure of 2,27 MPa against 2,25 MPa of the experimental closest cycle; in addition the compression phase is still acceptable and there is just a little overestimation of the pressure in the expansion phase, between 760 CAD and 780 CAD. Overall, the model cycle number 3 is acceptable.

The *HRR* values obtained (Figure 6.47) are very good: the energy peak in fact is now very close to the experimental one and the profile follows very well the combustion phase of the pink line. Unfortunately, there is still an overestimation of the energy between 740 CAD and 780 CAD but as overall an improvement of the heat release rate is achieved. Furthermore, the peak of the integrated heat release in Figure 6.48 is closer to the experimental closest cycle than the previous case.

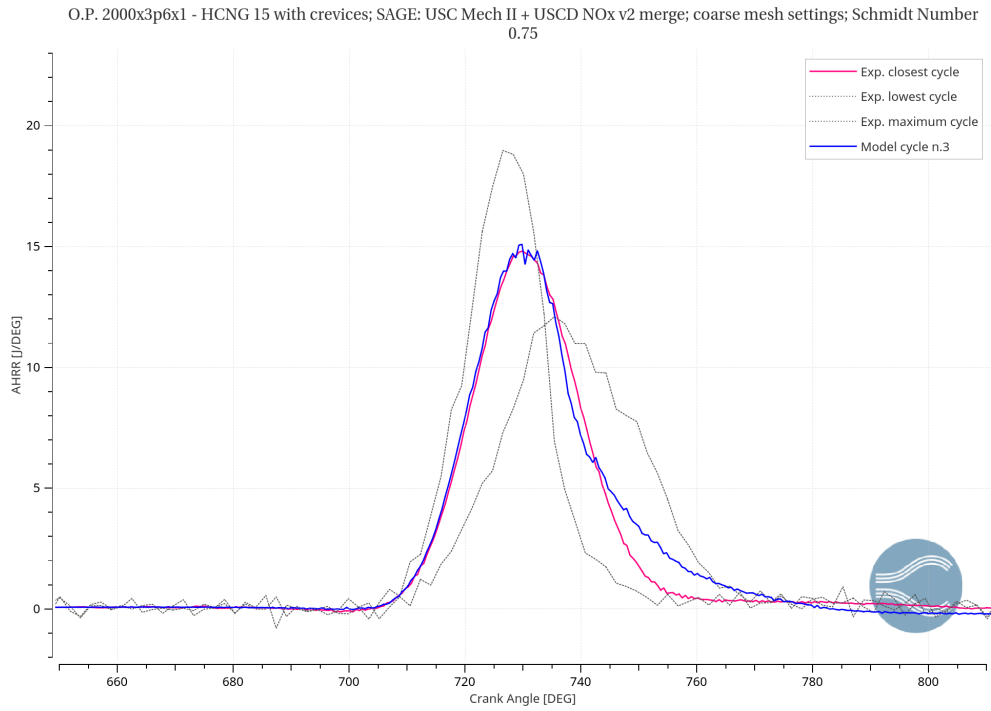


Figure 6.44: Heat release rate; crevice volume addition; *SAGE: USC+USCD mechanisms merged*; coarse mesh settings, HCNG 15

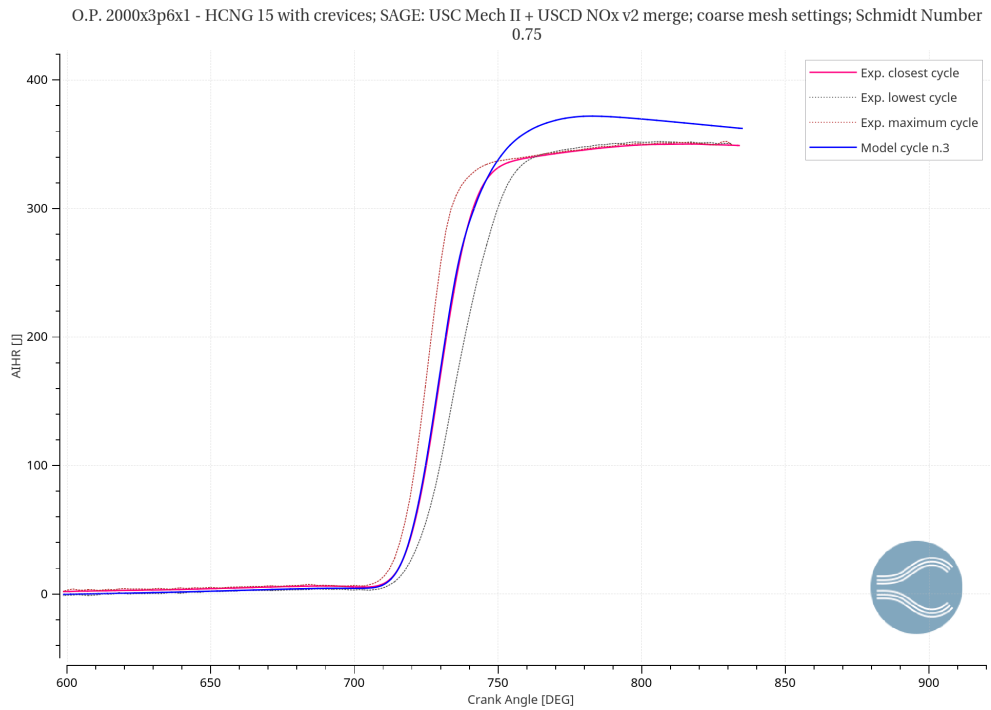


Figure 6.45: Integrated heat release; crevice volume addition; *SAGE: USC+USCD mechanisms merged*; coarse mesh settings, HCNG 15

In order to see the influence of the crevice volume, a comparison with the previous case (without crevices) could be useful. The Figure 6.46 shows that there are not great differences in terms of pressure, which are acceptable in both cases.

Concerning the *HRR* and *AIHR*, Figure 6.47 and 6.48 highlight the improvements achieved, mentioned before.

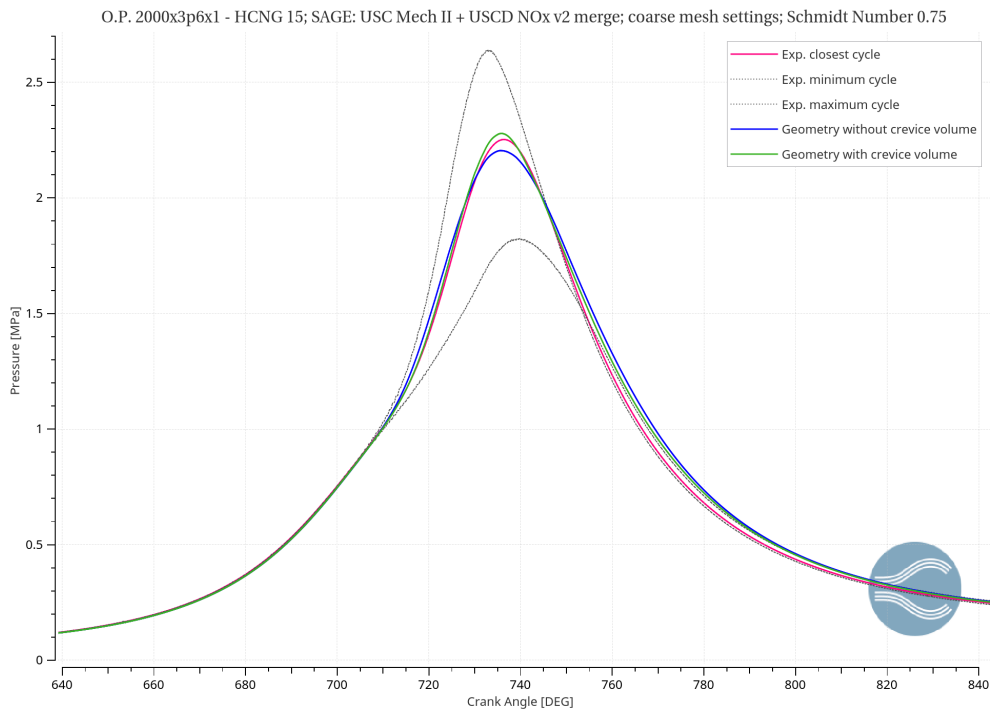


Figure 6.46: Pressure in cylinder 1; *SAGE: USC+USCD mechanisms merged*; coarse mesh settings, HCNG 15

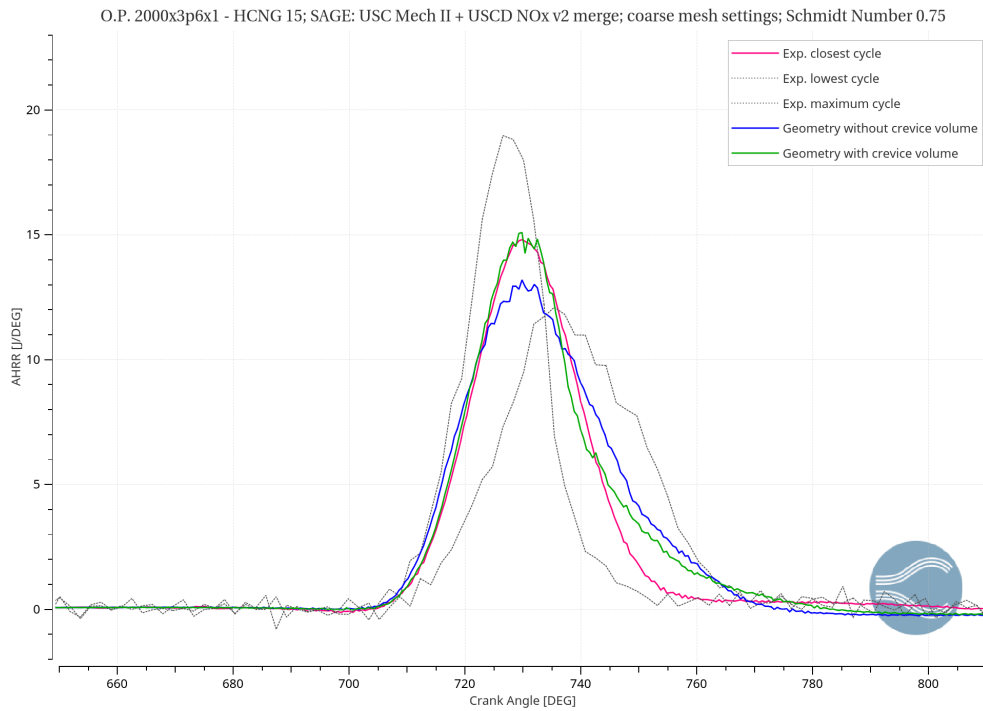


Figure 6.47: Heat release rate; *SAGE: USC+USCD mechanisms merged*; coarse mesh settings, HCNG 15

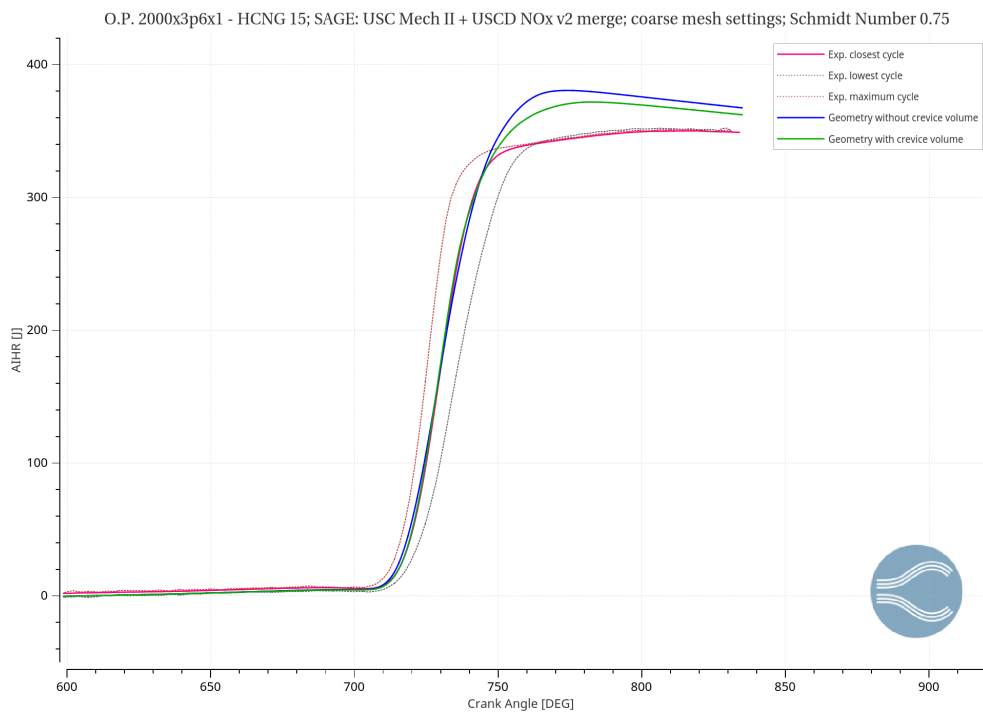


Figure 6.48: Heat release rate; *SAGE: USC+USCD mechanisms merged*; coarse mesh settings, HCNG 15

Finally, the table 19 shows a comparison between the emission results obtained by considering the model with and without crevices. It is clear that the biggest difference of the results concerns the unburned hydrocarbons: there is in fact a great increase of \tilde{x}_{HC} but obviously the error is extremely high (+790%). Hence, it is possible to affirm that \tilde{x}_{HC} is very sensitive to the crevice volume and a compromise solution must be adopted. For that reason, the volume of the crevices has been reduced two times and a crevice volume sensitivity has been ran.

	Exp. value	Model without crevices	Model with crevices
\tilde{x}_{CO} error	5572 ppm	5731 ppm +2,9%	5921 ppm +6,3%
\tilde{x}_{NO_x} error	1880 ppm	2013 ppm +7%	1842 ppm -2%
\tilde{x}_{CO_2} error	103857 ppm	96262 ppm -7,3%	92075 ppm -11,3%
\tilde{x}_{HC} error	327 ppm	62 ppm -81%	2932 ppm +790%

Table 19: Pollutant emissions results; *SAGE-USC+USCD merged*; LHV sensitivity; coarse mesh settings, HCNG 15

As Figure 6.49 shows, the height of the crevices has been reduced from 6,1 mm to 3,6 mm (*Medium* crevice volume) and 2,1 mm (*Small* crevice volume)

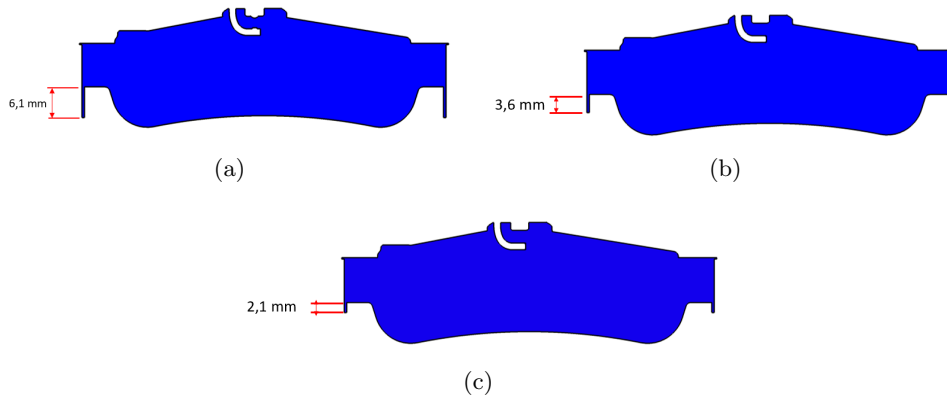


Figure 6.49: (a) *High* crevice volume; (b) *Medium* crevice volume; (c) *Small* crevice volume

***Medium* crevice volume**

As we can see from Figure 6.50 the best cycle is the model cycle number 3, even if also the model cycle number 2 is acceptable. Thus, in terms of pressure there are no worsening.

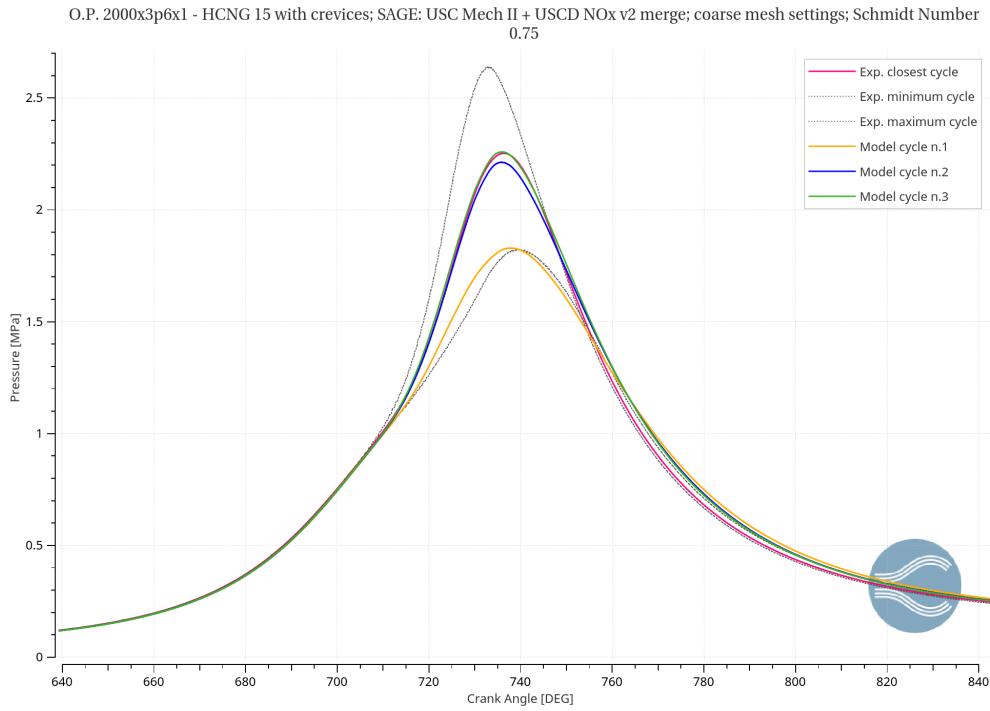


Figure 6.50: Pressure in cylinder 1; *Medium* crevice volume; *SAGE: USC+USCD mechanisms merged*; coarse mesh settings, HCNG 15

Furthermore, there is a small improvement for the *HRR* in fact the curve is closer to the experimental during the combustion phase in comparison with the previous case (Figure 6.51). The *AIHR* in Figure 6.52 is quite similar to the previous case and presents still a higher energy peak and a long burn rate.

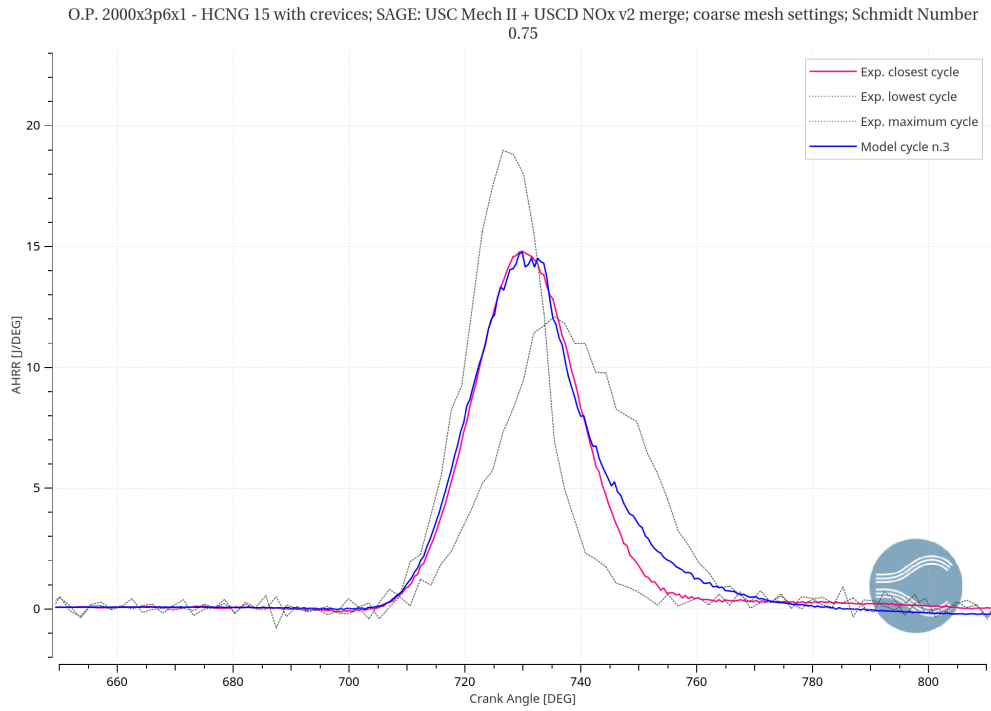


Figure 6.51: Heat release rate; *Medium* crevice volume; *SAGE: USC+USCD mechanisms merged*; coarse mesh settings, HCNG 15

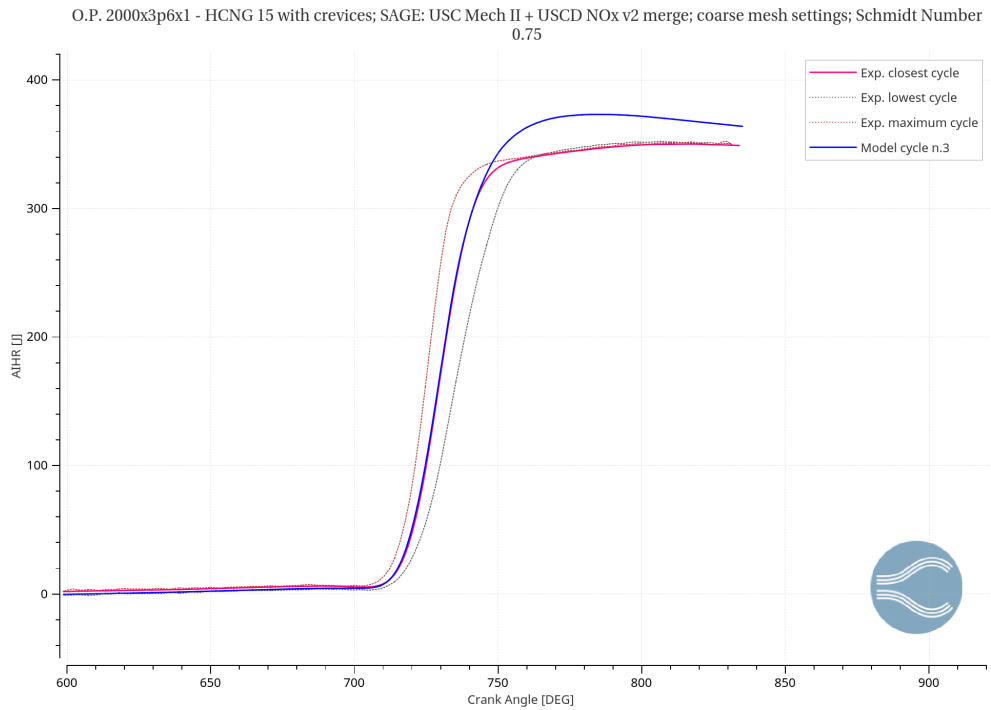


Figure 6.52: Integrated heat release; *Medium* crevice volume; *SAGE: USC+USCD mechanisms merged*; coarse mesh settings, HCNG 15

The great improvement is obtained for the pollutant emission (table 20) and in particular for \tilde{x}_{HC} ; reducing the height of the volume by few millimeters in fact the unburned hydrocarbons produced decrease from +790% to 372%, which means that the HC formation is very sensitive to the crevices dimension.

	Experimental value [ppm]	Simulation result [ppm]	Error
\tilde{x}_{CO}	5572	6137	+10,1%
\tilde{x}_{NO_x}	1880	2009	+6,8%
\tilde{x}_{CO_2}	103857	93625	-9,9%
\tilde{x}_{HC}	327	1549	372%

Table 20: Pollutant emissions results; *Medium* crevice volume; *SAGE-USC+USCD merged*; Schmidt Number = 0,75; coarse mesh settings, HCNG 15

Small crevice volume

The best cycle obtained by using the smallest crevice volume is the model cycle number 2, which peak pressure is 2,23 MPa (0,9% less than the experimental peak).

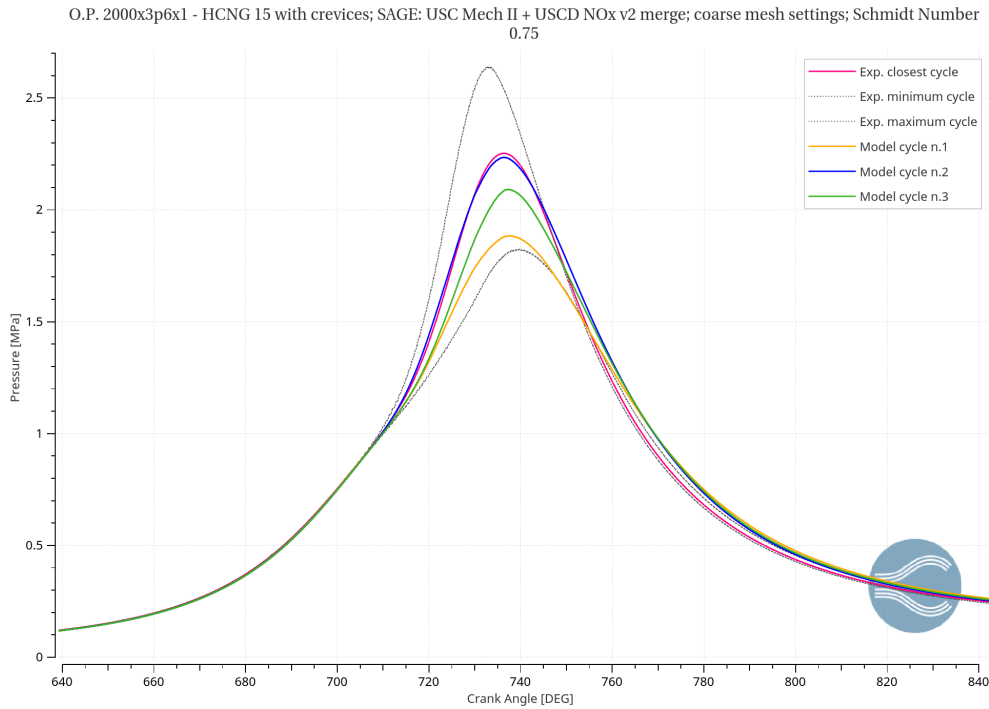


Figure 6.53: Pressure in cylinder 1; *Small* crevice volume; *SAGE: USC+USCD mechanisms merged*; coarse mesh settings, HCNG 15

The *HRR* and the *AIHR* are very similar to the case with *Medium* crevice volume and the results are quite good (Figure 6.54 and 6.55).

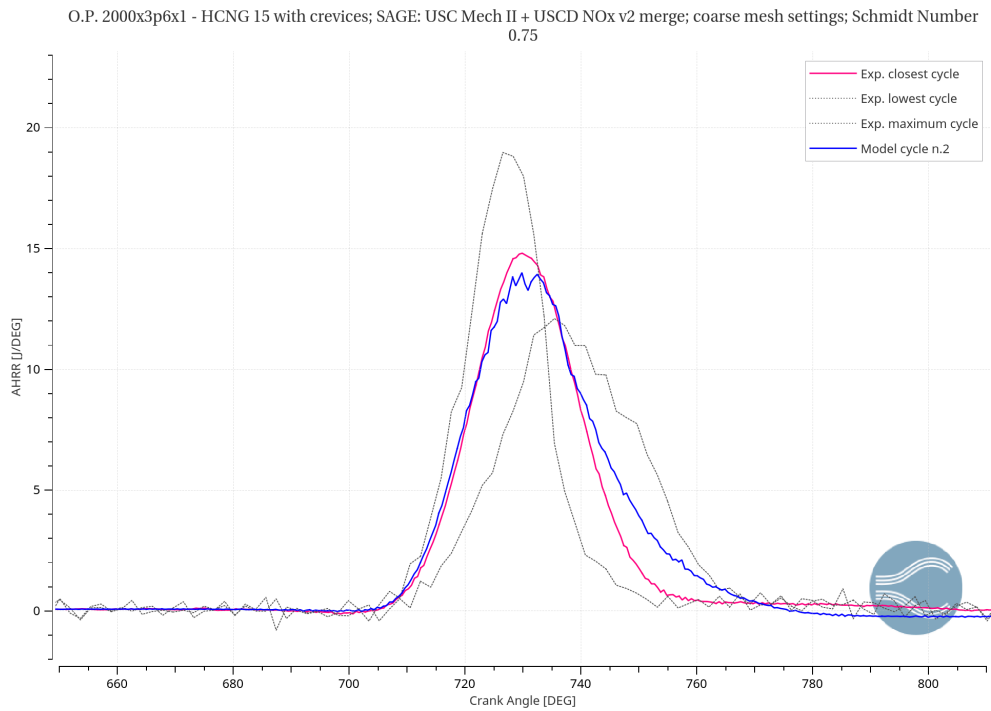


Figure 6.54: Heat release rate; *Small* crevice volume; *SAGE: USC+USCD mechanisms merged*; coarse mesh settings, HCNG 15

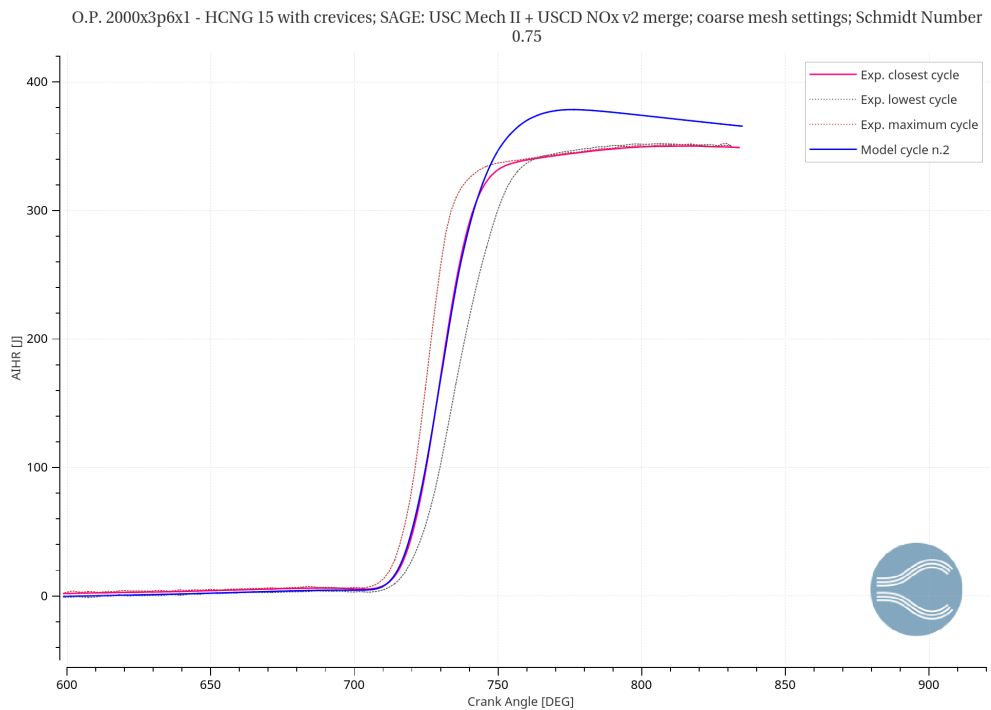


Figure 6.55: Integrated heat release; *Small* crevice volume; *SAGE: USC+USCD mechanisms merged*; coarse mesh settings, HCNG 15

As expected, from tabel 21 we can say that, while there are no great differences for the other species (which concentration are still close to the measurements), \tilde{x}_{HC} is smaller than the previous case and is only 15,5% bigger than the experimental value, which is acceptable.

	Experimental value [ppm]	Simulation result [ppm]	Error
\tilde{x}_{CO}	5572	5975	+7,2%
\tilde{x}_{NO_x}	1880	2016	+7,2%
\tilde{x}_{CO_2}	103857	95482	-8,1%
\tilde{x}_{HC}	327	378	15,5%

Table 21: Pollutant emissions results; *Small* crevice volume; *SAGE-USC+USCD merged*; Schmidt Number = 0,75; coarse mesh settings, HCNG 15

In order to highlight the sensitivity of the model to the crevices, a final comparison among *High*, *Medium* and *Small* crevice volume has been carried out.

Comparison

In Figure 6.56 the comparison between the pressure profiles is shown.

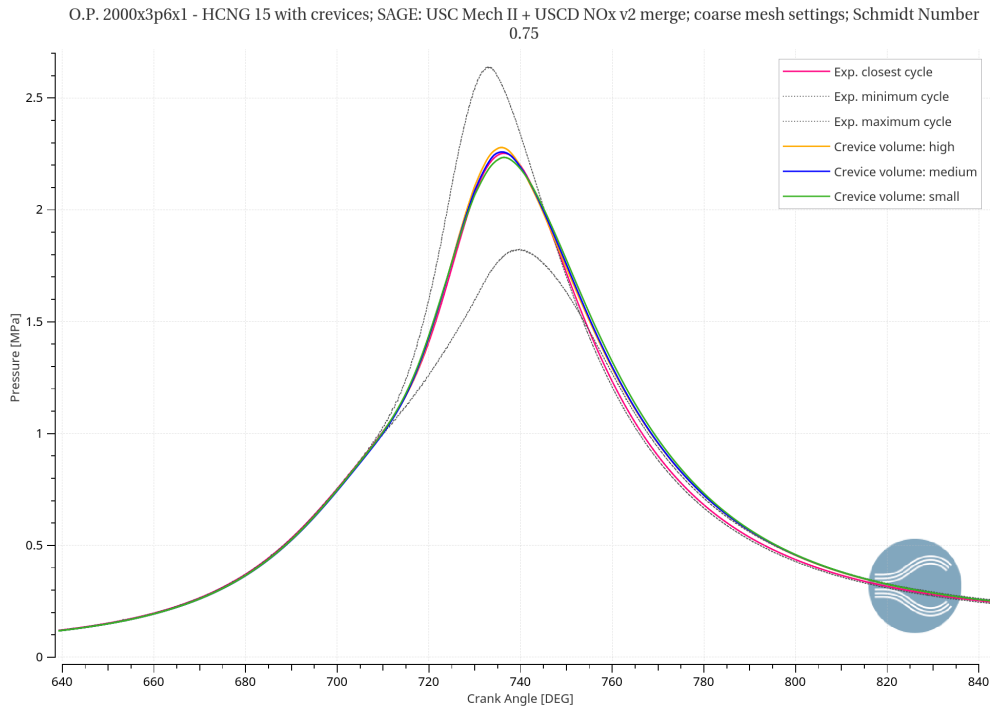


Figure 6.56: Pressure in cylinder 1; Crevice volume comparison; *SAGE: USC+USCD mechanisms merged*; coarse mesh settings, HCNG 15

As it is noticeable, there are no important differences among the best cycles of each case and peak pressure errors for *High*, *Medium* and *Small* crevice vol-

ume are 1,2%, 0,2% and -0,9% respectively, which are all acceptable.

The *HRR* (Figure 6.57) is also similar in the three cases, even if the *Small* crevice has a lower peak in comparison with the other two cases.

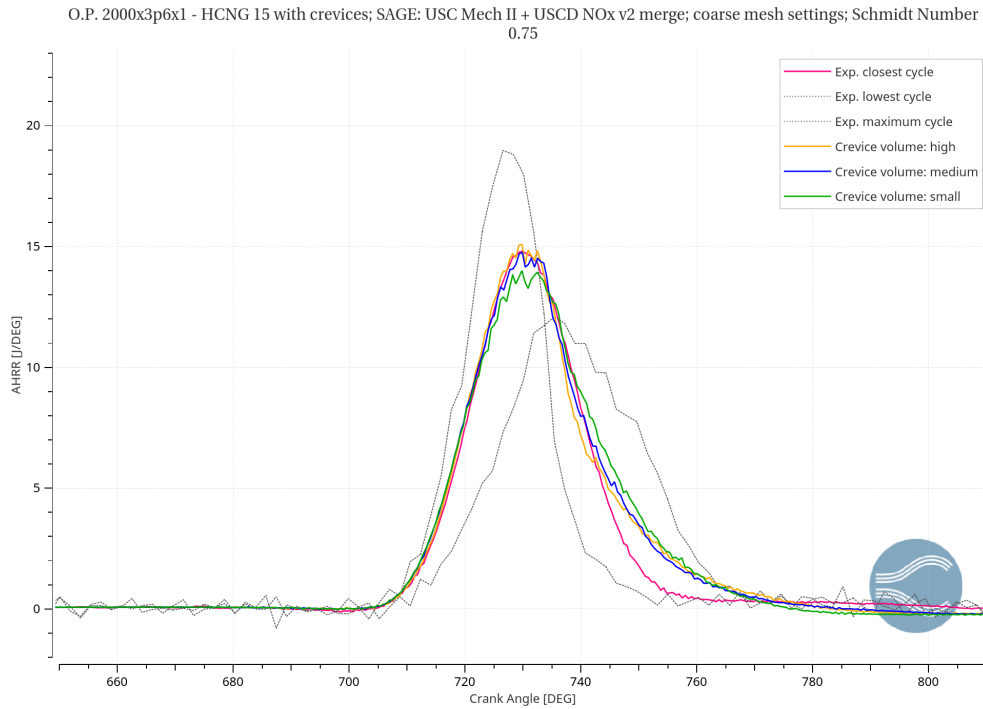


Figure 6.57: Heat release rate; Crevice volume comparison; *SAGE: USC+USCD mechanisms merged*; coarse mesh settings, HCNG 15

Furthermore, also the *AIHR* in figure 6.58 does not change by using different dimension of the crevices.

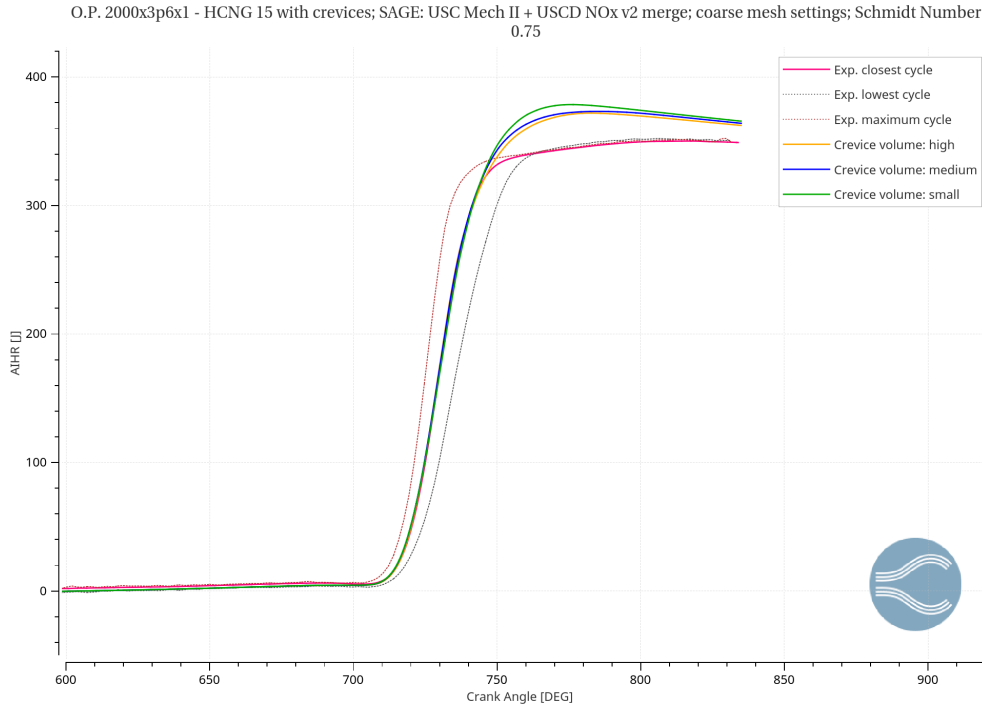


Figure 6.58: Integrated heat release; Crevice volume comparison; *SAGE: USC+USCD mechanisms merged*; coarse mesh settings, HCNG 15

The table 22 shows clearly how \tilde{x}_{HC} decreases with the reduction of the crevices, from 2932 ppm to 378 ppm (error of 15,5%). Since \tilde{x}_{CO} , \tilde{x}_{NO_x} and \tilde{x}_{CO_2} are also acceptable, the model with the **smallest** crevice volume represents the **best simulation** for the operating point 2000[rpm] x 3,6 [bar] x lambda = 1 with HCNG-15 as fuel.

	Exp. value	High volume	Medium volume	Small volume
\tilde{x}_{CO}	5572 ppm	5921 ppm	6137 ppm	5975
error		+6,3%	+10,1%	+7,2%
\tilde{x}_{NO_x}	1880 ppm	1842 ppm	2009 ppm	2016 ppm
error		-2%	+6,8%	+7,2%
\tilde{x}_{CO_2}	103857 ppm	92075 ppm	93625 ppm	95482 ppm
error		-11,3%	-9,9%	-8,1%
\tilde{x}_{HC}	327 ppm	2932 ppm	1549 ppm	378 ppm
error		+790%	+372%	+15,5%

Table 22: Pollutant emissions results; Crevice volume sensitivity; *SAGE-USC+USCD mechanisms merged*; coarse mesh settings, HCNG 15

6.3 O.P. 2000[rpm] x 3.6[bar] x lambda=1; HCNG 25

The analysis of the fuel HCNG-25, has been carried out in parallel with the case of the fuel HCNG-15. In general the same logical process and the same adjustment have been done, except in some case, where the previous results showed that any improvement had been obtained (e.g. through the wall temperature reduction and the LHV correction). Thus, as the previous case, also this time we start analyzing the numerical results obtained by using the *GRI Mech 3.0* reaction mechanism.

6.3.1 Base simulation: *GRI Mech 3.0*

The Figure 6.59 shows the results obtained by using this reaction mechanism. Two problems can be highlighted: the first cycle, which is not considered since it is a sort of "initialization" for the following two cycles, is very close to the experimental profile, while the model cycle number 2 and 3 are far (with errors for pressure peak magnitude of almost +20% and +10% respectively; figure 6.60). Secondly, there is a high CCV between the cycle number 2 and 3, even if they are into the boundaries (experimental maximum and minimum cycle).

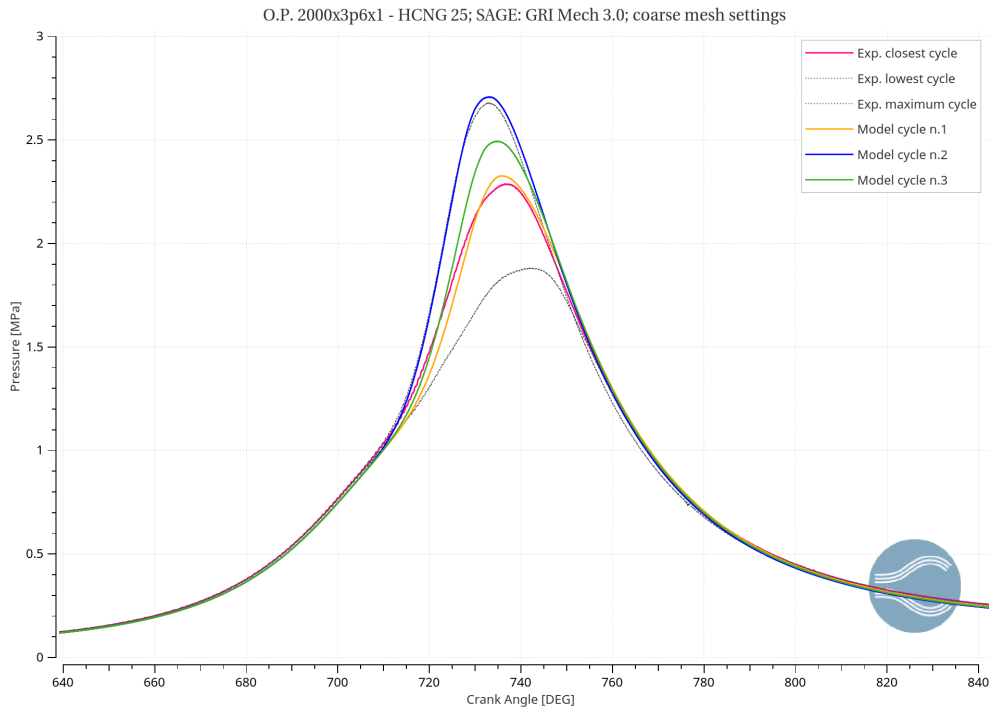


Figure 6.59: Pressure in cylinder 1; *SAGE: GRI Mech 3.0* mechanism; coarse mesh settings, HCNG 25

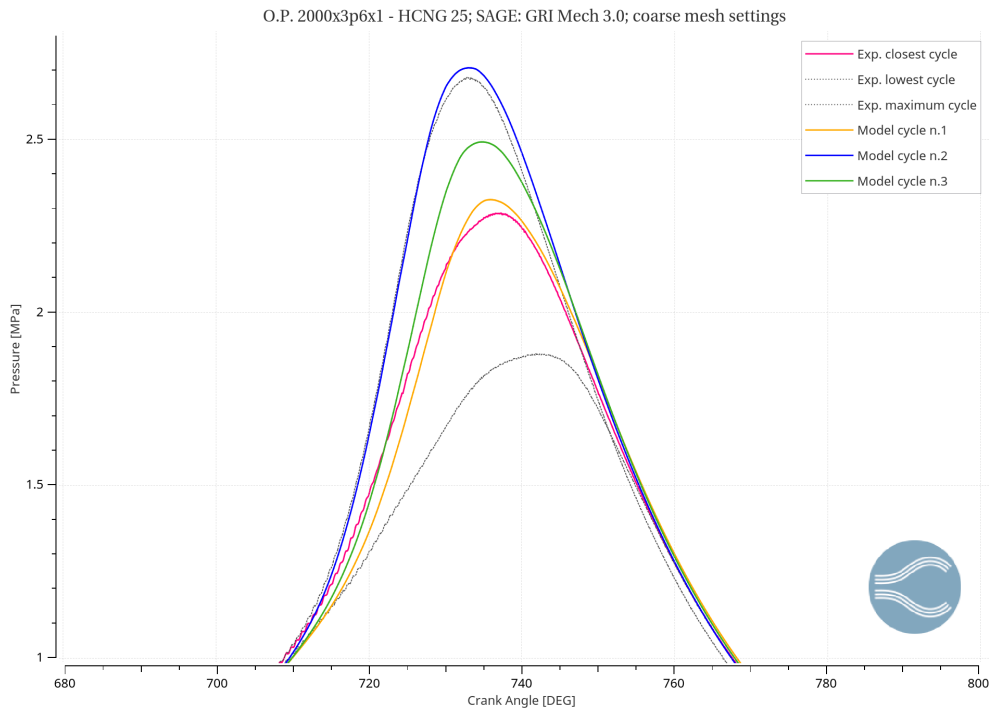


Figure 6.60: Zoom: pressure in cylinder 1; *SAGE: GRI Mech 3.0* mechanism; coarse mesh settings, HCNG 25

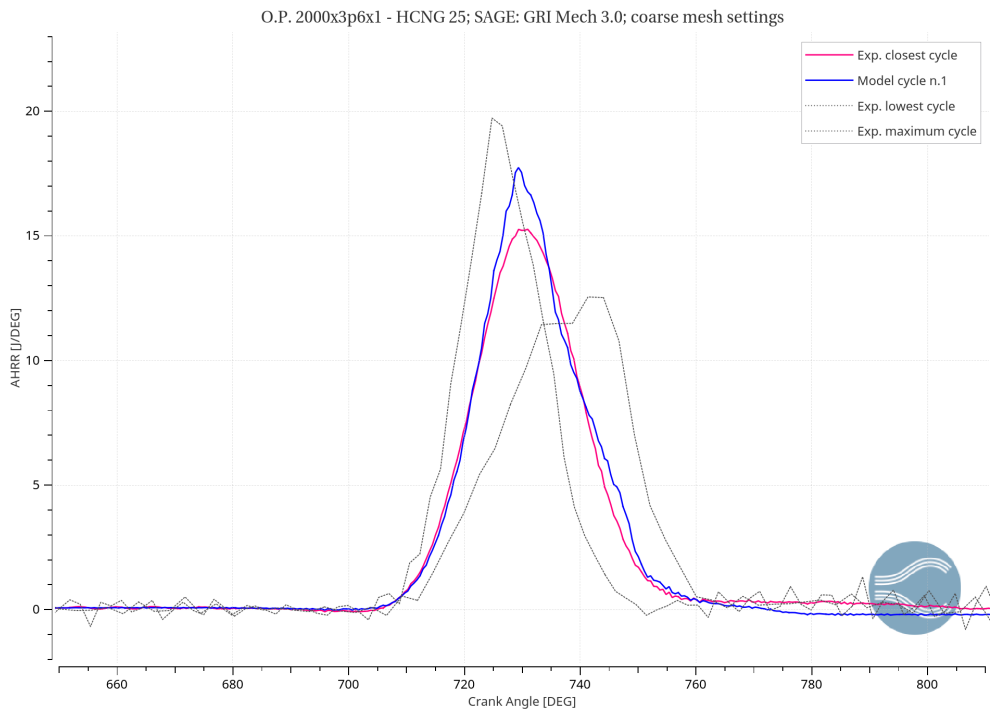


Figure 6.61: Heat release rate; *SAGE: GRI Mech 3.0* mechanism; coarse mesh settings, HCNG 25

The HRR curve, shown in figure 6.61, is quite good because the model cycle follows well the experimental closest cycle during the compression and expansion phase but presents a higher peak at 730 CAD; thus, the integrated heat release in Figure 6.62 reaches a higher value of energy and the burn rate is longer in comparison with the experimental cycle.

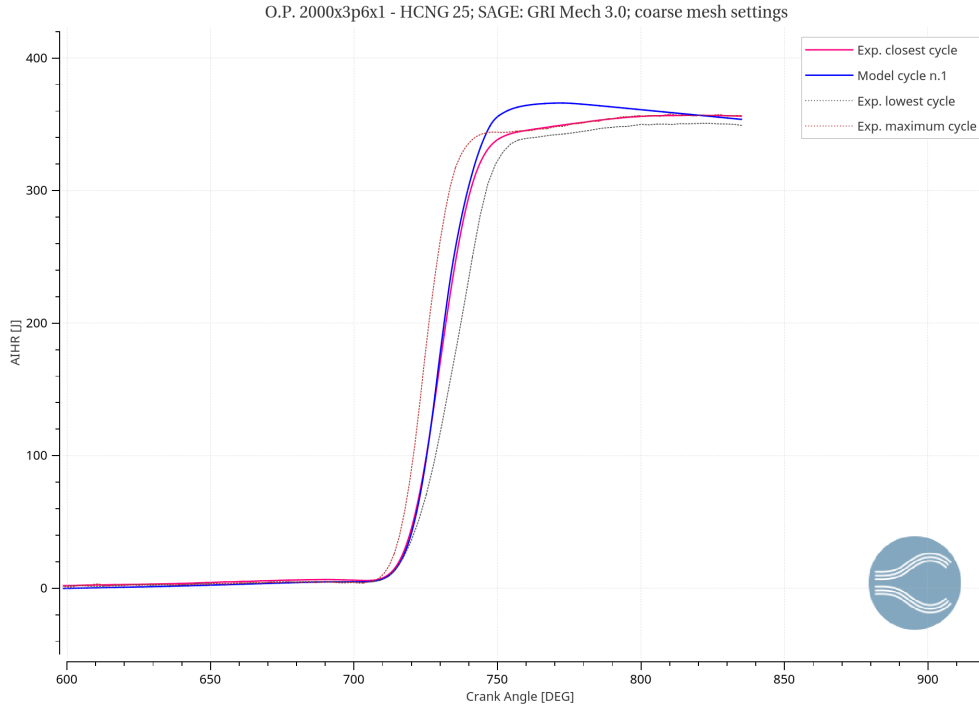


Figure 6.62: Integrated heat release; *SAGE: GRI Mech 3.0* mechanism; coarse mesh settings, HCNG 25

The pollutant emissions concentrations obtained with the *GRI Mech 3.0* mechanisms are not good here too, in particular for CO and HC (Table 23).

	Experimental value [ppm]	Simulation result [ppm]	Error
\tilde{x}_{CO}	5650	6611	+17%
\tilde{x}_{NO_x}	1818	1930	+6,2%
\tilde{x}_{CO_2}	101059	95366	-5,6%
\tilde{x}_{HC}	281	30	-89,3%

Table 23: Pollutant emissions; *SAGE: GRI Mech 3.0* mechanism; coarse mesh settings, HCNG 25

Furthermore, in order to check the CCV observed in Figure 6.59, three cycles more have been ran. The Figure 6.63 shows that even among the six cycles the variability of the pressure from cycle to cycle is very important.

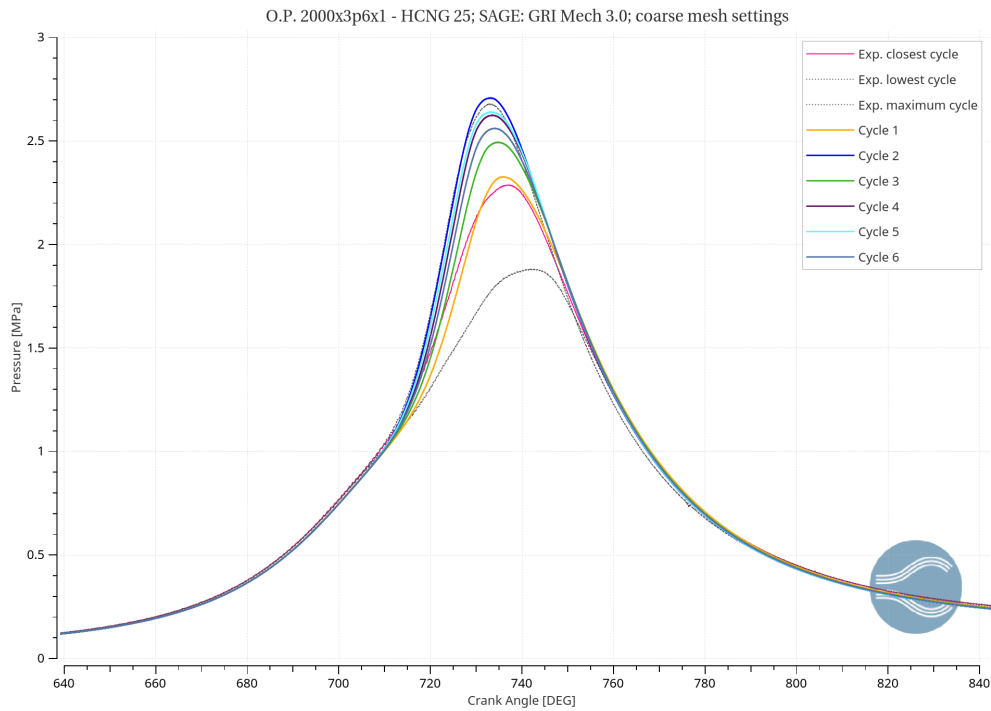


Figure 6.63: Pressure in cylinder 1; *SAGE: GRI Mech 3.0* mechanism; coarse mesh settings, HCNG 25

In conclusion, since the pressure results and the pollutant emissions concentrations obtained with *GRI Mech 3.0* are not satisfactory, the *USC mech II* has been used as first approach and then *USC+USCD mechanisms* merged.

6.3.2 USC mech II

As already seen for the case with HCNG-15, this mechanism gives underestimated values of the pressure in comparison with the *GRI* mechanisms (Figure 6.64): the peak pressure of the best cycle, which is the model cycle number 3, is 2,11 MPa so it is 4,5% lower than the experimental peak. Furthermore, while the compression phase is acceptable, the pressure profile during the expansion phase is almost 7% higher than the experimental closest cycle; obviously, it will negatively affect the *HRR* and *AIHR*.

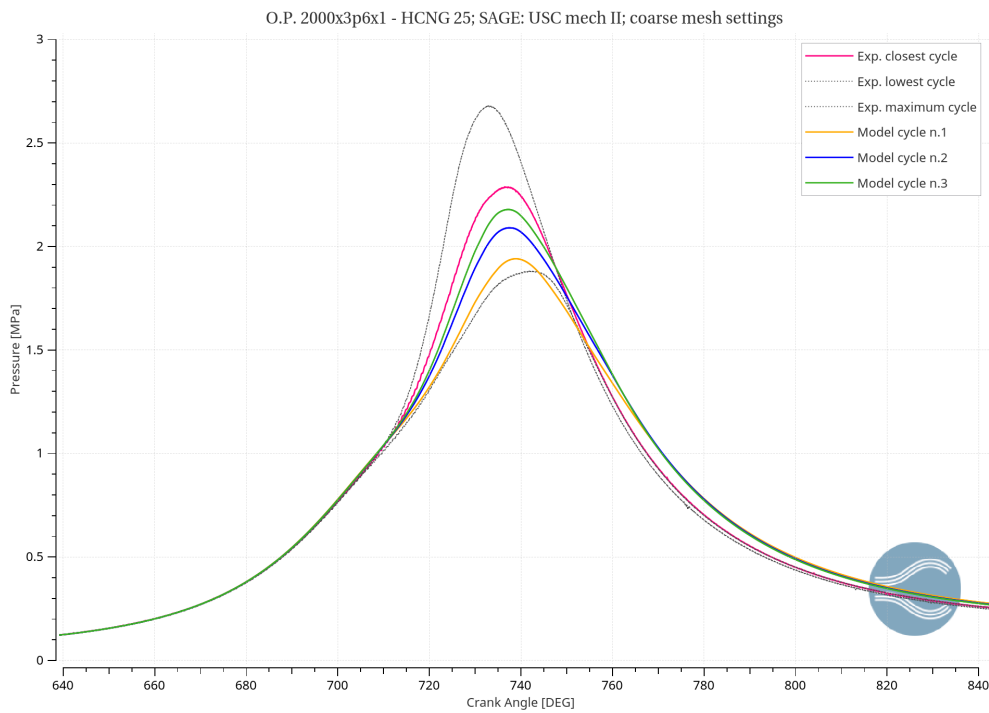


Figure 6.64: Pressure in cylinder 1; *SAGE: USC mech II*; coarse mesh settings, HCNG 25

Concerning the *HRR* in Figure 6.65, there is in fact an excess of energy between 740 CAD and 780 CAD, the expansion phase. Hence, although the *AIHR* follows well the experimental combustion process, it will have a higher peak of energy after 750 CAD (Figure 6.66).

The trapped mass error is +1,62% which is an acceptable result.

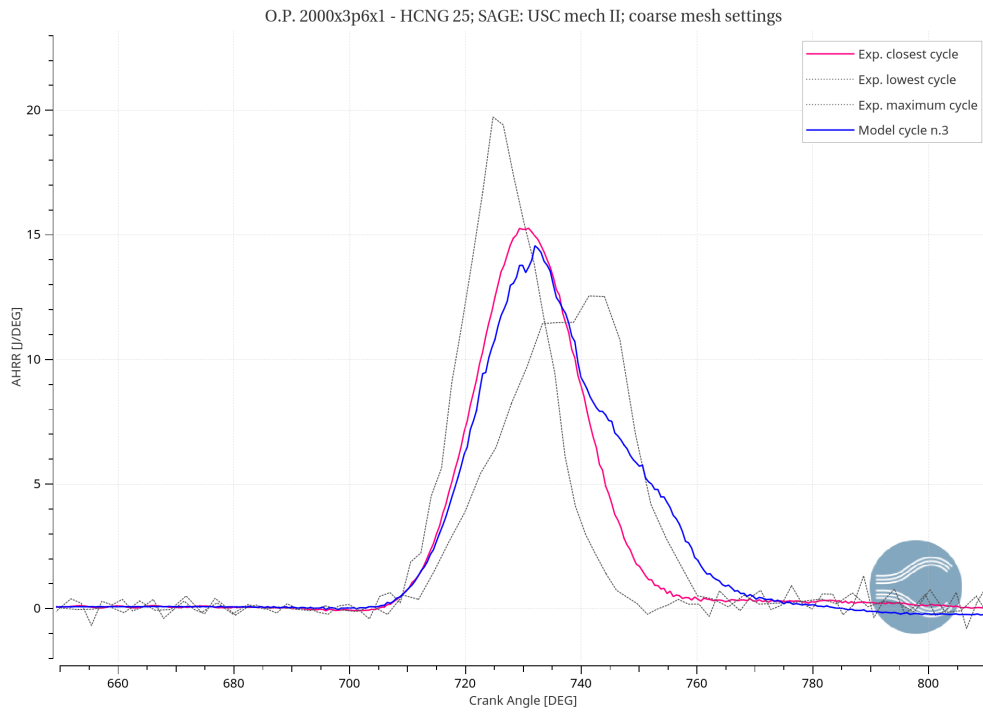


Figure 6.65: Heat release rate; *SAGE: USC mech II*; coarse mesh settings, HCNG 25

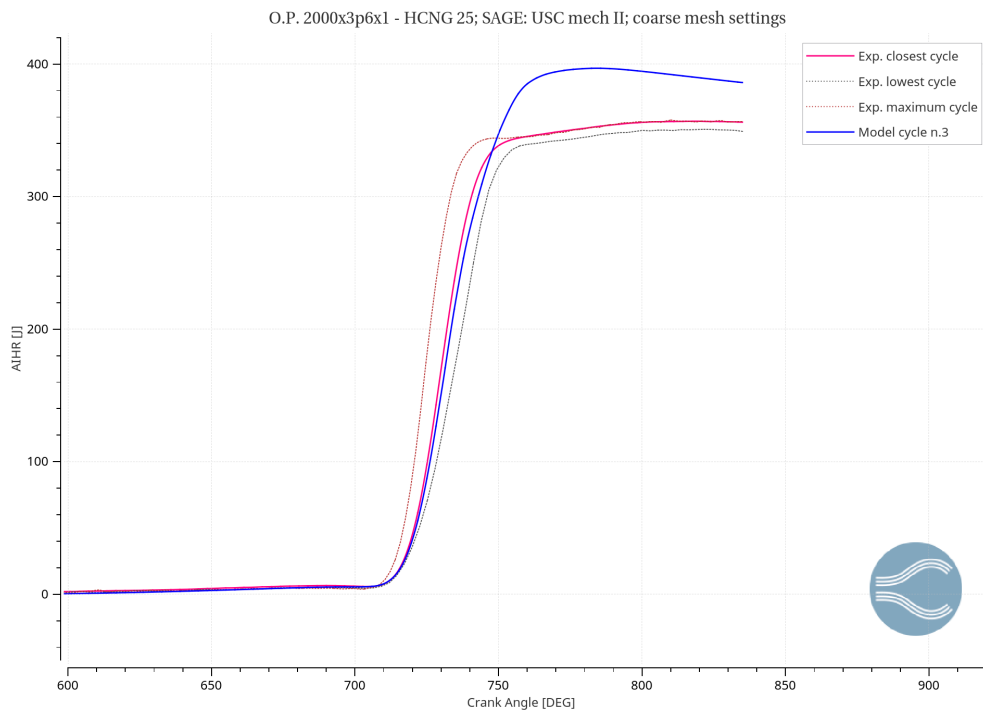


Figure 6.66: Integrated heat release; *SAGE: USC mech II*; coarse mesh settings, HCNG 25

In order to increase the underestimated value of the pressure, a numerical modification has been done: the variation of the monotone tolerance.

Monotone Tolerance variation

The monotone tolerance is the tolerance for the step flux limiter above which CONVERGE switches to a lower-order spatial discretization to preserve stability; it will switch in fact to a first-order upwind spatial discretization when the ratio of gradients on either side of a cell face exceeds the specified value. Thus, changing the value from $1e-05$ (default value) to $0,025$ we can obtain a wider range of tolerance; in this way it is possible to change the *diffusivity* of the combustion model.

[6]

The effect of this variation on the pressure is shown in Figure 6.67. As we can see, now the best cycle is the number 2 and the pressure peak error decreases from $-4,5\%$ to -1% . However, there is still a high error of the pressure during the expansion phase (around 7% at 770 CAD).

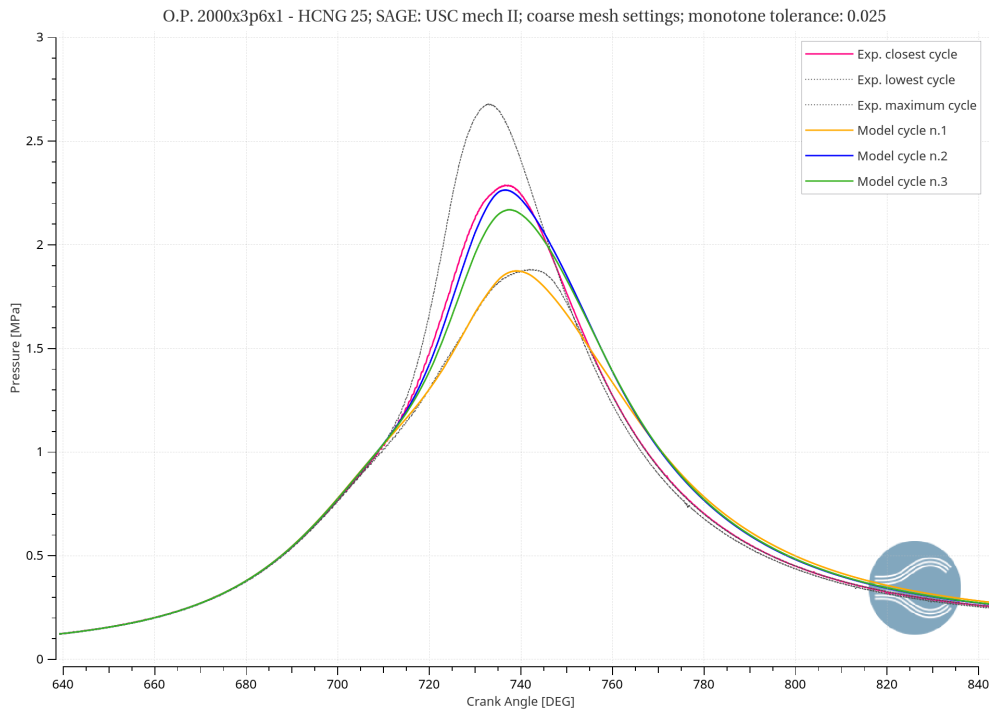


Figure 6.67: Pressure in cylinder 1; *SAGE: USC mech II*; Monotone tolerance $0,025$; coarse mesh settings, HCNG 25

In order to better understand the effect of the monotone tolerance, a comparison between the two cases might be useful. The improvement reached for the pressure is clearly visible in the following figure:

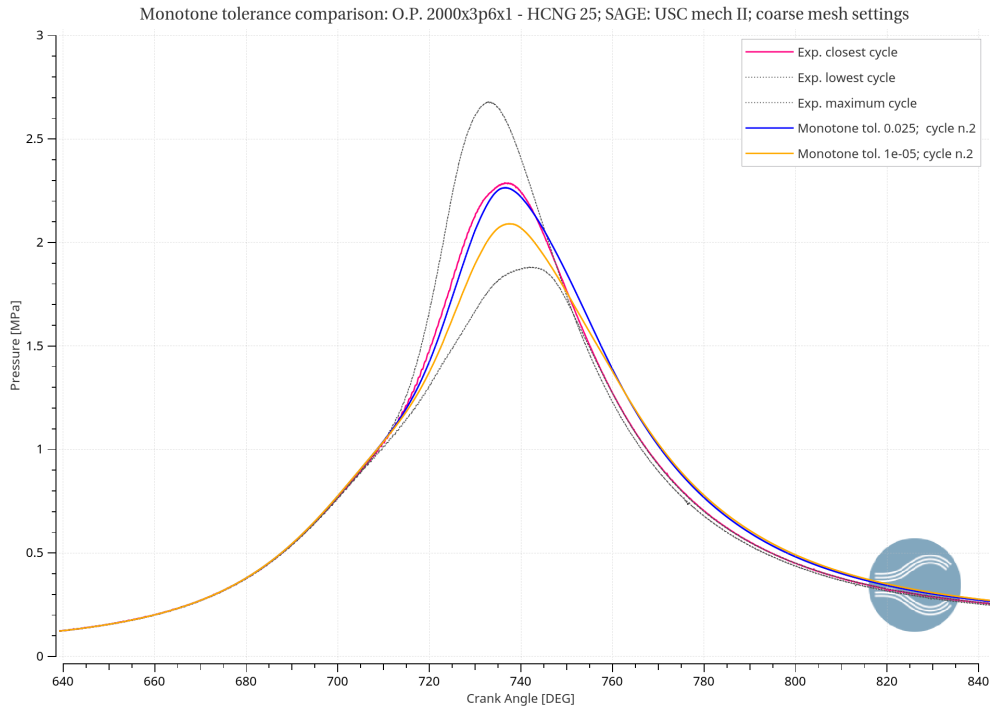


Figure 6.68: Pressure in cylinder 1; *SAGE: USC mech II*; Monotone tolerance comparison; coarse mesh settings, HCNG 25

On the other hand, there are no important differences for the *HRR* and the *AIHR* with the case with $1e-5$ as monotone tolerance, and the same problems of the excess of energy occurs (figures 6.69 and 6.70).

As final comparison, the table 24 shows the different emission results obtained in both cases. It should be noted the raise of the NO_x concentration with monotone tolerance 0,025: in this case in fact the pressure is higher so \tilde{x}_{NO_x} , which is strictly related with the temperature and then with the pressure, increases. That is why, the variation of the monotone tolerance is a "numerical" way to change the NO_x concentration; in general, the percentage of this particular species in the exhaust gas grows up by changing the value from $1e-5$ to 0,025.

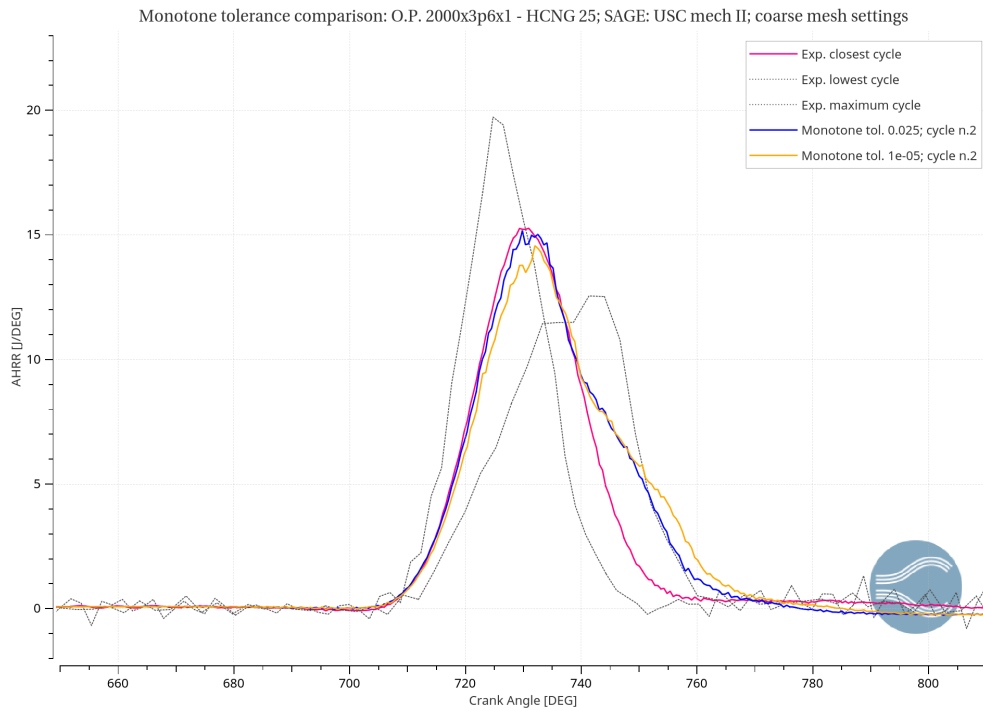


Figure 6.69: Heat release rate; *SAGE: USC mech II*; Monotone tolerance comparison; coarse mesh settings, HCNG 25

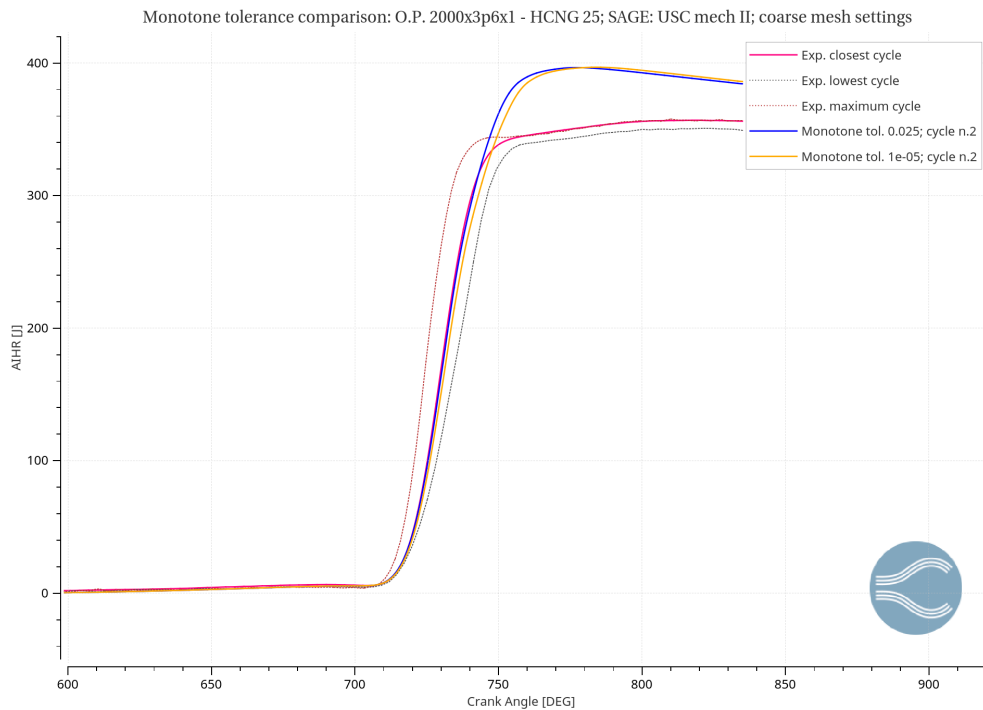


Figure 6.70: Integrated heat release; *SAGE: USC mech II*; Monotone tolerance comparison; coarse mesh settings, HCNG 25

	Exp. value	Monotone tolerance 1e-05	Monotone tolerance 0,025
\tilde{x}_{CO} error	5650 ppm	5381 ppm -4,8%	5374 ppm -4,9%
\tilde{x}_{NO_x} error	1818 ppm	1978 ppm +8,8%	2228 ppm +22,5%
\tilde{x}_{CO_2} error	101059 ppm	96755 ppm -4,3%	96755 ppm -4,3%
\tilde{x}_{HC} error	281 ppm	25,61 ppm -90,9%	25,65 ppm -90,9%

Table 24: Pollutant emissions results; Monotone tolerance comparison; *SAGE: USC mech II*; coarse mesh settings, HCNG 25

Unfortunately, as already cited before (see chapter 6.2.2), the *USC mech II* is not suitable for the emission analysis because it contains few species and reactions in particular for NO_x , CO and CO_2 . For that reason, the two mechanisms merged *USC mech II* and *USCD NOx v2* have been used in order to study carefully the pollutant emissions.

6.3.3 USC + USCD mechanisms merged

The Figure 6.71 describes the results of the pressure obtained with the new mechanism.

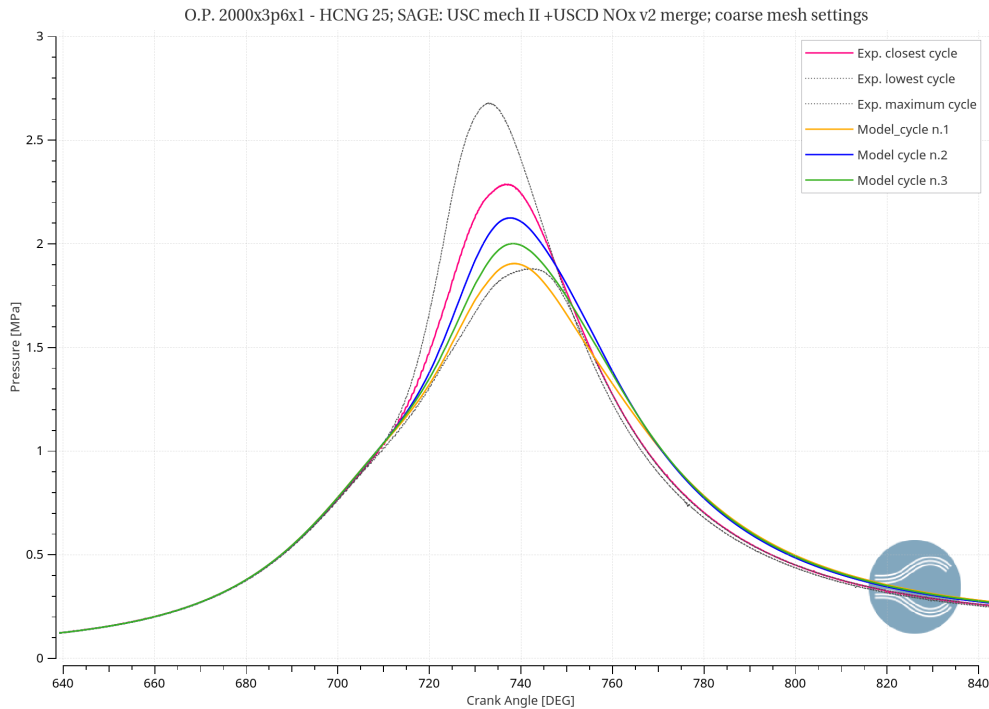


Figure 6.71: Pressure in cylinder 1; *SAGE: USC+USCD mechanisms merged*; coarse mesh settings, HCNG 25

As we can see the best cycle is the number 2: it has been used to compute the representative *HRR* and *AIHR* profiles of the model in order to do a comparison with the case with *USC mech II*.

Unfortunately, as evidenced by figure 6.72, the peak pressure is lower and reaches only 2,12 MPa (7% less than the experimental peak).

The trapped mass is good in fact the error obtained is +1,14%.

The *HRR* in figure 6.73 gets worse as well, in fact the peak of energy is not only lower than the experimental but it is also shifted to the right at 735 CAD instead of 730 CAD. Furthermore, there is still the issue of the excess of energy between 740 CAD and 780 CAD, which means that the combustion is slower in comparison with the real process. Finally, the figure 6.74 demonstrates that no improvements have been achieved for the *AIHR*.

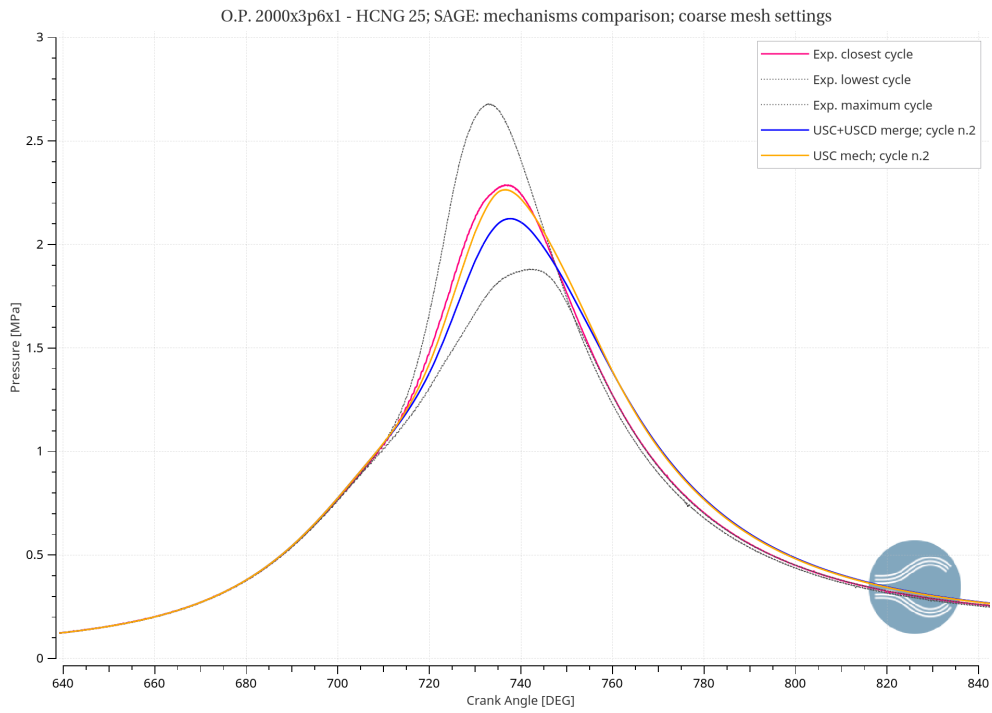


Figure 6.72: Pressure in cylinder 1; *SAGE* mechanisms comparison; coarse mesh settings, HCNG 25

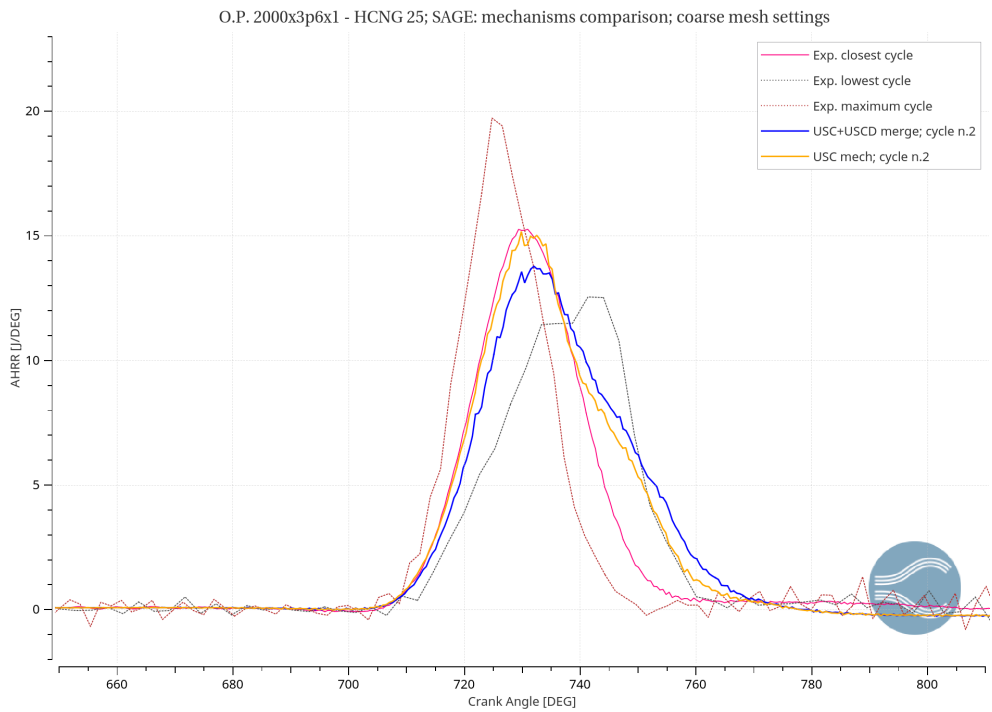


Figure 6.73: Heat release rate; *SAGE* mechanisms comparison; coarse mesh settings, HCNG 25

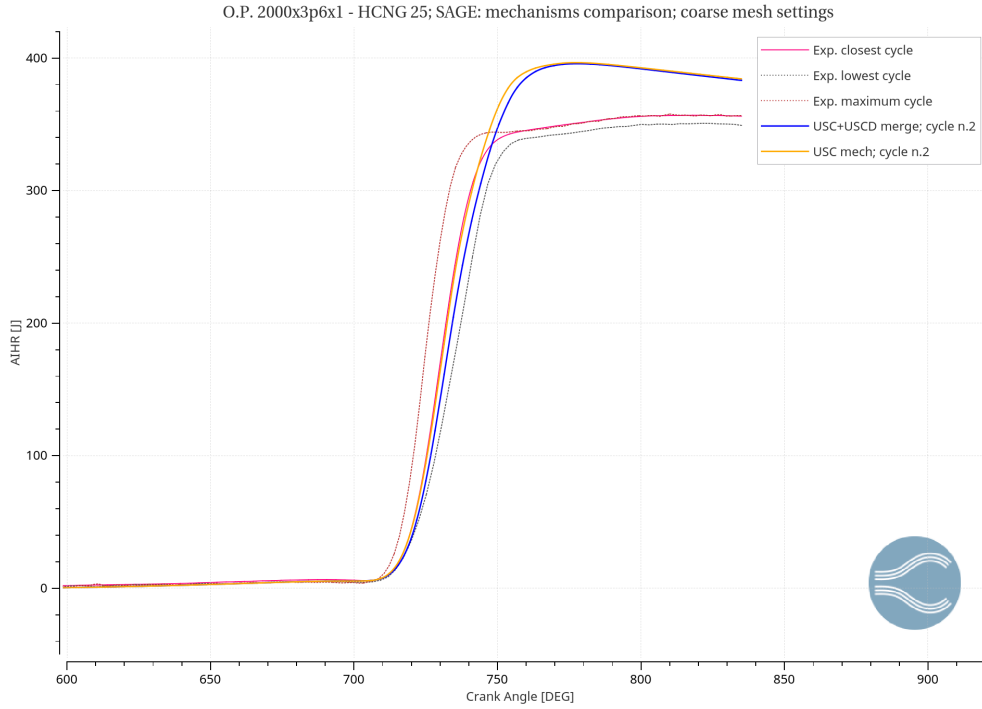


Figure 6.74: Integrated heat release; *SAGE* mechanisms comparison; coarse mesh settings, HCNG 25

The benefit gained with the *USC+USCD* mechanisms merged concerns the emission results. As we can see from the table 25 in fact the main improvement is the reduction of NO_x from +22% to +1%; the other concentrations remain acceptable except for HC where the error is, again, extremely high.

	Exp. value	<i>USC mech II</i>	<i>USC+USCD mechanisms merged</i>
\tilde{x}_{CO}	5650 ppm	5374 ppm	6404 ppm
error		-4,9%	+13,3%
\tilde{x}_{NO_x}	1818 ppm	2228 ppm	1836 ppm
error		+22,5%	+1%
\tilde{x}_{CO_2}	101059 ppm	96755 ppm	95501 ppm
error		-4,3%	-5,5%
\tilde{x}_{HC}	281 ppm	25,65 ppm	53 ppm
error		-90,9%	-81,2%

Table 25: Pollutant emissions results; Mechanisms comparison; coarse mesh settings, HCNG 25

To sum up, the two mechanisms merged do not provide better results in terms of pressure, *HRR* and *AIHR* but they are very important for the analysis of the emissions. The next steps are trying to reduce the error of the pressure profile (for the peak pressure and for the expansion phase) and of the HC concentration.

6.3.4 Boundary conditions manipulation

In the last results the peak pressure obtained for the best cycle is lower than the peak reached by the experimental closest cycle. A strategy to improve the pressure of the cycle is to increase the boundary intake pressure. Thus, the excel file with the experimental data has been modified and the intake pressure has been raised by 6.6%; since the pressure boundary conditions were computed by a MatLab script instead of direct measurements, this approximation can be considered acceptable.

As it is noticeable from figure 6.75, in this way not only the peak pressure increases (until 2,26 MPa with a peak magnitude error of +0,1%) but the pressure in the expansion range is now closer to the experimental profile.

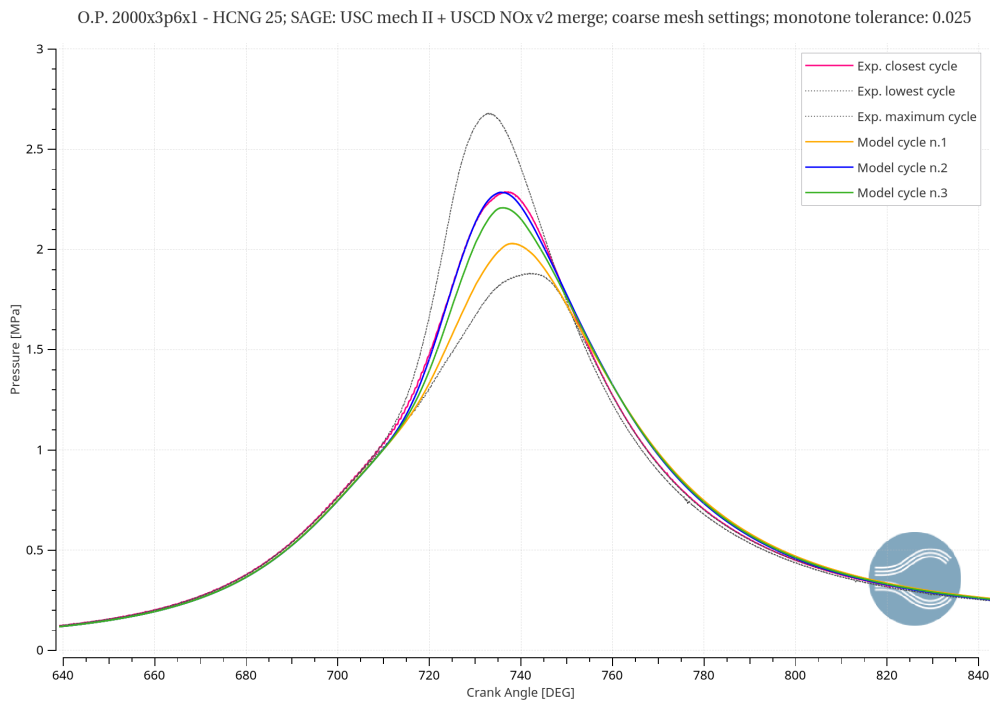


Figure 6.75: Pressure in cylinder 1; *SAGE: USC+USCD mechanisms merged*; coarse mesh settings, HCNG 25

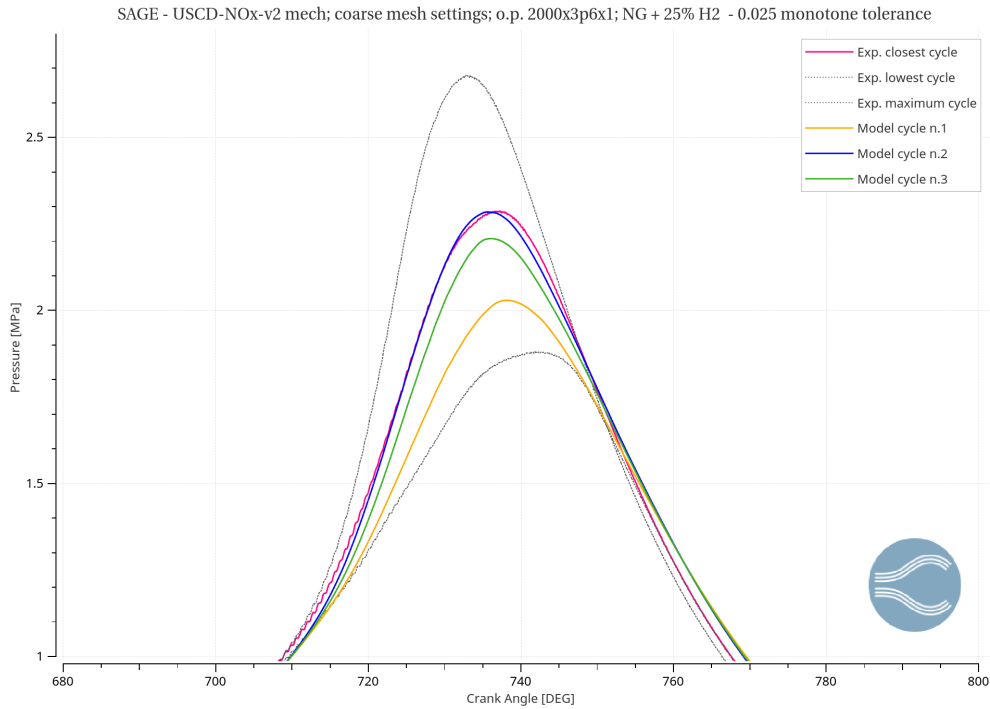


Figure 6.76: Zoom: Pressure in cylinder 1; *SAGE*: *USC+USCD mechanisms merged*; coarse mesh settings, HCNG 25

The reduction of the error for the pressure allows to improve the *HRR* profile, as shown in Figure 6.77. Now, the peak of energy is almost the same of the experimental cycle, but mostly the excess of energy between 740 CAD and 780 CAD shrank. However, the *AIHR* in Figure 6.78 shows that the combustion of the simulation is still slower than the real one and it ends at almost 755 CAD instead of 745 CAD.

With regards to the emission results, the table 27 describes the effect of the boundary conditions manipulation on the different concentration. Since the pressure is now raised, the NO_x concentration increases from 1836 ppm to 2101 ppm (+15%), while CO , CO_2 and HC remains quite constant.

As final verification the monotone tolerance (previously changed from $1e-5$ to 0,025) is now modified again to $1e-5$ to check if \tilde{x}_{NO_x} decreases to a more accurate value.

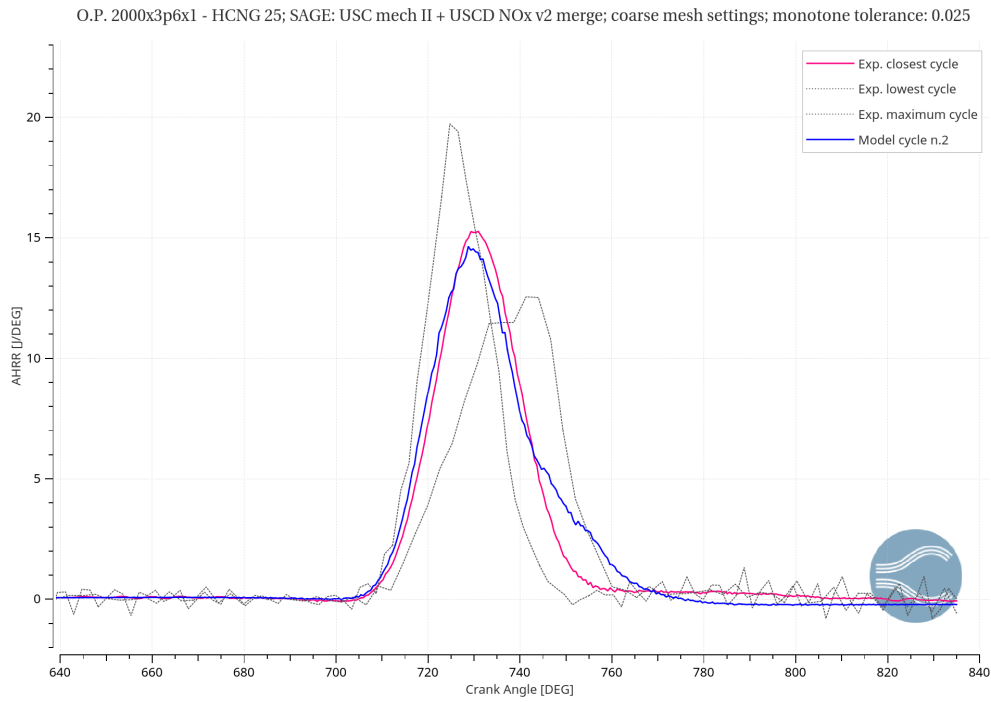


Figure 6.77: Heat release rate; *SAGE: USC+USCD mechanisms merged*; coarse mesh settings, HCNG 25

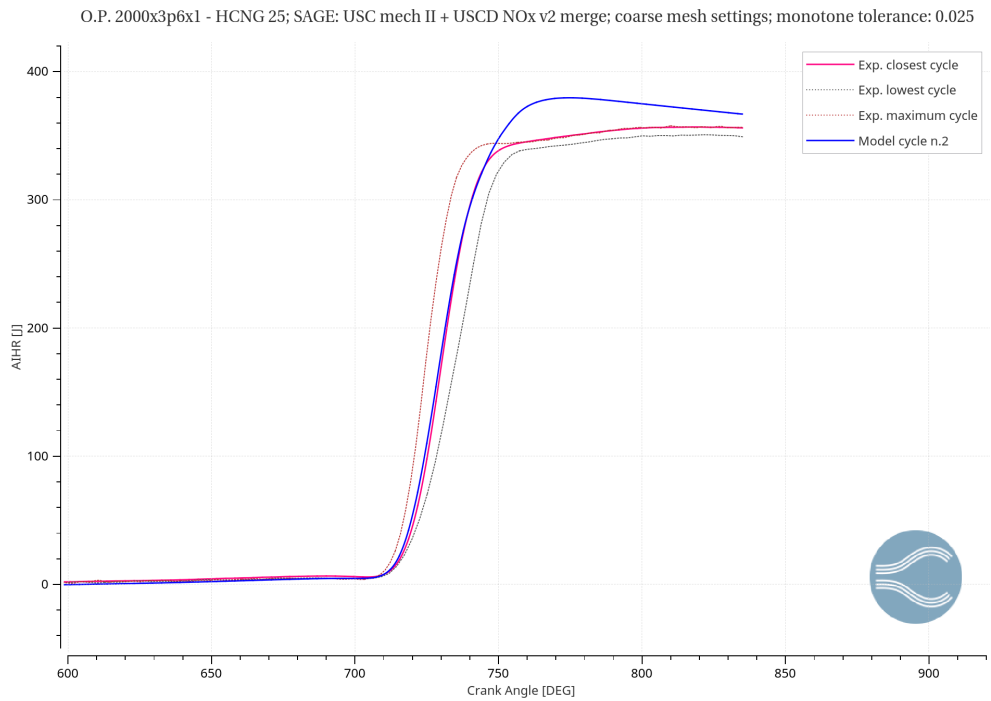


Figure 6.78: Integrated heat release; *SAGE: USC+USCD mechanisms merged*; coarse mesh settings, HCNG 25

	Experimental value [ppm]	Simulation result [ppm]	Error
\tilde{x}_{CO}	5650	6302	+11,5%
\tilde{x}_{NO_x}	1818	2101	+15,5%
\tilde{x}_{CO_2}	101059	92258	-8,7%
\tilde{x}_{HC}	281	76	-72,9%

Table 26: Pollutant emissions; *SAGE: USC+USCD mechanisms merged*; coarse mesh settings, HCNG 25

As we can see from the figure 6.79, 6.80 and 6.81 there are no important differences between the two best cycles of each case in terms of pressure, *HRR* and *AIHR*.

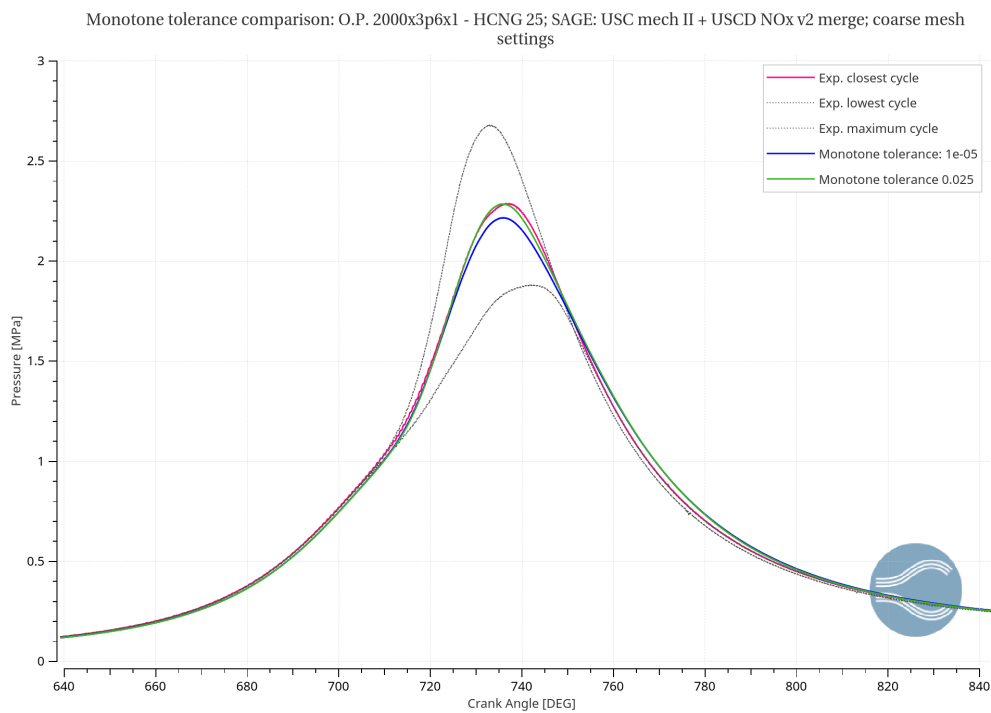


Figure 6.79: Pressure in cylinder 1; *SAGE: USC+USCD mechanisms merged*; monotone tolerance comparison; coarse mesh settings, HCNG 25

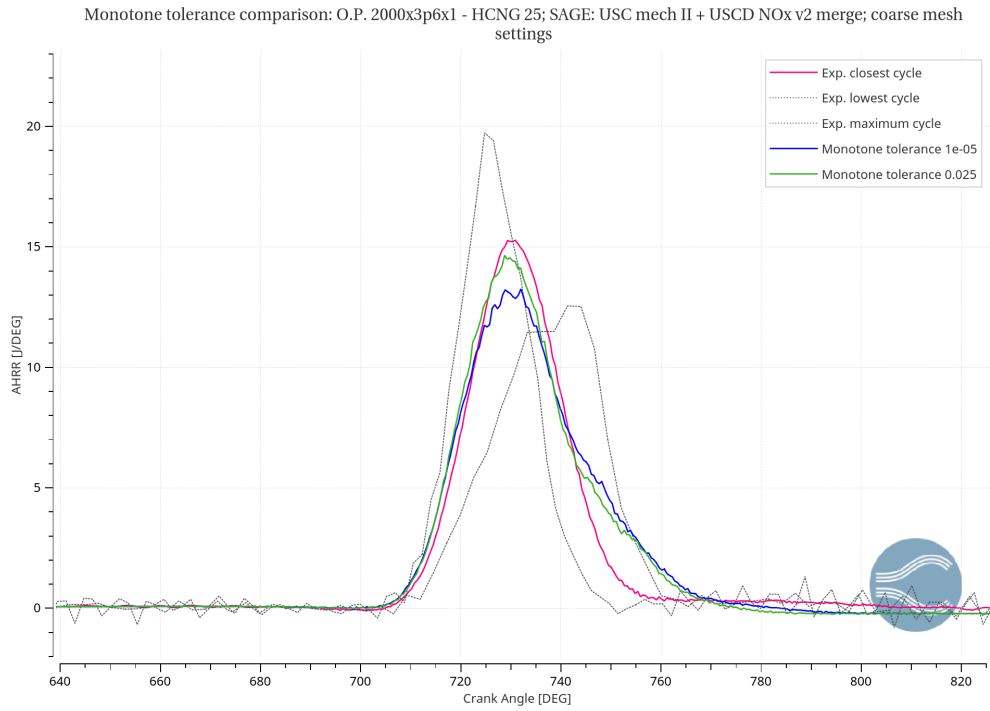


Figure 6.80: Heat release rate; *SAGE: USC+USCD mechanisms merged*; monotone tolerance comparison; coarse mesh settings, HCNG 25

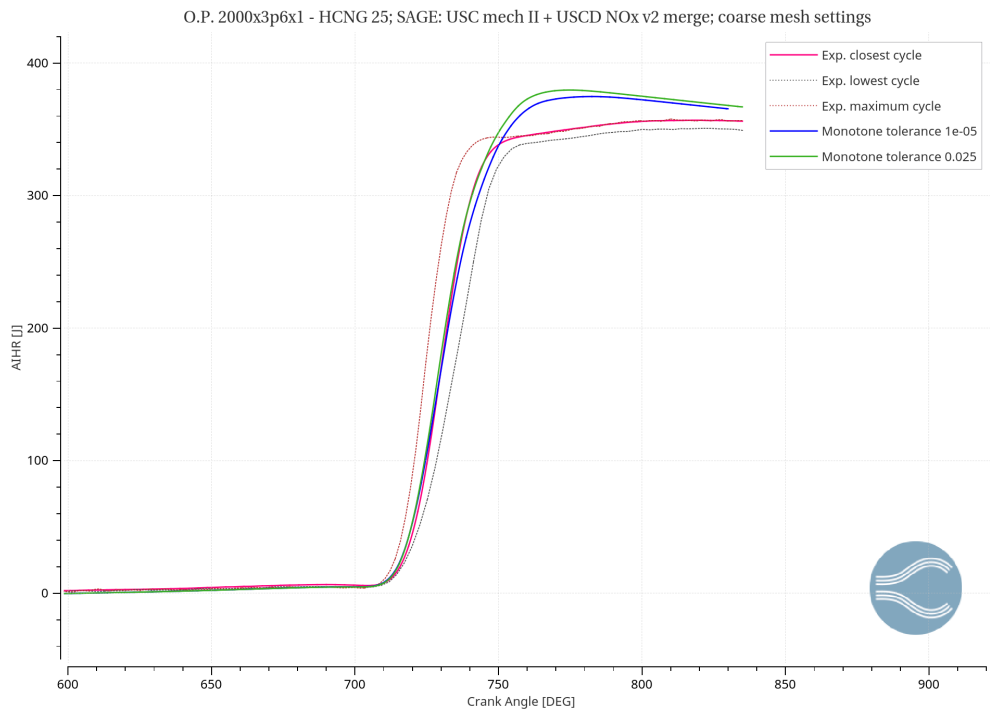


Figure 6.81: Integrated heat release; *SAGE: USC+USCD mechanisms merged*; monotone tolerance comparison; coarse mesh settings, HCNG 25

Finally, the table 27 sums up the errors obtained for both cases on pressure, trapped mass and emissions:

	Exp. value	Mon. tol. 0,025	Mon. tol. 1e-05
Peak pressure error	2,286 [bar]	+0,11%	+3%
Trapped mass error	$1,84 \times 10^{-4}$ [kg]	-1,97%	-1,58%
\tilde{x}_{CO} error	5650 ppm	6302 ppm +11,5%	6330 ppm +12%
\tilde{x}_{NO_x} error	1818 ppm	2101 ppm +15,5%	1914 ppm +5,3%
\tilde{x}_{CO_2} error	101059 ppm	92258 ppm -8,7%	95540 ppm -5,5%
\tilde{x}_{HC} error	281 ppm	68,6 ppm -75,7%	69,3 ppm -75,4%

Table 27: Results overview; *SAGE: USC+USCD mechanisms merged*; monotone tolerance comparison; coarse mesh settings, HCNG 25

The best compromise turns out to be the model with monotone tolerance 1e-05: in fact, although the peak pressure error increases by 3%, in this second case it is possible to gain an error reduction of almost 10% and 3% for \tilde{x}_{NO_x} and \tilde{x}_{CO_2} respectively.

The final step is trying to reduce the high error of the hydrocarbons. As done for the case with HCNG-15 (see chapter 6.2.7), the same *SMALL crevice volume* (height of the crevice of 2,1mm) has been added to this specific case setup.

6.3.5 Crevice Volume

The addition of the crevices to the geometry allows to obtain the following results:

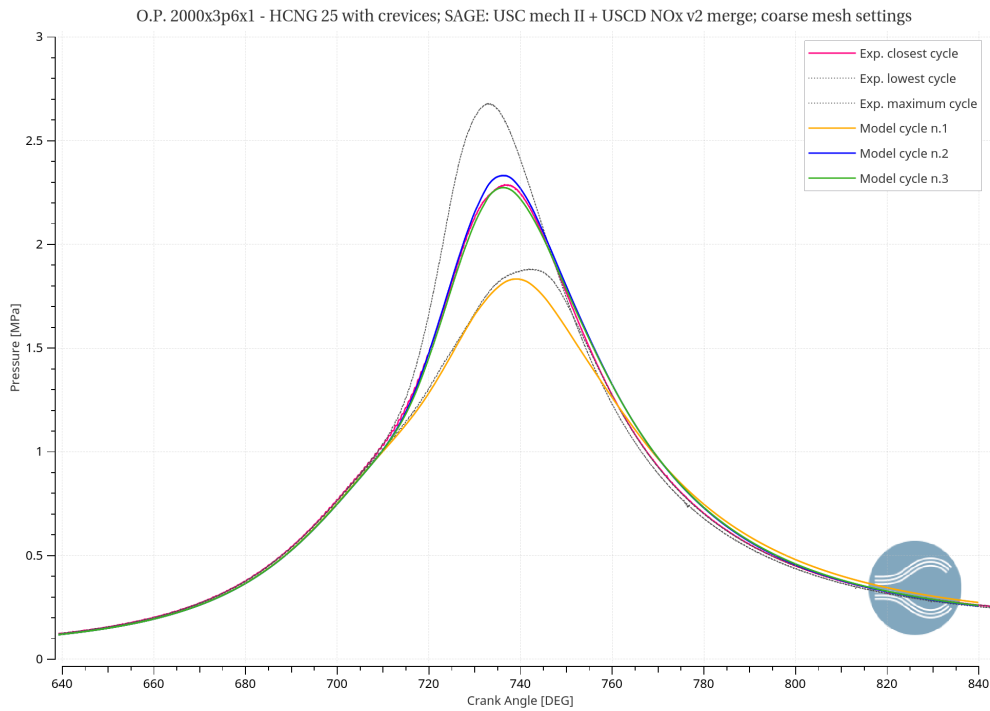


Figure 6.82: Pressure in cylinder 1; *SAGE: USC+USCD mechanisms merged*; small crevice volume; coarse mesh settings, HCNG 25

The best cycle is the model cycle number 3 which is very close to the experimental closest cycle, in fact it reaches the peak pressure of 2,26 MPa (0,6% less than the real value of 2,28 MPa).

So, if we compare this cycle with the best cycle of the case without crevices (Figure 6.83), we can see that a reduction of the peak pressure error of 3% has been gained.

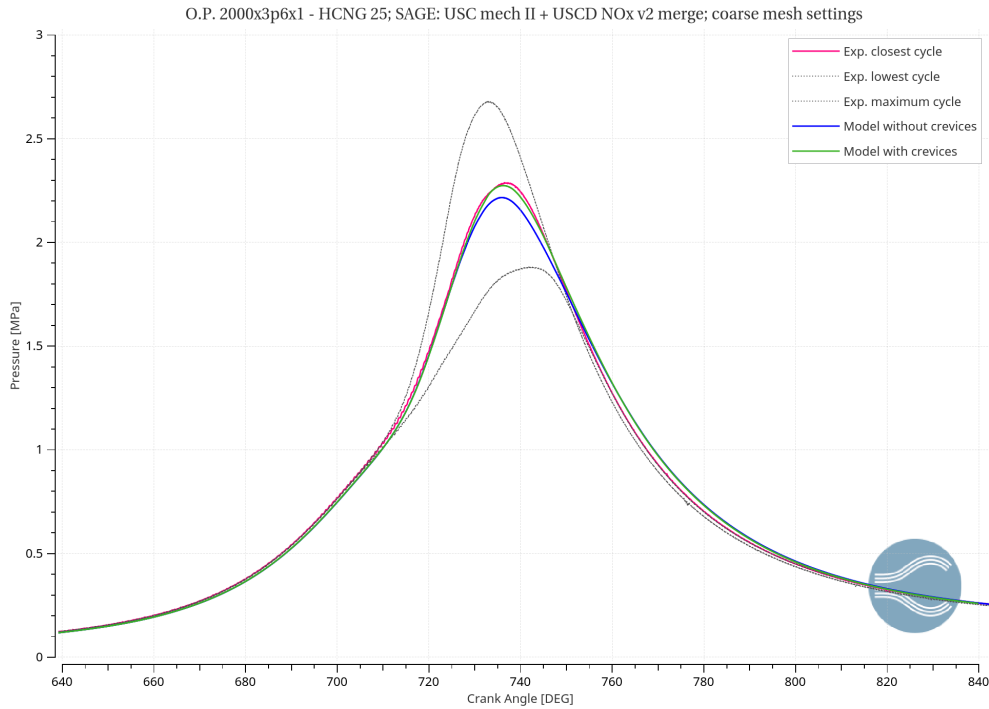


Figure 6.83: Pressure in cylinder 1; *SAGE: USC+USCD mechanisms merged*; coarse mesh settings, HCNG 25

The *HRR* profile presents notable improvements: from figure 6.84 and from the comparison in figure 6.85 it is clear that the peak of energy obtained adding the crevice volume, which is 6% lower than the experimental peak, is better in comparison with the previous case where the error is 13% on the peak magnitude. Furthermore, also the slope of the curve in the expansion phase is different and the excess of energy in this range is smaller.

The improvement of the heat release rate has a beneficial effect on *AIHR*: from figures 6.86 and 6.87 in fact we can see that the slope of the curve between 720 CAD and 750 CAD is very good and it follows very well the experimental profile. Unfortunately, there is still a high peak of energy (after 750 CAD) and thus the combustion of the simulation is still slower than the real one; further developments will have to be made.

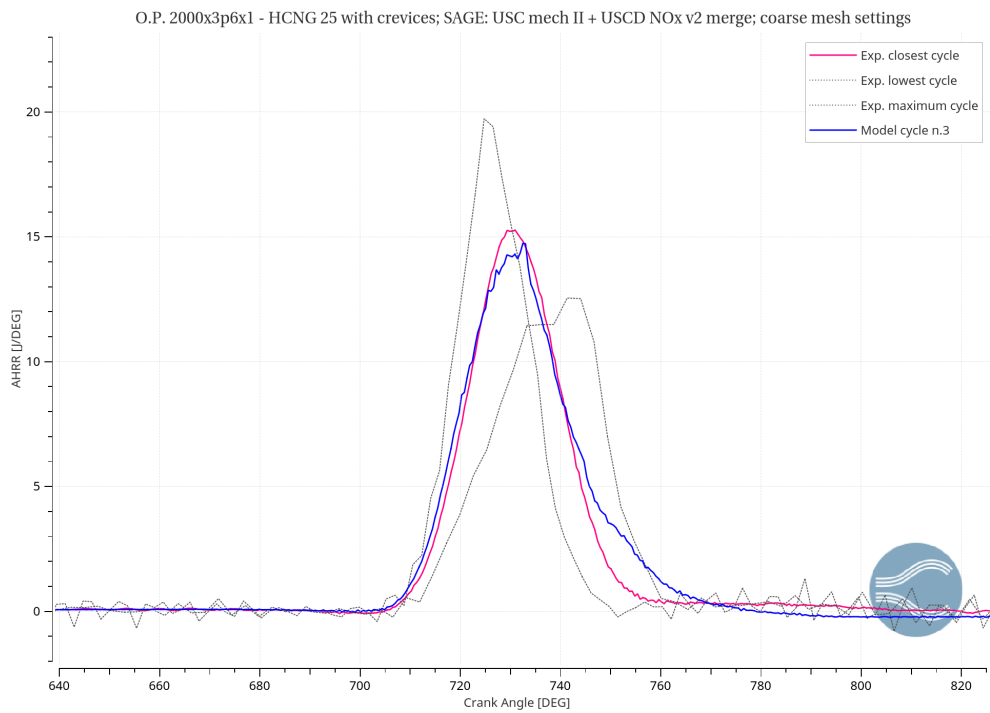


Figure 6.84: Heat release rate; *SAGE: USC+USCD mechanisms merged*; small crevice volume; coarse mesh settings, HCNG 25

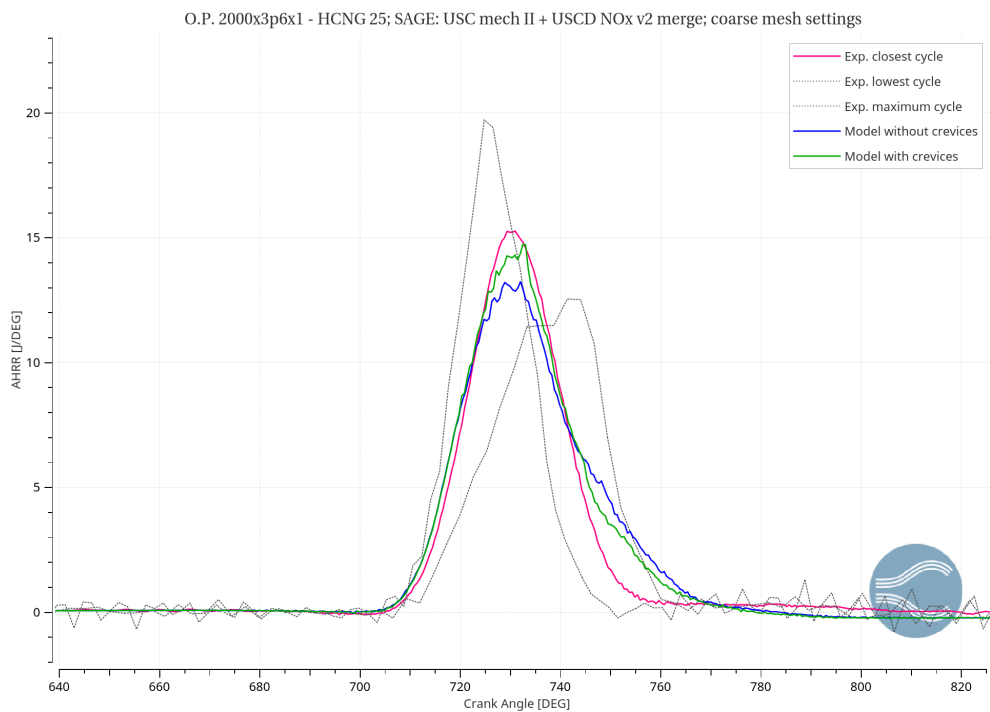


Figure 6.85: Heat release rate; *SAGE: USC+USCD mechanisms merged*; coarse mesh settings, HCNG 25

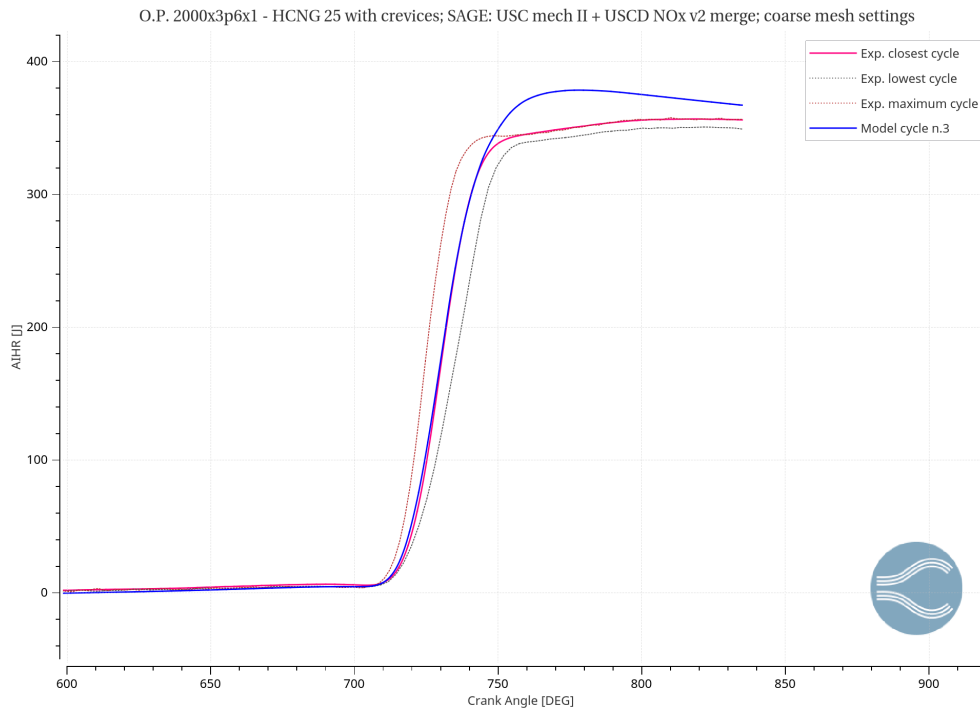


Figure 6.86: Integrated heat release; *SAGE: USC+USCD mechanisms merged*; small crevice volume; coarse mesh settings, HCNG 25

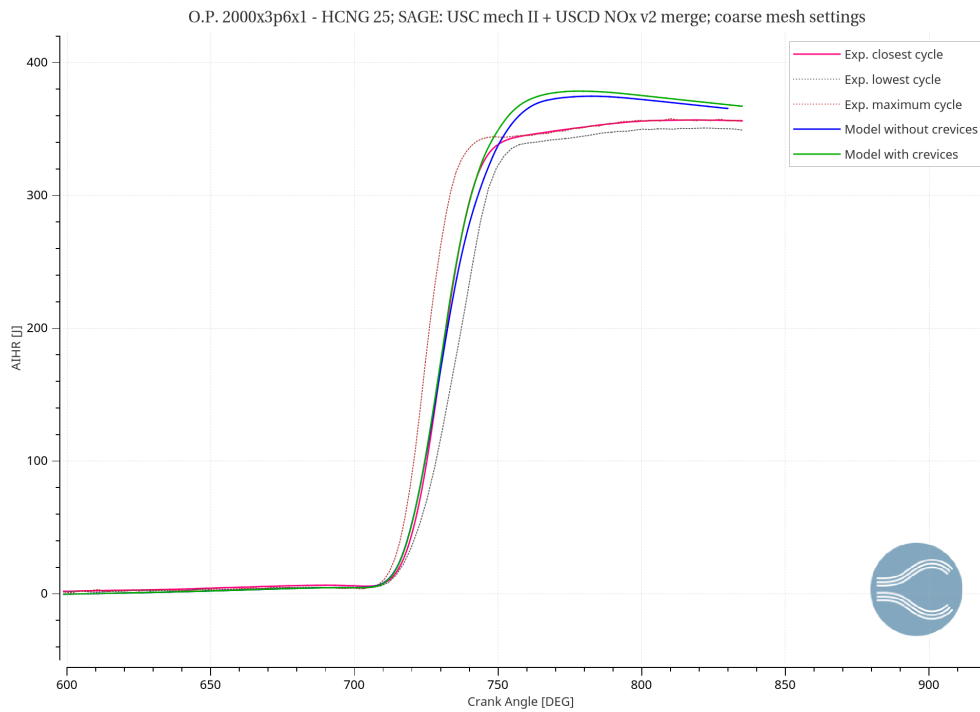


Figure 6.87: Integrated heat release; *SAGE: USC+USCD mechanisms merged*; coarse mesh settings, HCNG 25

The trapped mass error is -1,6% which means that the model mass into the chamber is slightly less than the real one.

Concerning the emission results, the table 28 compares the different values obtained by using a geometry with and without the small crevice volume.

	Exp. value	No crevices	Small crevice volume
\tilde{x}_{CO} error	5650 ppm	6330 ppm +12%	6522 ppm +15%
\tilde{x}_{NO_x} error	1818 ppm	1914 ppm +5,3%	2224 ppm +22%
\tilde{x}_{CO_2} error	101059 ppm	95540 ppm -5,5%	95044 ppm -6%
\tilde{x}_{HC} error	281 ppm	69,3 ppm -75,4%	89,6 ppm -68%

Table 28: Results overview; *SAGE: USC+USCD mechanisms merged*; effect of the crevices; coarse mesh settings, HCNG 25

Unlike the case with 15% of H₂, unfortunately the addition of the same volume of the crevices does not provide a sufficient increase of the hydrocarbons. Furthermore, also the others concentrations become worse in particular \tilde{x}_{NO_x} which raises from 1914 ppm to 2224 ppm with an error of +22% instead of 5,3%. For that reason, the crevice volume should be enlarged and, although the hydrocarbons formation is very sensitive to the size of the volume, a compromise solution with the case of HCNG 15 fuel should be found.

In order to better understand why there is a great difference of the HC formation by using the two different fuels, an analysis inside the cylinder during the combustion process might be useful. First of all, the flame propagation differs from case to case: as the Figure 6.88 shows, the case with HCNG 15 shows a slight flame quenching phenomena at 735 CAD. Conversely, in the case with HCNG 25 the combustion is better and no flame quenching is obtain close to the walls. Furthermore, the speed of combustion is faster with 25% of H₂, in fact at 750 CAD we can see the different propagation of the flame into the combustion chamber. However, the combustion simulated with HCNG 25 is so quick that it does not represents the real process, which has some “imperfections” (e.g. flame quenching) and it is better simulated by the HCNG 15 model.

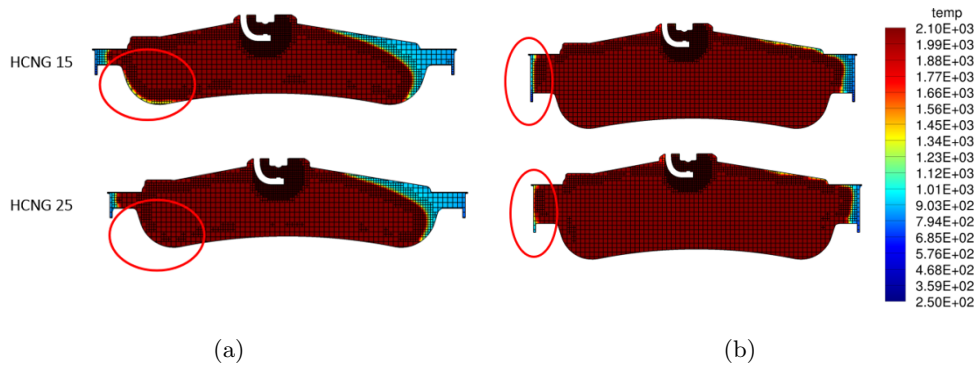


Figure 6.88: Temperature comparison (a) 735 CAD ; (b) 750 CAD

The two different models give two concentrations \tilde{x}_{HC} , which differs by one order of magnitude. The figures 6.89 6.90 and 6.91 highlight the influence of the same crevice volume on the location and mass fraction of CH_4 (the main component of the fuel) and so on the HC production. As we can see, the majority of the unburned CH_4 is located around the valves and between cylinder wall and piston: here, there is a great difference of mass fraction between HCNG 15 and the case with HCNG 25, where the hydrocarbons are underestimated.

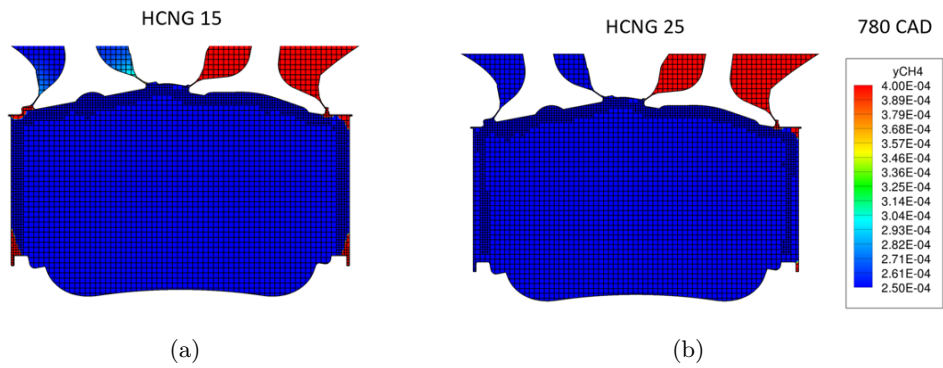


Figure 6.89: CH_4 mass fraction comparison at 780 CAD (a) HCNG 15 ; (b) HCNG 25

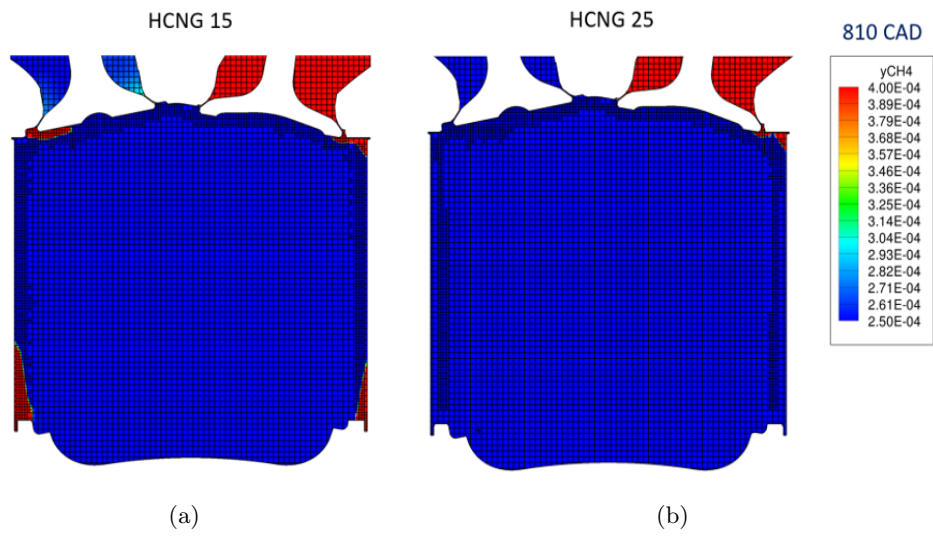


Figure 6.90: CH₄ mass fraction comparison at 810 CAD (a) HCNG 15 ; (b) HCNG 25

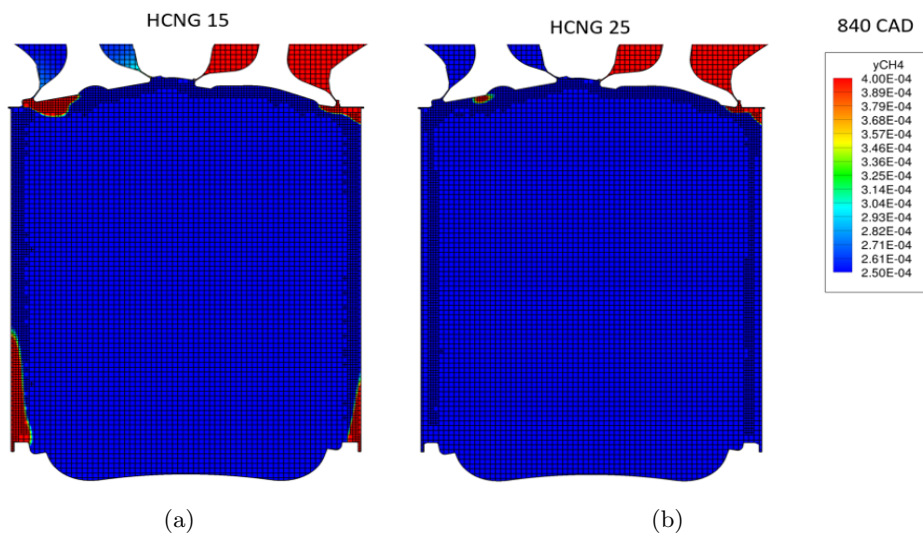


Figure 6.91: CH₄ mass fraction comparison at 850 CAD (a) HCNG 15 ; (b) HCNG 25

Finally, the hydrocarbons produced in the whole cylinder are shown in figures 6.92, 6.93 and 6.94 as 3D plot.

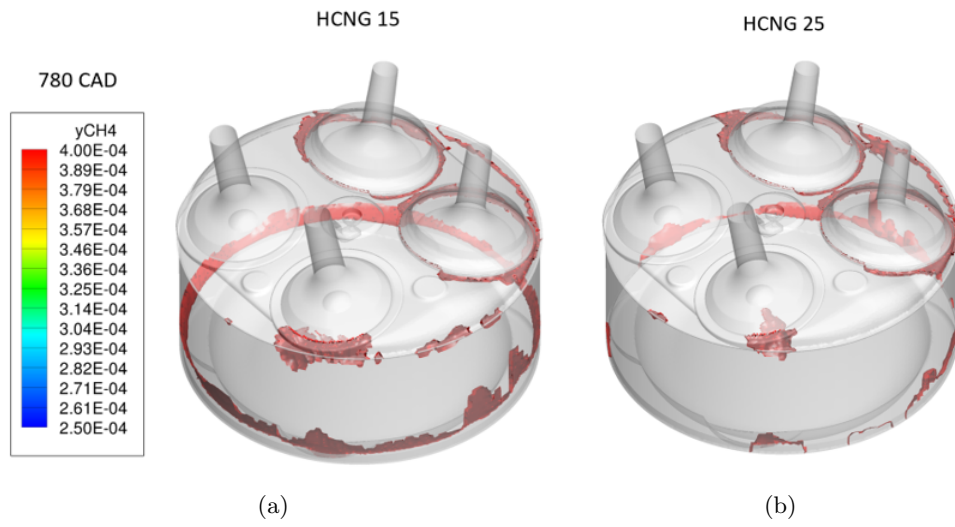


Figure 6.92: CH₄ mass fraction in cylinder at 780 CAD (a) HCNG 15 ; (b) HCNG 25

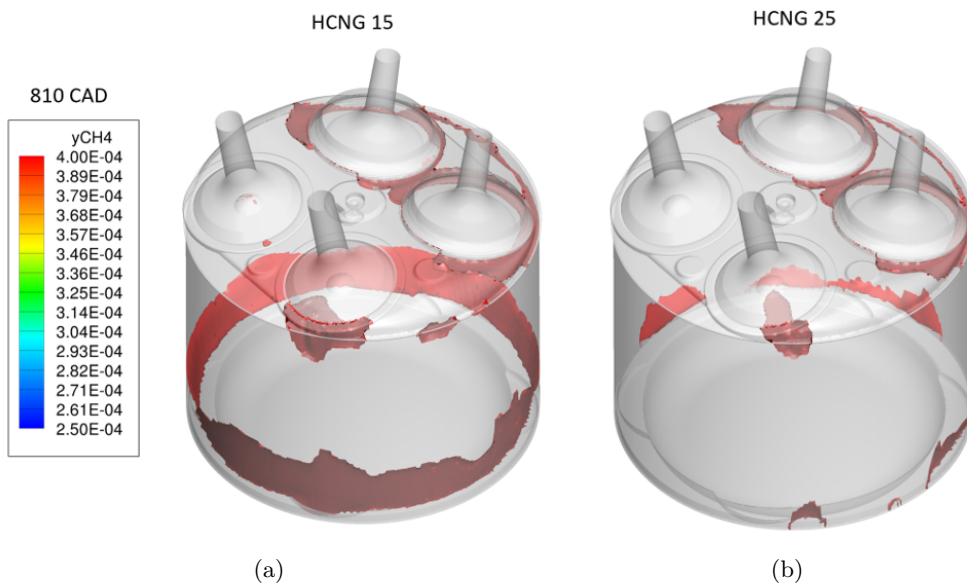


Figure 6.93: CH₄ mass fraction in cylinder at 810 CAD (a) HCNG 15 ; (b) HCNG 25

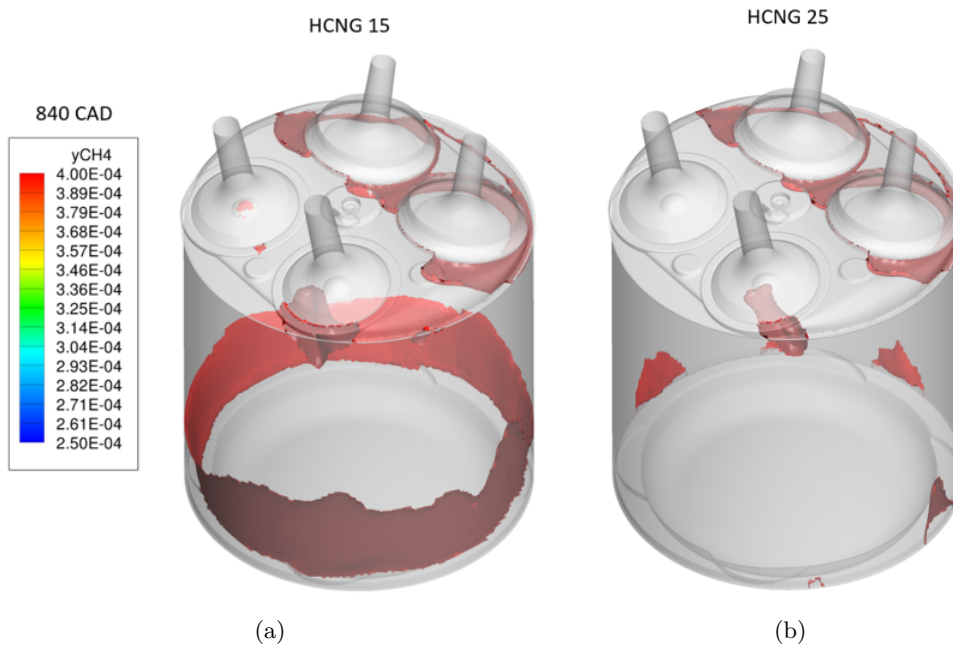


Figure 6.94: CH_4 mass fraction in cylinder at 840 CAD (a) HCNG 15 ; (b) HCNG 25

In conclusion, the case setup which best simulates the operating point $2000[\text{rpm}] \times 3.6 [\text{bar}] \times \lambda=1$ with HCNG 25 is obtained by using the *SAGE* model and the *USC+USCD* mechanisms merged with a *coarse* mesh, the default value of $Sc = 0,78$ and $1e-05$ as monotone tolerance.

However, while the small crevice volume provides good results in terms of emissions for the case with HCNG 15, the addition of the same volume to the model with HCNG 25 does not provide the same results and the value of \tilde{x}_{HC} is still far from the experimental measurements. For that reason, further developments like the combined effect of the crevices and the reduction of the wall temperature or the modeling of the blow-by phenomenon might give better results in terms of pollutant emissions, in particular for the unburned hydrocarbons.

7 Conclusions and Future Developments

This thesis work gave me the opportunity to familiarize with the CFD simulations and in particular with CONVERGE CFD software, which is a strong tool able to simulate the combustion process of the internal combustion engines, in different conditions.

The work has been developed in collaboration with Politecnico di Torino and the European project *Gas-On*, whose aim is to reduce the emissions of engines and to realize a sustainable mobility in Europe. Thus, the study of fuel mixture with hydrogen might be a way to achieve this target.

The analysis proposed in this thesis is focused on one operating point, 2000[rpm] x 3.6 [bar] x lambda=1, with two different fuel compositions: natural gas + 15% of H₂, HCNG 15 and natural gas + 25% of H₂, HCNG 25. Several issues have been found during the model validation and different changes have been made, for example choice of others reaction mechanisms, variation of the Schmidt Number or monotone tolerance, LHV correction and addition of the crevices.

For what concerns the case with HCNG 15 as fuel, the first mechanism *GRI Mech 3.0* did not provide good results; thus, the *USC mech II* and *USCD NOx v2* mechanisms have been used in order to improve the pressure profile, the *HRR* and *AIHR*, but mostly the emission results. A fundamental parameter which can affect the pressure and the emissions, in particular NO_x, is the Schmidt Number: a sensitivity of the model has been carried out, after which the value of 0,75 has been chosen instead of the default value of 0,78. Since none of these changes has led to an improvement of the HC concentration, three strategies have been tried to increase the unburned hydrocarbons: the reduction of the cylinder wall temperature, the LHV correction and the addition of the crevices to the surface. The first two strategies did not provide enough improvements, but the addition of the crevice volume (between piston and cylinder) has allowed to obtain an error of 15% on the HC concentration.

Considering the case with HCNG 25, more or less the same problems of pressure and heat release rate of the previous case have been found. The same mechanisms has been used, which is the *USC+USCD mechanisms merged*, because the *GRI Mech 3.0* gave overestimated results. In addition, some adjustments through the monotone tolerance has been made but, finally, the best value has proved to be the default value of 1e-05. Finally, in order to reduce the error of the unburned hydrocarbons, the same crevice volume of the case with HCNG 15 has been added to the surface. Unfortunately, in this case the increase of the HC concentration is not enough to reach the experimental value. After the post-processing, in fact, it is possible to note how the combustion process differs from HCNG 15 to the HCNG 25 fuel, where in this last case the phenomenon does not presents imperfections, like flame quenching, and it produces less hydrocarbons.

To sum up, the following table gives an overview of the influence of the parameters considered in this work on the peak pressure and the pollutant emissions:

	Peak pressure	CO	NO_x	CO₂	HC
<i>USC mech II</i>	Lower	↓↓	↑↑	↑	-
<i>USC+USCD merged</i>	Slightly lower	↑↑	↓↓	-	-
<i>Schmidt Number</i>	$p \propto \frac{1}{Sc}$	-	$\tilde{x}_{NO_x} \propto \frac{1}{Sc}$	-	-
<i>Monotone tolerance</i>	Whit 0,025 the peak pressure slightly increases	-	Whit 0,025: \tilde{x}_{NO_x} slightly increases	Whit 0,025: \tilde{x}_{CO_2} slightly decreases	-
<i>Reduction of T_{wall}</i>	-	-	↓	-	↑
<i>Crevice volume</i>	-	-	-	-	↑↑↑

Table 29: Results overview

In order to reach a more accurate value for the pollutant emissions, future developments are needed. A good idea might be to add the effect of the reduction of the cylinder wall temperature to the crevice volume, or to use a proper “crevice model” and a blow-by model; in this way, the effect of the crevices (a fundamental source for the HCs) will be simulate as well as possible. Furthermore, an interesting idea might be also to validate others operating points (e.g. with high load and rpm), in order to check the engine behavior in different conditions.

The analysis of the combustion in CNG/HCNG engines through CFD simulations, might be a strong tool able to better understand how to improve the performance and the efficiency of the powertrain systems. The use of alternative fuels, in fact, is very important for the pollutant emission reduction and can lead the world towards a green and environmental friendly transport system .

List of Figures

1.1	Surface forces in the x -direction exerted on the fluid element . . .	5
1.2	(a) nozzle embedding; (b) fixed embedding around a valve . . .	10
1.3	AMR through the valves	11
2.1	Comparison of properties of Hydrogen, CNG and HCNG5 with Gasoline	13
2.2	Properties of CNG and HCNG blends with different hydrogen content	13
3.1	Engine and test bench under construction	16
3.2	Throttle body: (a) wire control of throttle opening ; (b) frontal view of butterfly valve	18
3.3	(a) Turbocharger ; (b) Intercooler air-water	18
3.4	(a) <i>Tartarini</i> pressure regulator; (b) High pressure sensor <i>Kelle Pa 22 M</i> ; (c) Low pressure sensor <i>Kavlico P4000</i>	19
3.5	Gas feeding rail	19
3.6	Lambda-sensor characteristic	21
3.7	Dynamo-meter FE 260-S <i>Borghini and Savieri</i>	22
3.8	Experimental layout	23
3.9	Experimental data plot: Pressure in cylinder 1; 2000x3.6x1; HCNG 15	28
3.10	Experimental data plot: zoom around peak pressure in cylinder 1; 2000x3.6x1; HCNG 15	29
3.11	Experimental data plot: Pressure in cylinder 1; 2000x3.6x1; HCNG 25	30
3.12	Experimental data plot: Pressure in cylinder 1; 2000x3.6x1; HCNG 25	30
4.1	Engine CAD geometry: isometric view	31
4.2	Engine CAD geometry: focus on valves and spark plug	32
4.3	Regions	33
4.4	Boundaries	34
4.5	schematic representations of the Boundary and Initial condition	36
4.6	Source models	40
4.7	(a) source model on the geometry; (b) additional fixed embedding	41
5.1	<i>GRI Mech 3.0</i> ; <i>mech.dat</i> file	49
5.2	(a) <i>USC mech II</i> ; (b) <i>USCD NOx v2</i>	50
6.1	Pressure in cylinder 1; <i>SAGE-GRI Mech 3.0</i> and experimental data; coarse mesh settings, HCNG 15	54
6.2	Pressure in cylinder 1 - Zoom; <i>SAGE-GRI Mech 3.0</i> and experimental data; coarse mesh settings, HCNG 15	54
6.3	Pressure in cylinder 1 - Compression phase; <i>SAGE-GRI Mech 3.0</i> and experimental data; coarse mesh settings, HCNG 15	55
6.4	Heat release rate; <i>SAGE-GRI Mech 3.0</i> and experimental data; coarse mesh settings, HCNG 15	56
6.5	Integrated heat release rate; <i>SAGE-GRI Mech 3.0</i> and experimental data; coarse mesh settings, HCNG 15	56

6.6	Pressure in cylinder 1; <i>SAGE-USC mech II</i> and experimental data; coarse mesh settings, HCNG 15	58
6.7	Heat release rate; <i>SAGE-USC mech II</i> and experimental data; coarse mesh settings, HCNG 15	58
6.8	Integrated heat release rate; <i>SAGE-USC mech II</i> and experimental data; coarse mesh settings, HCNG 15	59
6.9	Pressure in cylinder 1; <i>SAGE - USC+USCD mechanisms merged</i> and experimental data; coarse mesh settings, HCNG 15	61
6.10	Heat release rate; <i>SAGE - USC+USCD mechanisms merged</i> and experimental data; coarse mesh settings, HCNG 15	62
6.11	Integrated heat release; <i>SAGE - USC+USCD mechanisms merged</i> and experimental data; coarse mesh settings, HCNG 15	62
6.12	Pressure in cylinder 1; comparison between <i>USC mech II</i> and <i>USC+USCD mechanisms merged</i> ; coarse mesh settings, HCNG 15	63
6.13	Heat release rate; comparison between <i>USC mech II</i> and <i>USC+USCD mechanisms merged</i> ; coarse mesh settings, HCNG 15	64
6.14	Integrated heat release rate; comparison between <i>USC mech II</i> and <i>USC+USCD mechanisms merged</i> ; coarse mesh settings, HCNG 15	64
6.15	Pressure in cylinder 1; <i>SAGE: USC+USCD mechanisms merged</i> ; Schmidt Number = 0,765; coarse mesh settings, HCNG 15	67
6.16	Heat release rate; <i>SAGE: USC+USCD mechanisms merged</i> ; Schmidt Number = 0,765; coarse mesh settings, HCNG 15	67
6.17	Integrated heat release; <i>SAGE: USC+USCD mechanisms merged</i> ; Schmidt Number = 0,765; coarse mesh settings, HCNG 15	68
6.18	Pressure in cylinder 1; <i>SAGE: USC+USCD mechanisms merged</i> ; Schmidt Number = 0,75; coarse mesh settings, HCNG 15	69
6.19	Heat release rate; <i>SAGE: USC+USCD mechanisms merged</i> ; Schmidt Number = 0,75; coarse mesh settings, HCNG 15	69
6.20	Heat release rate; <i>SAGE: USC+USCD mechanisms merged</i> ; Schmidt Number = 0,75; coarse mesh settings, HCNG 15	70
6.21	Pressure in cylinder 1; <i>SAGE: USC+USCD mechanisms merged</i> ; Schmidt Number sensitivity; coarse mesh settings, HCNG 15	71
6.22	Pressure in cylinder 1 - zoom; <i>SAGE: USC+USCD mechanisms merged</i> ; Schmidt Number sensitivity; coarse mesh settings, HCNG 15	72
6.23	Heat release rate; <i>SAGE: USC+USCD mechanisms merged</i> ; Schmidt Number sensitivity; coarse mesh settings, HCNG 15	73
6.24	Heat release rate; <i>SAGE: USC+USCD mechanisms merged</i> ; Schmidt Number sensitivity; coarse mesh settings, HCNG 15	73
6.25	Comparison of mass fraction of CH ₄ with two different values of Schmidt Number	74
6.26	Comparison of mass fraction of CO with two different values of Schmidt Number	75
6.27	Pressure in cylinder 1; Temperature of the wall reduced by 30 K; <i>SAGE: USC+USCD mechanisms merged</i> ; coarse mesh settings, HCNG 15	76

6.28	Heat release rate; Temperature of the wall reduced by 30 K; <i>SAGE: USC+USCD mechanisms merged</i> ; coarse mesh settings, HCNG 15 . . .	77
6.29	Integrated heat release; Temperature of the wall reduced by 30 K; <i>SAGE: USC+USCD mechanisms merged</i> ; coarse mesh settings, HCNG 15 . . .	78
6.30	Pressure in cylinder 1; Temperature of the wall reduced by 50 K; <i>SAGE: USC+USCD mechanisms merged</i> ; coarse mesh settings, HCNG 15 . . .	79
6.31	Heat release rate; Temperature of the wall reduced by 50 K; <i>SAGE: USC+USCD mechanisms merged</i> ; coarse mesh settings, HCNG 15 . . .	79
6.32	Integrated heat release; Temperature of the wall reduced by 50 K; <i>SAGE: USC+USCD mechanisms merged</i> ; coarse mesh settings, HCNG 15 . . .	80
6.33	Pressure in cylinder 1; Temperature of the wall sensitivity; <i>SAGE: USC+USCD mechanisms merged</i> ; coarse mesh settings, HCNG 15 . . .	81
6.34	Heat release rate; Temperature of the wall sensitivity; <i>SAGE: USC+USCD mechanisms merged</i> ; coarse mesh settings, HCNG 15	82
6.35	Integrated heat release; Temperature of the wall sensitivity; <i>SAGE: USC+USCD mechanisms merged</i> ; coarse mesh settings, HCNG 15 . . .	82
6.36	Pressure in cylinder 1; LHV sensitivity; <i>SAGE: USC+USCD mechanisms merged</i> ; coarse mesh settings, HCNG 15	84
6.37	Zoom: Pressure in cylinder 1; LHV sensitivity; <i>SAGE: USC+USCD mechanisms merged</i> ; coarse mesh settings, HCNG 15	85
6.38	Heat release rate; LHV sensitivity; <i>SAGE: USC+USCD mechanisms merged</i> ; coarse mesh settings, HCNG 15	86
6.39	Integrate heat release; LHV sensitivity; <i>SAGE: USC+USCD mechanisms merged</i> ; coarse mesh settings, HCNG 15	86
6.40	(a) 3D picture of the cylinder; (b) section of the cylinder	88
6.41	Height of the crevice volume	88
6.42	Pressure in cylinder 1; crevice volume addition; <i>SAGE: USC+USCD mechanisms merged</i> ; coarse mesh settings, HCNG 15	89
6.43	Zoom: Pressure in cylinder 1; crevice volume addition; <i>SAGE: USC+USCD mechanisms merged</i> ; coarse mesh settings, HCNG 15	90
6.44	Heat release rate; crevice volume addition; <i>SAGE: USC+USCD mechanisms merged</i> ; coarse mesh settings, HCNG 15	91
6.45	Integrated heat release; crevice volume addition; <i>SAGE: USC+USCD mechanisms merged</i> ; coarse mesh settings, HCNG 15	91
6.46	Pressure in cylinder 1; <i>SAGE: USC+USCD mechanisms merged</i> ; coarse mesh settings, HCNG 15	92
6.47	Heat release rate; <i>SAGE: USC+USCD mechanisms merged</i> ; coarse mesh settings, HCNG 15	93
6.48	Heat release rate; <i>SAGE: USC+USCD mechanisms merged</i> ; coarse mesh settings, HCNG 15	93
6.49	(a) <i>High</i> crevice volume; (b) <i>Medium</i> crevice volume; (c) <i>Small</i> crevice volume	94
6.50	Pressure in cylinder 1; <i>Medium</i> crevice volume; <i>SAGE: USC+USCD mechanisms merged</i> ; coarse mesh settings, HCNG 15	95
6.51	Heat release rate; <i>Medium</i> crevice volume; <i>SAGE: USC+USCD mechanisms merged</i> ; coarse mesh settings, HCNG 15	96

6.52	Integrated heat release; <i>Medium</i> crevice volume; <i>SAGE: USC+USCD mechanisms merged</i> ; coarse mesh settings, HCNG 15	96
6.53	Pressure in cylinder 1; <i>Small</i> crevice volume; <i>SAGE: USC+USCD mechanisms merged</i> ; coarse mesh settings, HCNG 15	97
6.54	Heat release rate; <i>Small</i> crevice volume; <i>SAGE: USC+USCD mechanisms merged</i> ; coarse mesh settings, HCNG 15	98
6.55	Integrated heat release; <i>Small</i> crevice volume; <i>SAGE: USC+USCD mechanisms merged</i> ; coarse mesh settings, HCNG 15	98
6.56	Pressure in cylinder 1; Crevice volume comparison; <i>SAGE: USC+USCD mechanisms merged</i> ; coarse mesh settings, HCNG 15	99
6.57	Heat release rate; Crevice volume comparison; <i>SAGE: USC+USCD mechanisms merged</i> ; coarse mesh settings, HCNG 15	100
6.58	Integrated heat release; Crevice volume comparison; <i>SAGE: USC+USCD mechanisms merged</i> ; coarse mesh settings, HCNG 15	101
6.59	Pressure in cylinder 1; <i>SAGE: GRI Mech 3.0</i> mechanism; coarse mesh settings, HCNG 25	102
6.60	Zoom: pressure in cylinder 1; <i>SAGE: GRI Mech 3.0</i> mechanism; coarse mesh settings, HCNG 25	103
6.61	Heat release rate; <i>SAGE: GRI Mech 3.0</i> mechanism; coarse mesh settings, HCNG 25	103
6.62	Integrated heat release; <i>SAGE: GRI Mech 3.0</i> mechanism; coarse mesh settings, HCNG 25	104
6.63	Pressure in cylinder 1; <i>SAGE: GRI Mech 3.0</i> mechanism; coarse mesh settings, HCNG 25	105
6.64	Pressure in cylinder 1; <i>SAGE: USC mech II</i> ; coarse mesh settings, HCNG 25	106
6.65	Heat release rate; <i>SAGE: USC mech II</i> ; coarse mesh settings, HCNG 25	107
6.66	Integrated heat release; <i>SAGE: USC mech II</i> ; coarse mesh settings, HCNG 25	107
6.67	Pressure in cylinder 1; <i>SAGE: USC mech II</i> ; Monotone tolerance 0,025; coarse mesh settings, HCNG 25	108
6.68	Pressure in cylinder 1; <i>SAGE: USC mech II</i> ; Monotone tolerance comparison; coarse mesh settings, HCNG 25	109
6.69	Heat release rate; <i>SAGE: USC mech II</i> ; Monotone tolerance comparison; coarse mesh settings, HCNG 25	110
6.70	Integrated heat release; <i>SAGE: USC mech II</i> ; Monotone tolerance comparison; coarse mesh settings, HCNG 25	110
6.71	Pressure in cylinder 1; <i>SAGE: USC+USCD mechanisms merged</i> ; coarse mesh settings, HCNG 25	112
6.72	Pressure in cylinder 1; <i>SAGE</i> mechanisms comparison; coarse mesh settings, HCNG 25	113
6.73	Heat release rate; <i>SAGE</i> mechanisms comparison; coarse mesh settings, HCNG 25	113
6.74	Integrated heat release; <i>SAGE</i> mechanisms comparison; coarse mesh settings, HCNG 25	114

6.75	Pressure in cylinder 1; <i>SAGE: USC+USCD mechanisms merged</i> ; coarse mesh settings, HCNG 25	115
6.76	Zoom: Pressure in cylinder 1; <i>SAGE: USC+USCD mechanisms merged</i> ; coarse mesh settings, HCNG 25	116
6.77	Heat release rate; <i>SAGE: USC+USCD mechanisms merged</i> ; coarse mesh settings, HCNG 25	117
6.78	Integrated heat release; <i>SAGE: USC+USCD mechanisms merged</i> ; coarse mesh settings, HCNG 25	117
6.79	Pressure in cylinder 1; <i>SAGE: USC+USCD mechanisms merged</i> ; monotone tolerance comparison; coarse mesh settings, HCNG 25	118
6.80	Heat release rate; <i>SAGE: USC+USCD mechanisms merged</i> ; monotone tolerance comparison; coarse mesh settings, HCNG 25	119
6.81	Integrated heat release; <i>SAGE: USC+USCD mechanisms merged</i> ; monotone tolerance comparison; coarse mesh settings, HCNG 25	119
6.82	Pressure in cylinder 1; <i>SAGE: USC+USCD mechanisms merged</i> ; small crevice volume; coarse mesh settings, HCNG 25	121
6.83	Pressure in cylinder 1; <i>SAGE: USC+USCD mechanisms merged</i> ; coarse mesh settings, HCNG 25	122
6.84	Heat release rate; <i>SAGE: USC+USCD mechanisms merged</i> ; small crevice volume; coarse mesh settings, HCNG 25	123
6.85	Heat release rate; <i>SAGE: USC+USCD mechanisms merged</i> ; coarse mesh settings, HCNG 25	123
6.86	Integrated heat release; <i>SAGE: USC+USCD mechanisms merged</i> ; small crevice volume; coarse mesh settings, HCNG 25	124
6.87	Integrated heat release; <i>SAGE: USC+USCD mechanisms merged</i> ; coarse mesh settings, HCNG 25	124
6.88	Temperature comparison (a) 735 CAD ; (b) 750 CAD	126
6.89	CH ₄ mass fraction comparison at 780 CAD (a) HCNG 15 ; (b) HCNG 25	126
6.90	CH ₄ mass fraction comparison at 810 CAD (a) HCNG 15 ; (b) HCNG 25	127
6.91	CH ₄ mass fraction comparison at 850 CAD (a) HCNG 15 ; (b) HCNG 25	127
6.92	CH ₄ mass fraction in cylinder at 780 CAD (a) HCNG 15 ; (b) HCNG 25	128
6.93	CH ₄ mass fraction in cylinder at 810 CAD (a) HCNG 15 ; (b) HCNG 25	128
6.94	CH ₄ mass fraction in cylinder at 840 CAD (a) HCNG 15 ; (b) HCNG 25	129

List of Tables

1	Engine technical data	16
2	Fuel compositions	17
3	Where find the parameter in the TSMS file	24
4	Engine operating points considered	27
5	where to find the value for ICs and BCs	36
6	<i>Coarse mesh: Fixed embedding settings</i>	42
7	<i>Coarse mesh: AMR settings specifications</i>	43
8	Pollutant emissions results; <i>SAGE-GRI Mech 3.0</i> and experimental data; coarse mesh settings, HCNG 15	57
9	Pollutant emissions results; <i>SAGE-USC mech II</i> and experimental data; coarse mesh settings, HCNG 15	60
10	Pollutant emissions comparison: <i>USC mech II and USC+USCD mechanisms merged</i> ; coarse mesh settings, HCNG 15	65
11	Pollutant emissions results; <i>SAGE-USC+USCD merged</i> ; Schmidt Number = 0,765; coarse mesh settings, HCNG 15	68
12	Pollutant emissions results; <i>SAGE-USC+USCD merged</i> ; Schmidt Number = 0,75; coarse mesh settings, HCNG 15	71
13	Trapped mass comparison; <i>SAGE-USC+USCD merged</i> ; Schmidt Number sensitivity; coarse mesh settings, HCNG 15	72
14	Pollutant emissions results; <i>SAGE-USC+USCD merged</i> ; Schmidt Number sensitivity; coarse mesh settings, HCNG 15	74
15	Pollutant emissions results; Temperature of the wall = 397 K; <i>SAGE-USC+USCD merged</i> ; Schmidt Number = 0,75; coarse mesh settings, HCNG 15	78
16	Pollutant emissions results; Temperature of the wall = 377 K; <i>SAGE-USC+USCD merged</i> ; Schmidt Number = 0,75; coarse mesh settings, HCNG 15	80
17	Pollutant emissions results; <i>SAGE-USC+USCD merged</i> ; Temperature of the wall sensitivity; coarse mesh settings, HCNG 15	83
18	Pollutant emissions results; <i>SAGE-USC+USCD merged</i> ; LHV sensitivity; coarse mesh settings, HCNG 15	87
19	Pollutant emissions results; <i>SAGE-USC+USCD merged</i> ; LHV sensitivity; coarse mesh settings, HCNG 15	94
20	Pollutant emissions results; <i>Medium crevice volume</i> ; <i>SAGE-USC+USCD merged</i> ; Schmidt Number = 0,75; coarse mesh settings, HCNG 15	97
21	Pollutant emissions results; <i>Small crevice volume</i> ; <i>SAGE-USC+USCD merged</i> ; Schmidt Number = 0,75; coarse mesh settings, HCNG 15	99
22	Pollutant emissions results; Crevice volume sensitivity; <i>SAGE-USC+USCD merged</i> ; coarse mesh settings, HCNG 15	101
23	Pollutant emissions; <i>SAGE: GRI Mech 3.0</i> mechanism; coarse mesh settings, HCNG 25	104
24	Pollutant emissions results; Monotone tolerance comparison; <i>SAGE: USC mech II</i> ; coarse mesh settings, HCNG 25	111

25	Pollutant emissions results; Mechanisms comparison; coarse mesh settings, HCNG 25	114
26	Pollutant emissions; <i>SAGE: USC+USCD mechanisms merged</i> ; coarse mesh settings, HCNG 25	118
27	Results overview; <i>SAGE: USC+USCD mechanisms merged</i> ; monotone tolerance comparison; coarse mesh settings, HCNG 25	120
28	Results overview; <i>SAGE: USC+USCD mechanisms merged</i> ; effect of the crevices; coarse mesh settings, HCNG 25	125
29	Results overview	131

References

- [1] J. B. Heywood, “Internal combustion engine fundamentals,” 2018.
- [2] J. H. Ferziger and M. Peric, *Computational methods for fluid dynamics*. Springer Science & Business Media, 2012.
- [3] D. Anderson, J. C. Tannehill, and R. H. Pletcher, *Computational fluid mechanics and heat transfer*. CRC Press, 2016.
- [4] L. Testa, D. Misul, M. Baratta, and R. Rothbauer, “Combustion modelling of ng-engine using detailed chemistry in converge,” Ph.D. dissertation, Politecnico di Torino, 2018.
- [5] L. Ferretti, “Development and validation of ng-h2 engine numerical model embedding detailed chemistry in converge,” Ph.D. dissertation, Politecnico di Torino, 2018.
- [6] K. Richards, P. Senecal, and E. Pomraning, “Converge (version 2.3) manual,” *Convergent Science, Madison, WI*, 2017.
- [7] R. K. Mehra, H. Duan, R. Juknelevičius, F. Ma, and J. Li, “Progress in hydrogen enriched compressed natural gas (hcng) internal combustion engines—a comprehensive review,” *Renewable and Sustainable Energy Reviews*, vol. 80, pp. 1458–1498, 2017.
- [8] K. Kavathekar, S. Rairikar, and S. Thipse, “Development of a cng injection engine compliant to euro-iv norms and development strategy for hcng operation,” SAE Technical Paper, Tech. Rep., 2007.
- [9] J. Xu, X. Zhang, J. Liu, and L. Fan, “Experimental study of a single-cylinder engine fueled with natural gas–hydrogen mixtures,” *International journal of hydrogen energy*, vol. 35, no. 7, pp. 2909–2914, 2010.
- [10] K. Nanthagopal, R. Subbarao, T. Elango, P. Baskar, and K. Annamalai, “Hydrogen enriched compressed natural gas—a futuristic fuel for internal combustion engines.” *Thermal Science*, vol. 15, no. 4, 2011.
- [11] P. De Angelis, “Simulation of the ensemble and cycle-resolved combustion processes in a ng-h2 engine,” Ph.D. dissertation, Politecnico di Torino, 2017.
- [12] M. F. Brunt and A. L. Emtage, “Evaluation of burn rate routines and analysis errors,” Tech. Rep., 1997.
- [13] A. Siddique, S. A. Azeez, and R. Mohammed, “Simulation and cfd analysis of various combustion chamber geometry of a ci engine using cfx,” *Simulation*, vol. 5, no. 8, pp. 33–39, 2016.
- [14] S. R. Turns *et al.*, *An introduction to combustion*. McGraw-hill New York, 1996, vol. 499.